DESIGN AND DISPATCH OF CONCENTRATING SOLAR POWER TOWER SYSTEMS WITH UTILITY-SCALE PHOTOVOLTAICS

by

William T. Hamilton

A thesis submitted to the Faculty and the Board of Trustees of the Colorado School of Mines in partial fulfillment of the requirements for the degree of Doctor of Philosophy (Mechanical Engineering).

Golden, Colorado

Date _____

Signed: _____
William T. Hamilton

Signed: _____
Dr. Robert J. Braun
Thesis Advisor

Signed: _____
Dr. Alexandra M. Newman
Thesis Advisor

Golden, Colorado

Date _____

Signed: _____
Dr. John Berger
Professor and Head
Department of Mechanical Engineering

ABSTRACT

By utilizing inexpensive thermal energy storage, concentrating solar power (CSP) can provide dispatchable, stable, and renewable electricity generation; however, current system capital costs are uneconomical for widespread deployment. Conversely, the costs of photovoltaic (PV) systems have dropped significantly in the last decade, which has led to extensive market adoption. Coupling PV systems with batteries can mitigate much of their generation variability; however, the current battery costs are uneconomical to utilize as a grid-scale storage medium.

To compete in solar energy-dominated markets while taking advantage of the relative strengths of both technologies, CSP could dispatch electricity around PV generation, resulting a hybridization of the two technologies, referred to as a CSP-PV hybrid. Due to the limited availability of solar resource and storage capacity, CSP-PV hybrid system design and operational decisions are critical to overall economics. This dissertation presents a methodology for evaluating CSP-PV hybrid systems, which includes: (i) integrating CSP and PV simulation modules using a Python wrapper, (ii) expanding a profit-maximizing mixed-integer linear program that provides a dispatch strategy, (iii) implementing solution techniques to improve model tractability, (iv) modeling a molten salt-driven Rankine cycle to characterize off-design performance, and (v) utilizing derivative-free, or "black-box," algorithms to perform system-level design optimization.

For CSP-PV hybrid system dispatch at sub-hourly fidelity, we develop solution techniques to reduce solve times by as much as 93%. Additionally, we assess that CSP-PV hybrid systems can almost double capacity factors while improving various economic metrics by as much as 30%. Lastly, we determine that minimizing power purchase agreement price for CSP-PV hybrid design optimization results in systems with capacity factors less than 62%, but nonetheless with greater than 90% reliability.

TABLE OF CONTENTS

LIST OF FIGURES

LIST OF TABLES

LIST OF ABBREVIATIONS

Alternating Current . . . . . AC

California Independent System Operator . . . . . CAISO

Concentrating Solar Power . . . . . CSP

Department of Energy . . . . . DOE

Direct Current . . . . . DC

High Pressure Turbine . . . . . HPT

Intermediate Pressure Turbine . . . . . IPT

Low Pressure Turbine . . . . . HPT

Mean Squared Error . . . . . MSE

Mixed-Integer Linear Program . . . . . MILP

National Renewable Energy Laboratory . . . . . NREL

Pacific Gas and Electric . . . . . PG&E

Photovoltaic . . . . . PV

Power Purchase Agreement . . . . . PPA

Renewable Energy . . . . . RE

Spencer-Cotton-Cannon . . . . . SCC

System Advisor Model . . . . . SAM

Thermal Energy Storage . . . . . TES

Time-of-Delivery . . . . . ToD

ACKNOWLEDGMENTS

First and foremost, I would like to acknowledge my advisors, Professors Alexandra Newman and Rob Braun. Thank you for spending your time and effort on providing me an opportunity to achieve this degree and I hope to continue our professional relationship through the years to come. I would also like to thank my other committee members for their feedback and support: Prof. Greg Jackson, Prof. Jason Porter, Prof. Tulay Flamand, and Prof. Andres Guerra. In addition, I would like to give a special acknowledgment to Dr. Mike Wagner. You provided me insight and direction throughout my graduate career and for that, I thank you. I look forward to working with you and researchers at NREL to address the many questions left unanswered in this dissertation.

A majority of this dissertation work and my graduate school expenses were funded by the United States Department of Energy - Energy Efficiency and Renewable Energy under award numbers DE-EE00030338 and DE-EE00034245. Likewise, I am grateful for the Department of Mechanical Engineering for providing me with a funded position as a teaching assistant for my first semester. This opportunity enabled me interact with faculty, gain knowledge about research occurring within the department, and ultimately find a funded project that would support me through my graduate career.

I would like acknowledge my colleagues of the two research groups I was apart of during my time at Mines - Advanced Energy Systems Group and Operations Research with Engineering. Many of you have become my friends over last four and half years, which made graduate school that much more enjoyable. Bridging the gap between these two research groups allow me to cross-pollinate ideas and methods, which enabled better research (I believe) from each group. Specifically, I want to thank Dan Miller, David Curran, and Jamie Kee for giving me a reason to take a break and talk about anything other than research, but always ending the conversation with someone's latest research problem and brainstorming

potential solutions to address said problem. I would also like to thank Evan Reznicek for always challenging me with his questions, concerns, and ideas. From the operation research group, I want to thank the group as a whole for giving me many different perspectives during my graduate career. I wish all of you the best for your future endeavors.

I want to thank my family and friends for all the love they provided me over the years and their consistent questioning about when I will graduate. To my mother, whom I almost lost during my studies, you have supported my quest for knowledge since day one. To my father, you have taught me so much even though we have spent limited time together. To my grandfathers, while neither of you are engineers by trade, you two sparked my interest in building and repairing things at a early age and for that, I am grateful.

Finally and most importantly, I want to acknowledge my wife Molly Crouch for all of her unconditional love and support. You have taught me to enjoy the little things in life and to never take them for granted. Thank you for keeping life interesting and providing me an outlet from work. Without you, I would not be where I am today.

For my wife Molly,

I look forward to creating our future!

CHAPTER 1

INTRODUCTION

As the world's population grows, so does its demand for affordable, on-demand energy. Currently, a vast majority of the world's 168,519 TWh annual energy consumption, i.e., over 80% is supplied by fossil fuels [1]. Scientists agree that burning fossil fuels is producing greenhouse gases, e.g., carbon dioxide, at an alarming rate, causing climates to change around the world. The largest global greenhouse gas emissions sources include: (i) electricity and heat production at 25%, (ii) agriculture, forestry, and other land use at 24%, (iii) industry at 21%, and (iv) transportation at 14% [2]. With growing concerns about climate change, some countries are trying to reduce greenhouse gas emissions.

One of the main strategies of reducing emissions, and thereby the effects of climate change, is to decarbonize the electrical grid. This can be realized through three major technology pathways: (i) implementation of carbon capture and sequestration technologies on existing electricity generators, (ii) expansion of carbon-free resources (e.g., nuclear), and (iii) grid-integration of renewable energy (RE) resources, (e.g., wind, solar, hydro and geothermal). Each of these technology pathways has advantages and disadvantages. With the adoption of carbon capture and sequestration technologies, the electricity sector could continue to use fossil fuels without increasing emissions. However, current carbon capture technologies are expensive and reduce generator net efficiencies, which requires increasing the amount of fuel burned to produce a unit of electricity. On the other hand, fossil fuels are a finite resource, making carbon capture and sequestration unsustainable. Nuclear energy is a mature technology relative to the others; therefore, adoption could occur rapidly. Passive cooling nuclear reactors combined with thermal energy storage could be a promising path forward for the industry. However, due to some catastrophic events, there is a strong negative public opinion surrounding nuclear energy. In addition, disposal of nuclear waste has not been

sufficiently addressed. RE resources produce electricity without the use of fossil fuel, and their associated costs have significantly decreased in the last decade, leading to an increase in global adoption. However, RE sources possess technological and economical challenges.

At the time of writing, RE is anticipated to be the best option to sustainably decarbonize the electrical grid. Consequently, policy makers are implementing RE portfolio mandates and/or standards to reduce emissions and the effects of climate change [3]. State governments within the United States have legislated their own standards. For example, California plans to have 50% of its energy demands met using RE technologies by 2030 (Clean Energy and Pollution Reduction Act (SB350)). There is a large market-grown potential in the United States for RE solar systems depending on future costs [4]. However, as penetration of traditional variable generation sources, i.e., wind and photovoltaic solar, increases, so do challenges associated with grid stability and increased energy curtailment [5]. Electric, thermal, and chemical energy storage mitigate this instability, thereby potentially increasing RE share of the electricity market [6].

The following sections provide context for the dissertation. This includes an overview of RE technologies and the challenges of electrical grid integration, a description of the two distinct solar energy technologies, independently, and their hybridization.

1.1 Overview of Renewable Energy Technologies

Renewable energy technologies generate electricity from a sustainable resource without the production of greenhouse gases. Unfortunately, generation from RE resources are constrained by their availability in a particular geographic location, requiring a site-specific combination of RE technologies to meet demand. Each location requires a different combination of energy-generation technologies to meet electric demand reliably and cost-effectively. It has been estimated that solar technologies alone could power the worldwide energy demand, about 15-20 times over [7]. However, solar resource suffers from intermittence and diurnal cycles. Worldwide wind resource is estimated be able to power the world about 3-5 times over [7]. But, like solar, wind resource suffers from intermittence in generation.

Geothermal and hydro (hydroelectric, wave, and tidal combined) technologies yield a much smaller potential power resource compared to wind and solar. However, geothermal and hydro technologies are viable RE energy solutions for a subset of locations, but fall short of providing global energy demand.

Despite an abundance of solar and wind resources, how to capture, store, and dispatch them in an efficient, sustainable, and cost-effective manner remains a challenge. To capture solar energy, there are two distinct categories of technologies, photovoltaics (PV) and concentrating solar power (CSP). The following sections provide background on these two technologies and the hybridization of them.

1.2 Utility-Scale Photovoltaics

PV solar energy uses panels, called modules, comprised of an array of individual semiconducting solar cells that, when hit by a photon, generate a flow of electrons. The three main categories of solar cells are crystalline silicon, thin film, and multi-junction. Solar modules are connected in a variety of parallel and series configurations to meet voltage specifications of a power inverter, which transforms the direct current (DC), generated by the modules, to alternating current (AC) at the grid's regulated voltage and frequency. Modules can be mounted at a fixed orientation or can follow the relative movement of the sun using a single- or double-axis tracking system. PV systems can be coupled with electric energy storage, e.g., batteries, to provide some dispatchablity. However, battery technologies are still expensive and incapable of fully serving as a grid-scale storage method [8]. In addition, electric batteries suffer from capacity degradation caused by charge and discharge cycling. From a sustainability viewpoint, the industry has not addressed end-of-life recycling and/or disposal of grid-scale battery devices. The cost of PV systems has dropped significantly in the last decade and, as a result, deployment has rapidly accelerated. According to a recent National Renewable Energy Laboratory (NREL) report, 2017 utility-scale PV systems are already below the Department of Energy's 2020 SunShot target for levelized cost of energy ($0.06/kWh) [9]. Likewise, Basore and Cole argue that low-cost energy storage significantly

increases PV generation capacity [10].

1.3 CSP Tower Systems

CSP technologies capture solar thermal radiation by utilizing mirrors to concentrate the sun's energy onto a receiver. There are four major CSP technologies: parabolic trough, linear Fresnel, dish Stirling, and power tower. Each of these technologies has its relative benefits and drawbacks. Wagner et al. [11] provides an overview of CSP power tower technology advantages over those of other renewable and fossil alternatives. The power tower CSP configuration can achieve high concentration ratios (over a 1,000 suns) – as defined by collectors-to-surface area, and, correspondingly, high operating temperatures. Figure 1.1 depicts a CSP power tower system (also known as a "central receiver"), which uses a collector field of solar-tracking mirrors, called heliostats, to focus the sun's rays onto a receiver atop a tower. The receiver is a device that transfers heat from the incoming solar thermal energy to a flowing gas, liquid, or solid medium, depending on the application. Current utility-scale power tower systems use molten salt (60% $NaNO_3$ 40% KNO_3) to capture thermal energy within the receiver. At design conditions, molten salt enters and exits the receiver at 290℃ and 565℃, respectively. However, at the time of this writing, the Department of Energy (DOE) is interested in increasing the system's operating temperature to greater than 700℃ through three receiver pathways for future development: (i) air or supercritical CO_2 (gas), (ii) next-generation molten salts or sodium (liquid), and (iii) particles (solids) [12]. The CSP tower system consists of two well-insulated tanks used to store the salt at its high and low operating temperatures. With adequate tank design, molten salt can be held for extended periods of time, i.e., hours to days, with little to no heat dissipation. In the CSP power tower system, molten salt is considered as the heat transfer fluid and the thermal energy storage (TES) medium. With the use of TES, CSP tower plants decouple solar energy collection from electricity generation, allowing the technology to generate stable grid power through cloudy periods and throughout the night.

When the system operator wants to generate electrical power, high temperature molten salt is pumped from the storage tank to the steam generator, where the salt travels through a series of heat exchangers and the storage thermal energy is transferred to a working fluid of a thermodynamic heat engine. Current utility-scale systems generate electricity using a conventional steam Rankine cycle; however, the DOE suggests future CSP system may utilize a Supercritical CO_2 Brayton cycle, due to its high thermal-to-electric efficiency [12–14].

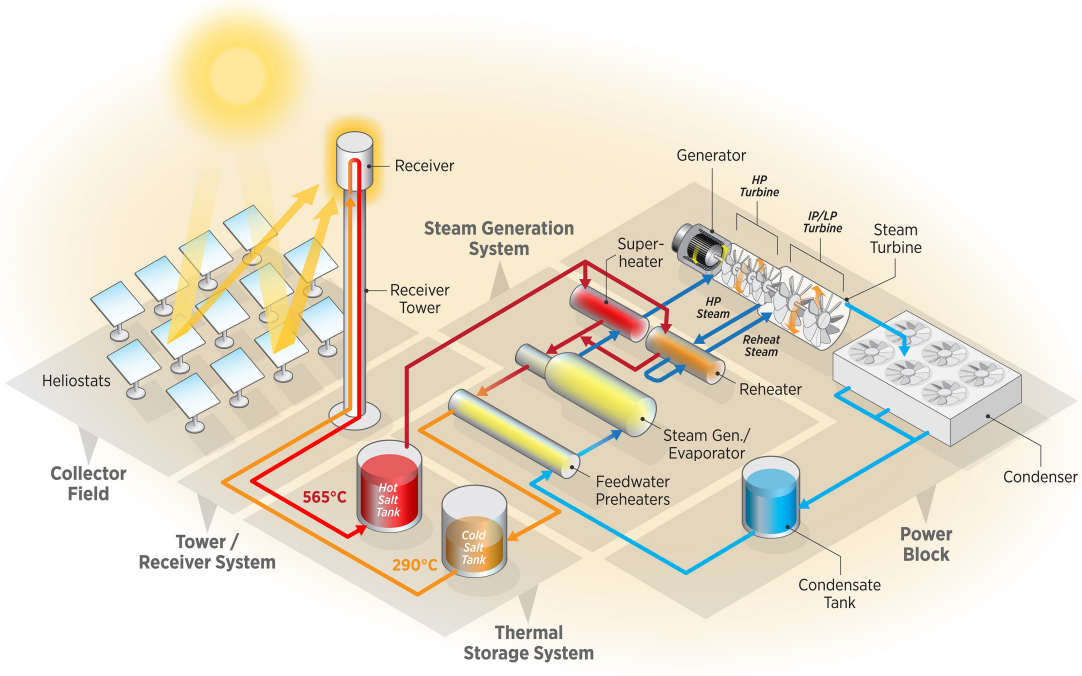

Figure 1.1: Molten salt power tower system configuration. The system consists of a heliostat field, molten salt receiver, direct TES system, steam generation system, Rankine power cycle, and heat rejection system (Graphic © NREL/Al Hicks).

1.4 CSP-PV Hybrid Systems

Hybridization of CSP with TES and PV with batteries reduces the cost of energy produced by the system while simultaneously providing reliable, dispatchable electricity. The proposed hybrid system exports low-cost PV generation during daytime hours while predominantly storing thermal energy collected by the CSP system. Stored energy can be dispatched for electricity generation at night or around disruptions in PV production, thereby achieving

a high capacity factor and a lower overall levelized cost of energy. CSP-TES-PV-battery hybrid systems, shown in Figure 1.2, are capable of replacing traditional fossil-fuel baseload generation and are therefore gaining popularity in international markets, e.g., Morocco [15] and Chile [16] at the time of this writing. However, the design, simulation, and optimization of CSP-TES-PV-battery hybrid systems presents significant challenges because the interaction of the sub-systems is not well understood.

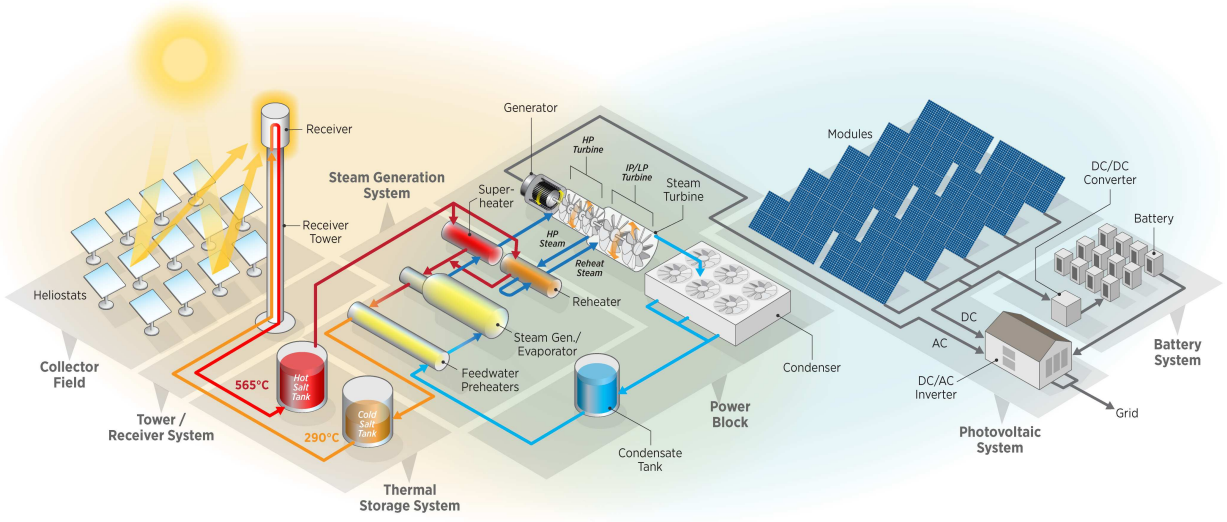

Figure 1.2: CSP-TES-PV-battery hybrid system configuration. The hybrid system consists of a molten salt power tower CSP plant (on the left) and a photovoltaic field with battery storage (on the right). The system depicted is not all-inclusive of components required for control or operation.

1.5 Grid Integration

The electricity grid balances generation (supply) and consumption (demand) exactly at any given point in time. Historically, this balance has been relatively easy to accomplish. A rise or fall in demand would cause grid operators to call upon generators to increase or decrease production, respectively. As penetration levels of intermittent RE (i.e., wind and solar) increase, balancing electricity supply and demand becomes increasingly challenging. To achieve high RE grid-penetration requires either: (i) over-generation and, consequently, curtailment, (ii) integration of highly flexible generators, ideally renewable, or (iii) adoption

of energy storage technologies [17]. The ability of a RE technology (e.g., CSP with TES) to be dispatched flexibly enables greater market potential than a highly variable generation source.

1.6 Research Questions

The current generation of commercial-scale CSP with TES systems were designed relatively simply, i.e., to operate under relaxed grid dispatch requirements. As these technologies mature, CSP systems will be expected to be increasingly flexible. Correspondingly, system designs will have to account for various market conditions. Designing CSP systems with and without neighboring PV generation requires accurate system modeling that can assess the design's performance and economics in a particular location and electricity market. The research questions to be answered in this dissertation are summarized as follows with brief discussion of the challenges:

Q.1 What are the benefits to solution accuracy (or quality) of CSP dispatch optimization when problem data fidelity is increased from hourly to 10-minute sub-hourly time periods? Furthermore, what solution techniques are required to maintain relatively fast solution times?

To move from hourly to sub-hourly time fidelity, the number of time periods in the problem horizon scales by a factor equal to the number of sub-hourly time periods in one hour. For example, the number time periods increases by a factor of six when increasing the fidelity from hourly to 10 minutes. Time-indexed variables and constraints (for all time periods) increase the problem size, resulting in intractability. Understanding the nature of the dispatch problem could allow for techniques to be applied that reduce the computational effort and corresponding solution times.

Q.2 Given a CSP-PV hybrid design, how should a CSP system operate when co-located with PV to maximize revenue, subject to grid constraints and/or utility contractual

agreements? Furthermore, if the PV system has battery storage, how do the three systems interact in an optimal economic dispatch scenario?

A CSP dispatch model that incorporates PV generation would provide insight on CSP-PV hybrid system operations, which may have to operate under utility-imposed transmission limits. The dispatch model could be expanded to include battery storage technologies, allowing for CSP with TES to interact with price-taker PV generation and battery storage. Historically, CSP-PV hybrid systems have been simulated as separate sub-systems and their corresponding generation profiles summed. However, this approach neglects the interaction effects between CSP and PV, which can result in less accurate predictions of their combined performances. Furthermore, CSP dispatching around PV generation requires the power cycle to operate under off-design conditions more frequently, which cannot be captured in the previous approaches.

Q.3 How does off-design Rankine cycle performance impact optimal operating strategies, annual simulation metrics, and system design decisions?

To analyze off-design Rankine cycle performance, steady-state component models with off-design relationships should be developed and integrated. Previous work has utilized this methodology to predict off-design Rankine cycle performance with varying inaccuracies. However, the implications of off-design Rankine cycle performance on optimal operating strategies has not be thoroughly explored and/or understood. Likewise, the cascading effect that off-design cycle performance has on system design decisions is a challenge that has not been addressed in literature.

Q.4 How do optimal design of CSP-PV hybrid systems change under various market scenarios?

By using dispatch optimization to determine system operational decisions, a design can be evaluated under different market scenarios. This process can be iterative using a derivative-free, or "black-box," optimization algorithm to change design variable values to improve an

objective. This analysis would provide insight on what markets are more favorable for CSP-only systems and when is it economically favorable to hybridize CSP and PV technologies. However, this approach can be computationally burdensome and has no guaranty of global optimality.

Answering the above questions provides insight into how CSP dispatchability with neighboring PV generation can influence a holistic system design (i.e., CSP-PV hybrids). The remainder of this dissertation has been divided into chapters to address the research questions stated above.

Chapter 2 addresses questions **Q.1** and **Q.2** by formulating a CSP-PV hybrid dispatch optimization model with battery storage at 10-minute intervals. Given a system design, the dispatch model maximizes profits by determining sub-system operations over the problem's time horizon. For annual production predictions, the dispatch optimization model is integrated with a higher fidelity simulation model, which utilizes a rolling time horizon that solves a dispatch problem every 24 hours with a 48-hour look-ahead policy. We conduct a case study using the electricity pricing profiles and solar resource data from locations in southern Nevada and northern Chile. Additionally, we apply solution techniques that improve tractability and reduce solve times. The contributions specific to this dissertation writer are: (i) formulating the CSP-PV hybrid dispatch optimization model, (ii) integrating the dispatch model with the system simulation software, and (iii) conducting and analyzing case study results and implications.

Chapter 3 addresses question **Q.3** by developing an off-design performance model of a molten salt-driven Rankine cycle. We validate our results using cycle performance data provided by an industry partner and against a model using similar methodology. We compare our resulting off-design performance to that of an industry-standard software tool and integrate our results into a simulation framework that is capable of modeling the whole CSP system with dispatch optimization developed in previous work [18]. We conduct a case study that demonstrates the impact of cycle off-design performance on optimal operating

decisions, for a stand-alone CSP system and a CSP-PV hybrid system. The contributions specific to this dissertation writer are: (i) developing the off-design performance model of a molten salt-driven Rankine cycle, (ii) integrating results from said model into CSP system simulation software, and (iii) investigating the impact of cycle off-design performance on system optimal dispatch, economics, and design decisions.

Chapter 4 addresses question **Q.4** by developing and implementing a methodology to optimize a CSP-PV system design utilizing derivative-free, or "black-box," optimization algorithms around previously developed simulation software. We employ an open-source library of algorithms called NLopt which enables us to address the system design problem with multiple algorithms using minimal development time. We conduct a case study that investigates the optimal CSP-PV hybrid system design configuration under four electricity market scenarios. The contributions specific to this dissertation writer are: (i) developing and implementing the design optimization methodology using derivative-free algorithms and (ii) analyzing case study results and there implications.

Finally, Chapter 5, summarizes our contributions and suggests ideas for future work.

CHAPTER 2

DISPATCH OPTIMIZATION OF CONCENTRATING SOLAR POWER WITH UTILITY-SCALE PHOTOVOLTAICS

This paper has been published in the journal *Optimization and Engineering*

William T. Hamilton[1,2], Mark A. Husted [1,3], Alexandra M. Newman[1,4,5], Robert J. Braun[1,5], and Michael J. Wagner[6]

2.1 Abstract

Concentrating solar power (CSP) tower technologies capture thermal radiation from the sun utilizing a field of solar-tracking heliostats. When paired with inexpensive thermal energy storage (TES), CSP technologies can dispatch electricity during peak-market-priced hours, day or night. The cost of utility-scale photovoltaic (PV) systems has dropped significantly in the last decade, resulting in inexpensive energy production during daylight hours. The hybridization of PV and CSP with TES systems has the potential to provide continuous and stable energy production at a lower cost than a PV or CSP system alone. Hybrid systems are gaining popularity in international markets as a means to increase renewable energy portfolios across the world. Historically, CSP-PV hybrid systems have been evaluated using either monthly averages of hourly PV production or scheduling algorithms that neglect the time-of-production value of electricity in the market.

To more accurately evaluate a CSP-PV-battery hybrid design, we develop a profit-maximizing mixed-integer linear program ($\mathcal{H}$) that determines a dispatch schedule for the

[1]Department of Mechanical Engineering, Colorado School of Mines, Golden, CO 80401
[2]Ph.D. Student
[3]Operations Research with Engineering Ph.D. Graduate
[4]Corresponding Author
[5]Professor of Mechanical Engineering
[6]Mechanical Engineer, Ph.D., National Renewable Energy Laboratory, Golden, CO 80401

individual sub-systems with a sub-hourly time fidelity. We present the mathematical formulation of such a model and show that the original formulation is intractable and computationally expensive to solve. To improve model tractability and reduce solution times, we offer techniques that: (i) reduce the problem size, (ii) tighten the linear programming relaxation of ($\mathcal{H}$) via reformulation and the introduction of cuts, and (iii) implement an optimization-based heuristic (that can yield initial feasible solutions for ($\mathcal{H}$) and, at any rate, yields near-optimal solutions). Applying these solution techniques results in 79% improvement in solve time, on average, for the 48-hour instances of ($\mathcal{H}$) we solve; corresponding solution times for an annual model run decrease by as much as 93%, where such a run consists of solving 365 instances of ($\mathcal{H}$), retaining only the first 24 hours' worth of the solution, and sliding the time window forward 24 hours. We present annual system metrics for two locations and two markets that inform design practices for hybrid systems and lay the groundwork for a more exhaustive policy analysis. A comparison of alternative hybrid systems to the CSP-only system demonstrates that hybrid models can almost double capacity factors while resulting in a 30% improvement related to various economic metrics.

2.2 Introduction

Renewable energy portfolio mandates and/or standards reduce emissions and the effects of climate change [3]. Governments within the United States have legislated their own standards, e.g., California plans to have 50% of its energy demands met using renewable energy technologies by 2030 (Clean Energy and Pollution Reduction Act (SB350)). However, as penetration of traditional variable generation sources, i.e., wind and photovoltaic solar, increases, so do challenges associated with grid stability and increased energy curtailment [5]. Electric, thermal, and chemical energy storage mitigate this instability, thereby potentially increasing renewable energy share of the electricity market [6].

Concentrating solar power (CSP) is a renewable energy technology that uses relatively inexpensive media such as high-temperature salt to store thermal energy for later use in power generation. CSP technologies capture solar thermal radiation by utilizing mirrors

to concentrate the sun's energy onto a receiver. There are four major CSP technologies: parabolic trough, linear Fresnel, dish Stirling, and power tower. Each of these technologies has its relative benefits and drawbacks. CSP power tower (also known as a "central receiver") uses a field of thousands of mirrors, called heliostats, to focus the sun's rays onto a receiver atop a tower. This CSP configuration can achieve high concentration ratios as defined by collectors-to-surface area, and, correspondingly, high operating temperatures, without the high cost, compared to those of any other CSP technology, thereby allowing the solar heat collection system to be paired with higher efficiency power cycles. CSP power tower technology presents a promising path forward for utility-scale energy production with the greatest potential for cost reduction and efficiency improvement [19].

Wagner et al. [20] provide an overview of CSP power tower technology advantages over those of other renewable and fossil alternatives. With the use of TES, CSP power tower plants decouple solar energy collection from electricity generation, allowing the technology to generate stable grid power through cloudy periods and throughout the night, shown in the case study of Rice, California. This decoupling of collection and generation also permits the power tower technology to be paired with any conventional thermodynamic conversion power cycles, e.g, a steam Rankine cycle. However, Turchi et al. [13] and Dunham and Iverson [14] present supercritical carbon dioxide power cycles as the most promising. The methodology presented in this paper can be adapted to supercritical carbon dioxide power cycles as the technology matures.

Photovoltaic (PV) solar energy uses panels comprised of an array of individual solar cells made of semi-conducting material that, when hit by a photon, generates a flow of electrons. Modules are connected in a variety of parallel and series configurations to provide voltage to a power inverter that transforms the direct current (DC) to alternating current (AC) at the grid's regulated voltage and frequency. Photovoltaic panels can be mounted at a fixed orientation or can track the sun using a single- or double-axis system. PV can be coupled with electric energy storage, e.g., batteries, to provide some dispatchablity. However, battery

technologies are still expensive and incapable of fully serving as a grid-scale storage method [8]. The cost of PV systems has dropped significantly in the last decade and, as a result, deployment has rapidly accelerated. Fu et al. [9] reports that 2017 utility-scale PV systems are already below the Department of Energy's 2020 SunShot target for levelized cost of energy. Basore and Cole [10] argue that low-cost energy storage significantly increases PV generation capacity.

This paper demonstrates that hybridization of PV and batteries with CSP with TES reduces the cost of energy produced by the system while simultaneously providing reliable, dispatchable electricity. The proposed hybrid system exports low-cost PV generation during daytime hours while predominantly storing thermal energy collected by the CSP system. Stored energy can be dispatched for electricity generation at night or around disruptions in PV production, thereby achieving a high capacity factor and lower overall levelized energy cost. CSP-TES-PV-battery hybrid systems, shown in Figure 2.1, are capable of replacing traditional fossil fuel baseload generation and are therefore gaining popularity in international markets, e.g., Morocco [15] and Chile [16] at the time of this writing. However, the design and simulation of CSP-TES-PV-battery hybrid systems presents significant challenges because the interaction of the two systems is not well understood.

To analyze a CSP-TES-PV-battery hybrid design, we develop a mixed-integer linear programming (MILP) model that prescribes a dispatch strategy at a ten-minute time fidelity. The strategy is implemented within an engineering simulation framework on a rolling time horizon basis to determine the performance of the system over a longer horizon – typically, one year. This approach makes use of existing methods and software tools both for the MILP characterizing CSP and for the engineering simulation of plant performance. The dispatch model determines an operating schedule that maximizes profits over the prescribed time horizon while accounting for solar resource and electricity price forecasts, sub-system sizing, operational limits, and performance characteristics.

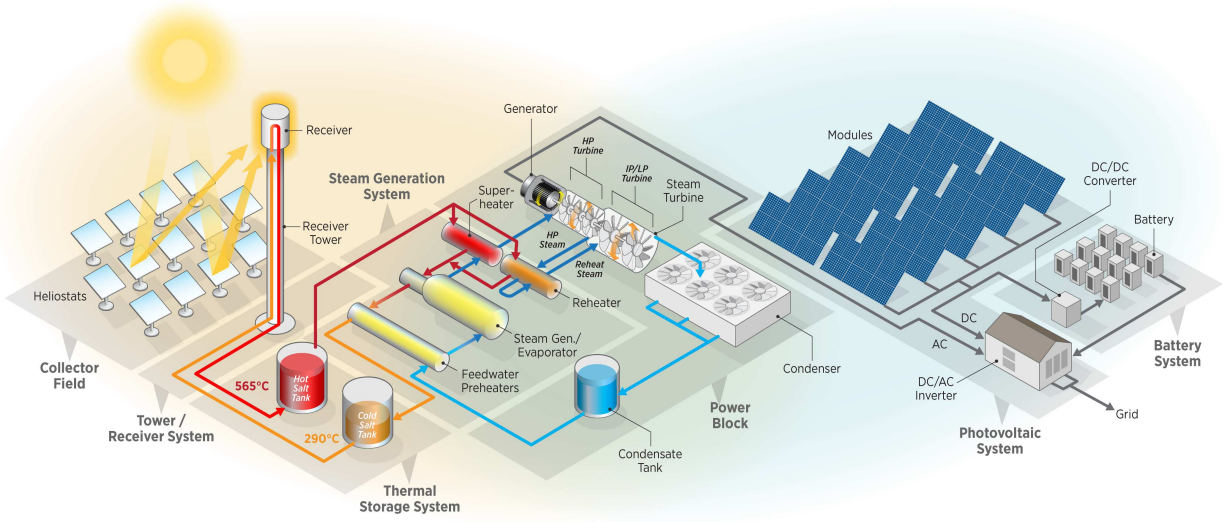

Figure 2.1: CSP-TES-PV-battery hybrid system configuration (Graphic © NREL/Al Hicks). On the left, the system consists of a molten salt power tower CSP plant, which consists of a heliostat field, molten salt receiver, thermal energy storage, and a Rankine power cycle. On the right, the system consist of a photovoltaic system with battery storage. The system depicted is not all-inclusive of components required for control or operation.

The remainder of the paper is organized as follows: Section 2.3 provides a literature review of dispatch methodologies used for stand-alone CSP with TES, stand-alone PV with battery, and combined CSP-PV hybrids. Section 2.4 presents and discusses a mathematical formulation of the hybrid system dispatch optimization model. Section 2.5 describes the challenges of model complexity and corresponding solution techniques implemented to improve tractability and reduce solution time. Section 2.6 presents a case study that exercises the model with the CSP-TES-PV-battery hybrid system design evaluated for two locations and two corresponding markets. We present results regarding annual plant performance and solution time improvements, and contrast hybrid and stand-alone system performance. Section 2.7 concludes with a summary and extensions of our work.

2.3 Literature Review

A system that combines PV with batteries is more commonly used in smaller residential markets, while CSP with TES is used only for larger commercial generation. However, with greater penetration of renewable energy sources in the electricity market, utility-scale battery

storage is being considered to increase grid stability by providing ancillary services, shaving peak-load, and integrating renewables [21, 22]. The combination of PV and CSP has only in recent years gained traction. We review (i) PV with battery storage, and (ii) CSP with TES separately and then (iii) examine cases that combine some subset of (i) and (ii).

2.3.1 Photovoltaics with Battery Storage

In general, literature pertaining to PV-battery systems suggests that batteries should either "peak-shift" demand, store energy from lower-demand parts of the day for use during high demand, or smooth power output during variations in solar resource, e.g., Heymans et al. [23]. Utility companies provide price incentives to induce this behavior.

Combining PV and lithium-ion batteries can reduce residential electricity use on the grid. Tervo et al. [24] demonstrate the cost effectiveness of these systems using bi-directional metering to sell energy back to the utility in each state in the United States of America. PV-plus-battery system sizing can be done at the residential scale for a single household [25], or for a university campus [26], and can include hybrid options such as wind or fuel cells, but does not employ mixed integer linear programs (MILPs) to determine the operations of the hybrid's sub-systems such as we do. Gitizadeh and Fakharzadegan [27] use a MILP to optimize the capacity of a battery for a grid-connected PV system and find that the resulting battery size is sensitive to the pricing structure.

Weather transients such as passing clouds significantly affect the performance of PV-plus-battery systems, though performance can be described using simplified models [28]; the authors compare results from an artificial neural network simulation model against experimental results during cloudy days. Shi et al. [29] forecast PV based on simplified categorized weather conditions for the following day with a view towards maximizing energy output and profit. These models differ from ours because we use the System Advisor Model (SAM) to estimate the performance of renewable equipment [30].

Various researchers propose linear programs to determine a dispatch, rather than a design, strategy for a PV-plus-battery system in day-ahead and real-time markets [31, 32],

respectively; however, there is no consideration of the battery charge and discharge currents. Hassan et al. [33] study a PV-plus-battery storage system with a feed-in-tariff incentive. Riffonneau et al. [34] compare optimizing a PV-plus-battery grid-connected system using dynamic programming with a rule-based heuristic. Lu and Shahidehpour [35] analyze the impact of scheduling short-term battery usage at hourly time fidelity on utility operations using a Lagrangian relaxation-based optimization algorithm. While these models use optimization, they do not simultaneously capture design and dispatch decisions, and, if a heuristic is used, optimality of the corresponding dispatch solutions cannot be guaranteed.

2.3.2 Concentrated Solar Power with Thermal Energy Storage

CSP systems use heliostats to focus sunlight onto a central receiver located on top of a tower to heat molten salt. By using TES to store the heat of the molten salt for use in power production at a later time, a CSP system can participate more reliably in day-ahead markets. Vasallo and Bravo [36] propose two models to optimize dispatch scheduling and apply the approach to a 50 MW CSP plant with TES to maximize profits in a day-ahead market. Algorithms exist to optimize the CSP plant's market participation with scheduling and control decisions [37]; the authors show that incorporating detailed dynamics into multi-scale electricity markets can increase revenues by up to 50% for certain capacities of thermal energy storage. Optimally sizing CSP-TES systems is done with the System Advisor Model using a short-term control strategy or with a model developed by Casella et al. [38]. Usaola [39] create a dispatch strategy based on day-ahead electricity market prices and examine the effects that incentives offer. Petrollese et al. [40] examine ways to handle weather uncertainty to mitigate its impact on revenue.

2.3.3 Hybrid Systems

For the purposes of this analysis, a *hybrid power generation system* is one in which two or more technologies that are capable of independently producing and/or storing energy are deployed in a coordinated – and often co-located – design. As such, many hybrid concepts are

possible and do not necessarily include CSP. For example, PV-battery systems might be used to support electrical generation for peak-load shaving and prevent peaking generators from turning on. Ashari and Nayar [41] illustrate the use of a PV, battery, and diesel generator hybrid system to develop policies or dispatch rules to more efficiently meet load.

Previous work on migrogrids with generators demonstrates that hybrid systems can effectively support electrical demand. Scioletti et al. [42] compare how integration of solar power and batteries into a diesel-powered microgrid reduces fuel consumption relative to a microgrid possessing only diesel generators, while Goodall et al. [43] extend the work to capture fade and temperature effects of the batteries. Muselli et al. [44] optimize equipment size in a microgrid consisting of PV, a battery, and gasoline or diesel generators, and show economic benefits over a PV stand-alone system. Marwali et al. [45] optimize thermal unit commitment at hourly time fidelity for a day-long time horizon to demonstrate the benefits of the PV-battery system.

In the last half decade, the solar industry has shown increasing interest in the design and deployment of CSP-PV hybrid systems. Preliminary analysis suggests that the inclusion of photovoltaics can increase the capacity factor of a baseload CSP plant from 80% to roughly 90% in a cost-effective manner [46]. Determining optimal equipment sizes in the hybrid system is important for lowering the power purchase agreement price, which can be different between areas of variable and constant hourly demand [47]. Denholm et al. [4] explore the economic opportunities of solar energy systems for the United States grid. The optimal solar energy system design with storage for constant power output has a different CSP-to-PV size ratio in areas where there are significant changes in the length of day throughout the year [48].

Concentrating solar power systems with TES are dispatchable, increasing overall grid flexibility and allowing for greater penetration of other non-dispatchable renewable resources such as PV and wind [17]. Similarly, Cocco et al. [49] improve power dispatchability, but instead use concentrated photovoltaics. Solar hybrids can generate *baseload* power at a lower

levelized cost of electricity than CSP or PV systems could alone [50]. An evaluation of a 50MW power plant for a mining operation in Chile shows how well a PV, a CSP, and a hybrid PV-CSP system effectively meet the mine's electricity demand [51]; however, the study does not include a battery system. A similar analysis is performed on a desalination plant in northern Chile [52], also without batteries.

2.3.4 Contribution

This paper presents a new hybrid system dispatch model that builds on existing work for optimizing dispatch for CSP [11] and for PV with batteries [53]. The results indicate that CSP with TES supplements the diurnal and variable PV generation profiles while the batteries provide rapid response to sudden changes in PV production or demand conditions. Furthermore, the model generates dispatch profiles at 10-minute intervals for an annual time horizon determined in 48-hour increments with a 24-hour look-ahead policy, improving upon previous models with lower temporal fidelity. The approach both adapts existing and develops new techniques for this application; specifically: it (i) modifies a fix-and-relax heuristic in two ways (both with respect to system components and with respect to time); (ii) linearizes nonlinear terms; and (iii) develops valid inequalities to improve proof of optimality.

2.4 Dispatch Optimization Model

Designing CSP-PV hybrid systems possesses its own unique challenges, requiring simulation to couple both subsystems, which has historically been done using monthly average hourly PV production [46]. By taking an average of the monthly PV production, the variability of PV resource is not captured, thereby over-predicting the production of the CSP-PV hybrid system. We propose to replace a heuristic, which had been used for dispatch solely of a CSP system, with a detailed optimization model that contains PV and a battery and that determines decisions at a 10-minute time fidelity, to determine an optimal schedule over a year-long time horizon.

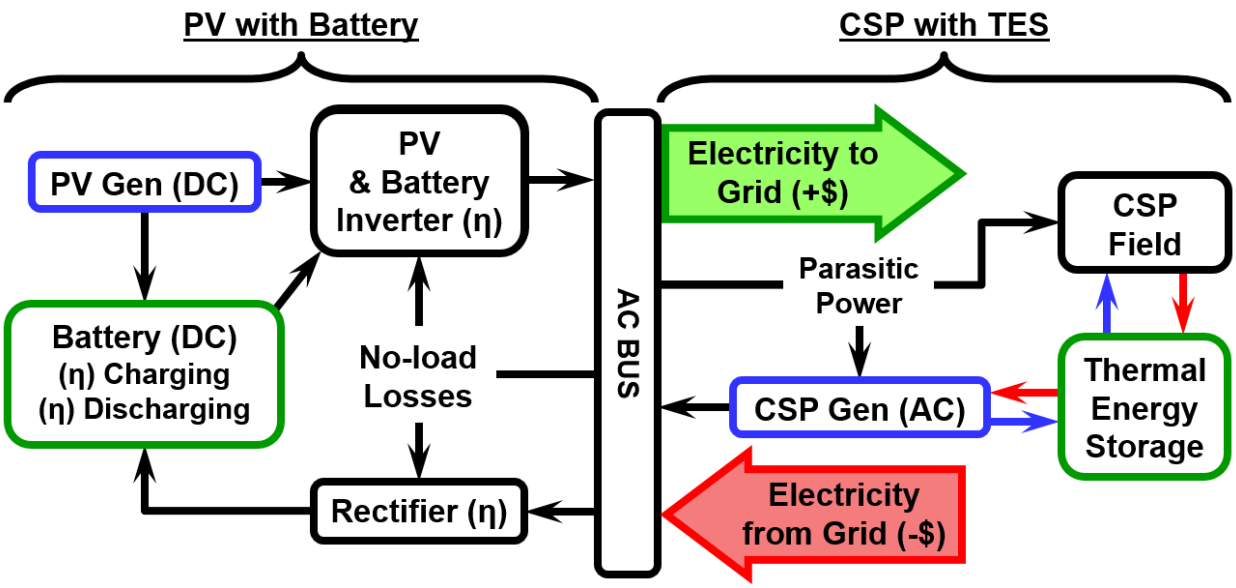

Figure 2.2: System layout consisting of CSP system (with TES), PV solar field generation, and battery storage.

Figure 2.2 presents a block diagram of a solar hybrid system. On the left of the alternating current (AC) bus, there is the PV array with battery storage. To the right of the AC bus is a CSP field, a power cycle (for CSP generation), TES coupled to both of these, and a connection to and from the grid. The black arrows represent electricity flow while the red and blue arrows represent "hot" and "cold" TES molten salt flows, respectively. The hybrid system produces electricity that can be sold to the grid, and can also purchase electricity from the grid in the analyzed configuration. This configuration is one of several possible, and various constraints related to grid connection, intra-system connections, and design considerations may alter the system topology in practice.

This section describes the sets, parameters, variables, objective function, and constraining relationships comprising the optimization model. Parameters and variables that contain the subscript of time t indicate their time-varying nature. In general, upper-case letters denote parameters while lower-case letters are reserved for variables. We also use lower-case letters for indices and upper-case script letters for sets.

2.4.1 Notation

The following MILP, ($\mathcal{H}$), requires the initial operational state of the system, the PV field and receiver energy generation forecasts, the expected cycle conversion efficiency profile as a function of ambient temperature and thermal input, and the energy price or tariff profile (Table 2.1).

Table 2.1: Hybrid dispatch model, ($\mathcal{H}$), set and parameters.

Set	
$\mathcal{T}$	Set of all time steps in the time horizon
Time-indexed Parameters	
Δ_t^{rs}	Estimated fraction of time step t required for receiver start-up [-]
η_t^{amb}	Cycle efficiency ambient temperature adjustment factor in time t [-]
η_t^{c}	Normalized condenser parasitic loss in time t [-]
P_t	Electricity sales price in time t [\$/kWh$_\mathsf{e}$]
Q_t^{in}	Available thermal power generated by the CSP heliostat field in time t [kW$_\mathsf{t}$]
W_t^{DC}	Available DC power generated by the PV field in time t [kW$_\mathsf{e}$]
W_t^{net}	Net grid transmission upper limit in time t [kW$_\mathsf{e}$]
Battery Parameters	
A^V	Battery linear voltage model slope coefficient [V]
α^+, α^-	Bi-directional slope-intercept for charge and discharge [kW$_\mathsf{e}$]
B^V	Battery linear voltage model intercept coefficient [V]
β^+, β^-	Bi-directional slope for charge and discharge [-]
C^B	Battery manufacturer-specified capacity [kAh]
I^{avg}	Typical current expected from the battery for both charge and discharge activities [A]
I^{L+}, I^{U+}	Battery charge current lower and upper bounds [kA]
I^{L-}, I^{U-}	Battery discharge current lower and upper bounds [kA]
$\underline{P}^B, \bar{P}^B$	Battery minimum and maximum power ratings [kW$_\mathsf{e}$]
R^{int}	Battery internal resistance [Ω]
$\underline{S}^B, \bar{S}^B$	Battery state of charge minimum and maximum operational bounds [-]
Cost Parameters	
C^{rec}	Operating cost of heliostat field and receiver [\$/kWh$_\mathsf{t}$]
C^{rsu}	Penalty for receiver cold start-up [\$/start]
C^{rhsp}	Penalty for receiver hot start-up [\$/start]
C^{pc}	Operating cost of power cycle [\$/kWh$_\mathsf{e}$]
C^{csu}	Penalty for power cycle cold start-up [\$/start]

Table 2.1: Continued

C^{chsp}	Penalty for power cycle hot start-up [$/start]
$C^{\delta W}$	Penalty for change in power cycle production [$/$\Delta$kW$_e$]
C^{csb}	Operating cost of power cycle standby operation [$/kWh$_t$]
C^{pv}	Operating cost of photovoltaic field [$/kWh$_e$]
C^{bc}	Operating cost of charging battery [$/kWh$_e$]
C^{bd}	Operating cost of discharging battery [$/kWh$_e$]
C^{bl}	Lifecycle cost for battery [$/lifecycle]

CSP Field and Receiver Parameters

Δ^l	Minimum time to start the receiver [hr]
E^{hs}	Heliostat field startup or shut down parasitic loss [kWh$_e$]
E^r	Required energy expended to start receiver [kWh$_t$]
E^u	Thermal energy storage capacity [kWh$_t$]
L^r	Receiver pumping power per unit power produced [kW$_e$/kW$_t$]
Q^{rl}	Minimum operational thermal power delivered by receiver [kWh$_t$]
Q^{rsb}	Required thermal power for receiver standby [kWh$_t$]
Q^{rsd}	Required thermal power for receiver shut down [kWh$_t$]
Q^{ru}	Allowable power per period for receiver start-up [kWh$_t$]
W^h	Heliostat field tracking parasitic loss [kW$_e$]
W^{ht}	Tower piping heat trace parasitic loss [kW$_e$]

Power Cycle Parameters

δW^{lim}	Power cycle ramp limit per time step [kW$_e$]
E^c	Required energy expended to start cycle [kWh$_t$]
η^{des}	Cycle nominal efficiency [-]
η^p	Slope of linear approximation of power cycle performance curve [kW$_e$/kW$_t$]
L^c	Cycle heat transfer fluid pumping power per unit energy expended [kW$_e$/kW$_t$]
Q^b	Cycle standby thermal power consumption per period [kW$_t$]
Q^c	Allowable power per period for cycle start-up [kW$_t$]
Q^l	Minimum operational thermal power input to cycle [kW$_t$]
Q^u	Cycle thermal power capacity [kW$_t$]
W^b	Power cycle standby operation parasitic load [kW$_e$]
W^u	Cycle electric power rated capacity [kW$_e$]

PV Parameters

α^{pv}, β^{pv}	Inverter slope-intercept linear approximation of DC-to-AC efficiency [kW$_e$, -]
W^I	Inverter DC power limit [kW$_e$]

Table 2.1: Continued

Miscellaneous Parameters	
α	Conversion factor between unitless and monetary values [$]
Δ	Time step duration [hr]
γ	Exponential time weighting factor [-]
$\mathbb{M}$	Sufficiently large number [-]
ϵ	Sufficiently small number [-]

The variables (see Table 2.2) describe energy (thermal kWh_t or electric kWh_e) states and power flows (thermal kW_t or electric kW_e) in the system. Continuous variables "x," "$\dot{w}$," "u," and "s" representing power and energy relate to the receiver, power cycle, PV field, battery, and TES. Binary variables "y" enforce operational modes and sequencing such that start-up must occur before normal operation, for example.

Table 2.2: Variables used in ($\mathcal{H}$).

Continuous	
b^c	Battery cycle count [-]
b_t^{soc}	State of charge of battery in time period t [-]
i_t^+, i_t^-	Battery current for charge and discharge in time period t [kA]
s_t	TES reserve quantity at time t [kWh_t]
u_t^{csu}	Cycle start-up energy inventory at time t [kWh_t]
u_t^{rsu}	Receiver start-up energy inventory at time t [kWh_t]
v_t^{soc}	Battery voltage in time period t [V]
$\dot{w}_t$	Power cycle electricity generation at time t [kW_e]
$\dot{w}_t^+, \dot{w}_t^-$	Power into and out of the battery at time t [kW_e]
$\dot{w}_t^\delta$	Power cycle change in electricity production at time t [kW_e]
$\dot{w}_t^{pv}$	Power from the photovoltaic field at time t [kW_e]
$\dot{w}_t^{pv+}$	Power from PV directly charging the battery at time t [kW_e]
$\dot{w}_t^s$	Electrical power sold to the grid at time t [kW_e]
$\dot{w}_t^p$	Electrical power purchased from the grid at time t [kW_e]
x_t	Cycle thermal power utilization at time t [kW_t]
x_t^r	Thermal power delivered by the receiver at time t [kW_t]
x_t^{rsu}	Receiver start-up power consumption at time t [kW_t]

Binary	
y_t^r	1 if receiver is generating "usable" thermal power at time t; 0 otherwise
y_t^{rhsp}	1 if receiver hot start-up penalty is incurred at time t (from standby); 0 otherwise
y_t^{rsb}	1 if receiver is in standby mode at time t; 0 otherwise

Table 2.2: Continued

y_t^{rsd}	1 if receiver is shut down at time t; 0 otherwise
y_t^{rsu}	1 if receiver is starting up at time t; 0 otherwise
y_t^{rsup}	1 if receiver cold start-up penalty is incurred at time t (from off); 0 otherwise
y_t	1 if cycle is generating electric power at time t; 0 otherwise
y_t^{chsp}	1 if cycle hot start-up penalty is incurred at time t (from standby); 0 otherwise
y_t^{csb}	1 if cycle is in standby mode at time t; 0 otherwise
y_t^{csd}	1 if cycle is shutting down at time t; 0 otherwise
y_t^{csu}	1 if cycle is starting up at time t; 0 otherwise
y_t^{csup}	1 if cycle cold start-up penalty is incurred at time t (from off); 0 otherwise
y_t^+, y_t^-	1 if battery is charging or discharging in time period t; 0 otherwise
y_t^{pv}	1 if the PV field is generating power at time t; 0 otherwise

2.4.2 Objective Function and Constraints

We maximize the sale of electricity given as the revenue based on sales minus the cost of grid purchase throughout the time horizon in question. We decrement the revenue by penalties incurred for start-ups and shut-downs, changes in production between successive time periods, and operating costs related to the power cycle, the PV field, the receiver and the battery. Lesser penalties are introduced to enforce the logic associated with the receiver and power cycle shut down, and we also charge for battery lifecycles consumed during the time horizon.

$$
\begin{aligned}
(\mathcal{H})\ \text{maximize}\quad & \sum_{t\in\mathcal{T}} \Big[\Delta \cdot P_t(\dot{w}_t^s - \dot{w}_t^p) \\
& - \Big(\frac{1}{\gamma}\Big)^t (C^{csu} y_t^{csup} + C^{chsp} y_t^{chsp} + \alpha y_t^{csd} + C^{\delta W} \dot{w}_t^{\delta}) \\
& - \Big(\frac{1}{\gamma}\Big)^t \big(C^{rsu} y_t^{rsup} + C^{rhsp} y_t^{rhsp} + \alpha y_t^{rsd}\big) \\
& - \Big(\frac{1}{\gamma}\Big)^t \Delta\big(C^{pc}\dot{w}_t + C^{csb} Q^b y_t^{csb} + C^{pv}\dot{w}_t^{pv} + C^{bd}\dot{w}_t^- \\
& + C^{bc}\dot{w}_t^+ + C^{rec} x_t^r\big)\Big] - C^{bl} b^c
\end{aligned}
\tag{2.1}
$$

2.4.2.1 Receiver Operations

We include the following constraints that govern receiver operations:

Receiver Start-up

$$u_t^{rsu} \leq u_{t-1}^{rsu} + \Delta x_t^{rsu} \qquad \forall\, t \in \mathcal{T} : t \geq 2 \tag{2.2a}$$
$$u_t^{rsu} \leq E^r y_t^{rsu} \qquad \forall\, t \in \mathcal{T} \tag{2.2b}$$
$$y_t^r \leq \frac{u_t^{rsu}}{E^r} + y_{t-1}^r + y_{t-1}^{rsb} \qquad \forall\, t \in \mathcal{T} : t \geq 2 \tag{2.2c}$$
$$y_t^{rsu} + y_{t-1}^r \leq 1 \qquad \forall\, t \in \mathcal{T} : t \geq 2 \tag{2.2d}$$
$$x_t^{rsu} \leq Q^{ru} y_t^{rsu} \qquad \forall\, t \in \mathcal{T} \tag{2.2e}$$
$$y_t^{rsu} \leq \frac{Q_t^{in}}{Q^{rl}} \qquad \forall\, t \in \mathcal{T} \tag{2.2f}$$

Receiver Supply and Demand

$$x_t^r + x_t^{rsu} + Q^{rsd} y_t^{rsd} \leq Q_t^{in} \qquad \forall\, t \in \mathcal{T} \tag{2.3a}$$
$$x_t^r \leq Q_t^{in} y_t^r \qquad \forall\, t \in \mathcal{T} \tag{2.3b}$$
$$x_t^r \geq Q^{rl} y_t^r \qquad \forall\, t \in \mathcal{T} \tag{2.3c}$$
$$y_t^r \leq \frac{Q_t^{in}}{Q^{rl}} \qquad \forall\, t \in \mathcal{T} \tag{2.3d}$$

Logic Associated with Receiver Modes

$$y_t^{rsu} + y_t^{rsb} \leq 1 \qquad \forall\, t \in \mathcal{T} \tag{2.4a}$$
$$y_t^r + y_t^{rsb} \leq 1 \qquad \forall\, t \in \mathcal{T} \tag{2.4b}$$
$$y_t^{rsb} \leq y_{t-1}^r + y_{t-1}^{rsb} \qquad \forall\, t \in \mathcal{T} : t \geq 2 \tag{2.4c}$$
$$y_t^{rsup} \geq y_t^{rsu} - y_{t-1}^{rsu} \qquad \forall\, t \in \mathcal{T} : t \geq 2 \tag{2.4d}$$
$$y_t^{rhsp} \geq y_t^r - (1 - y_{t-1}^{rsb}) \qquad \forall\, t \in \mathcal{T} : t \geq 2 \tag{2.4e}$$
$$y_t^{rsd} \geq (y_{t-1}^r - y_t^r) + (y_{t-1}^{rsb} - y_t^{rsb}) \qquad \forall\, t \in \mathcal{T} : t \geq 2 \tag{2.4f}$$

In order for the system to generate power, we impose Constraint (2.2a) which accounts for receiver start-up energy "inventory"; we employ an inequality such that inventory can revert to a level of zero in time periods after which start-up has completed. Inventory is allowed to assume a positive value during time periods of receiver start-up (Constraint (2.2b)). Power

production is positive only upon completion of a start-up or if the receiver also operates in the time period prior (Constraint (2.2c)). If the receiver is producing thermal power in time $t-1$, it cannot be starting up in the following time period t (Constraint (2.2d)). Ramp-rate limits must be honored during the start-up procedure (Constraint (2.2e)). Trivial solar resource prevents receiver start-up (Constraint (2.2f)).

The parameter Q_t^{in} provides an upper bound on the thermal power produced by the receiver, from which any energy used for start-up or shutdown detracts (Constraint (2.3a)). Constraint (2.3b) permits the receiver to generate thermal power only while in power-producing mode. Receiver thermal power generation is subject to a lower bound by Constraint (2.3c) owing to the minimum turndown of molten salt pumps. In the absence of thermal power, the receiver is not able to operate (Constraint (2.3d)).

Standby mode allows molten salt to be circulated between the TES tanks and the receiver such that a restart can occur quickly; such a restart incurs a smaller financial penalty. Constraints (2.4a) and (2.4b) preclude (i) standby and start-up modes and (ii) standby and power-producing modes from coinciding. Standby mode can only occur in time periods directly after which the receiver was either in standby or power-producing mode (Constraint (2.4c)). Constraints (2.4d) and (2.4e) ensure that penalties for receiver start-up from an off or from a standby state are incurred, respectively. Constraint (2.4f) implements shut-down logic related to power-producing or standby states. Constraints (2.12a)-(2.12c) and (2.12e) enforce domain requirements on the variables except for x_t^r whose non-negativity is ensured via Constraints (2.3c).

2.4.2.2 Power Cycle Operations

Power cycle operation constraints are similar to those of receiver operations:

Cycle Start-up

$$u_t^{csu} \leq u_{t-1}^{csu} + \Delta Q^c y_t^{csu} \qquad \forall\, t \in \mathcal{T} : t \geq 2 \tag{2.5a}$$

$$u_t^{csu} \leq E^c y_t^{csu} \qquad \forall\, t \in \mathcal{T} \tag{2.5b}$$

$$y_t \leq \frac{u_{t-1}^{csu}}{E^c} + y_{t-1} + y_{t-1}^{csb} \qquad \forall\, t \in \mathcal{T} : t \geq 2 \tag{2.5c}$$

$$x_t \leq Q^u y_t \qquad \forall\, t \in \mathcal{T} \tag{2.5d}$$

$$x_t \geq Q^l y_t \qquad \forall\, t \in \mathcal{T} \tag{2.5e}$$

Power Supply and Demand

$$\dot{w}_t = \frac{\eta_t^{amb}}{\eta^{des}}[\eta^p x_t + (W^u - \eta^p Q^u) y_t] \qquad \forall\, t \in \mathcal{T} \tag{2.6a}$$

$$\dot{w}_t^{\delta} \geq \dot{w}_t - \dot{w}_{t-1} \qquad \forall\, t \in \mathcal{T} : t \geq 2 \tag{2.6b}$$

$$\dot{w}_t^{\delta} \geq \dot{w}_{t-1} - \dot{w}_t \qquad \forall\, t \in \mathcal{T} : t \geq 2 \tag{2.6c}$$

$$\dot{w}_t^{\delta} \leq \delta W^{lim} \qquad \forall\, t \in \mathcal{T} \tag{2.6d}$$

$$\dot{w}_t^{s} \leq W_t^{net} \qquad \forall\, t \in \mathcal{T} \tag{2.6e}$$

$$\begin{aligned} \dot{w}_t^s - \dot{w}_t^p = \dot{w}_t(1 - \eta_t^c) + \frac{\dot{w}_t^- - \alpha^- y_t^-}{1 + \beta^-} \\ -[(1 + \beta^+)\dot{w}_t^+ + \alpha^+ y_t^+] + \frac{\dot{w}_t^{pv} - \dot{w}_t^{pv+} - \alpha^{pv} y_t^{pv}}{1 + \beta^{pv}} \\ -L^r(x_t^r + x_t^{rsu} + Q^{rl} y_t^{rsb}) - L^c x_t - W^h y_t^r - W^b y_t^{csb} \\ -W^{ht} y_t^{rsu} - \frac{E^{hs}}{\Delta}\left(y_t^{rsu} + y_t^{rsb} + y_t^{rsd}\right) \qquad \forall\, t \in \mathcal{T} \end{aligned} \tag{2.6f}$$

Logic Governing Cycle Modes

$$y_t^{csu} + y_{t-1} \leq 1 \qquad \forall\, t \in \mathcal{T} : t \geq 2 \tag{2.7a}$$

$$y_t + y_t^{csu} \leq 1 \qquad \forall\, t \in \mathcal{T} \tag{2.7b}$$

$$y_t^{csb} \leq y_{t-1} + y_{t-1}^{csb} \qquad \forall\, t \in \mathcal{T} : t \geq 2 \tag{2.7c}$$

$$y_t^{csu} + y_t^{csb} \leq 1 \qquad \forall\, t \in \mathcal{T} \tag{2.7d}$$

$$y_t + y_t^{csb} \leq 1 \qquad \forall\, t \in \mathcal{T} \tag{2.7e}$$

$$y_t^{chsp} \geq y_t - (1 - y_{t-1}^{csb}) \qquad \forall\, t \in \mathcal{T} : t \geq 2 \tag{2.7f}$$

$$y_t^{csd} \geq y_{t-1} - y_t + y_{t-1}^{csb} - y_t^{csb} \qquad \forall\, t \in \mathcal{T} : t \geq 2 \tag{2.7g}$$

$$y_t^{csup} \geq y_t^{csu} - y_{t-1}^{csu} \qquad \forall\, t \in \mathcal{T} : t \geq 2 \tag{2.7h}$$

Constraint (2.5a) accounts for start-up energy "inventory," which can only be positive during time periods in which the cycle is starting up (Constraint (2.5b)). Normal cycle

operation can occur upon completion of start-up energy requirements, if the cycle is operating normally, or directly after stand-by mode (Constraint (2.5c)). Constraint (2.5d) and Constraint (2.5e) form the upper and lower bounds on the heat input to the power cycle, respectively. The relationship between electrical power and cycle heat input is modeled as a linear function with corrections for ambient temperature effects (Constraint (2.6a)). Constraints (2.6b) and (2.6c) measure the change in the production of electrical power over time. Constraints (2.6d) and (2.6e) limit the cycle ramping rate and grid transmission for net power production, respectively. Positive and negative power flow (corresponding to sold and purchased electricity, respectively) is determined by a power balance on the AC bus of the hybrid system (Constraint (2.6f)). The right-hand side of Constraint (2.6f) consists of the following terms, in the order in which they appear: (i) power cycle generation less condenser parasitic power, (ii) battery discharge power accounting for DC-to-AC conversion losses, (iii) battery charge power accounting for AC-to-DC conversion losses, (iv) PV field generation less power used for battery charging directly from the field, accounting for inverter losses, (v) TES pumping power requirements for receiver operations, (vi) TES pumping power requirements for cycle operation, (v) heliostat tracking power, (vi) power cycle standby parasitic power, (vii) tower piping heat trace for receiver start-up, and (viii) heliostat field stow power for different receiver operations.

Constraint (2.7a) precludes power cycle start-up in consecutive time periods of power-producing operation. Constraint (2.7b) precludes power cycle start-up and operation from coinciding. The cycle-standby-mode constraint (Constraint (2.7c)) is analogous to that for the receiver. Standby and start-up modes cannot simultaneously occur (Constraint (2.7d)); this also holds for standby and power-producing modes (Constraint (2.7e)). Constraints (2.7f) and (2.7g) implement the following logic, respectively: (i) starting up after standby and (ii) shutting down after producing power or standing by. Penalties incurred from a cycle cold start are incurred via Constraint (2.7h). Constraints (2.12a)-(2.12c) and (2.12f) enforce domain requirements on the variables except for x_t whose non-negativity is ensured

via Constraint (2.5e).

2.4.2.3 TES Energy Balance

The system's energetic state implies power terms that can assume either sign; the thermal storage charge state (s_t) reconciles their difference. We therefore impose some additional constraints with respect to TES state of charge:

TES State of Charge

$$s_t - s_{t-1} = \Delta[x_t^r - (Q^c y_t^{csu} + Q^b y_t^{csb} + x_t + Q^{rsb} y_t^{rsb})] \quad \forall\, t \in \mathcal{T} : t \geq 2 \tag{2.8a}$$

$$s_t \leq E^u \quad \forall\, t \in \mathcal{T} \tag{2.8b}$$

$$s_{t-1} \geq \Delta \cdot \Delta_t^{rs}[\mathbb{M}(-3 + y_t^{rsu} + y_{t-1} + y_t + y_{t-1}^{csb} + y_t^{csb}) + x_t + Q^b y_t^{csb}] \quad \forall\, t \in \mathcal{T} : t \geq 2 \tag{2.8c}$$

Constraint (2.8a) balances energy to and from TES with the charge; a time-scaling parameter Δ reconcils power and energy. Constraint (2.8b) imposes the upper bound to TES charge state. If the power cycle is operating or standing by in time period $t-1$ or t, and if the receiver is starting up in time t, then there must be a sufficient charge level in the TES in time $t-1$ to ensure that the receiver can operate through its start-up period (Constraint (2.8c)). The expected fraction of a time period used for receiver start-up is given by (2.9), if applicable.

$$\Delta_t^{rs} = \min\left\{1, \max\left\{\Delta^l, \frac{E^c}{\max\left\{\epsilon, Q_{t+1}^{in}\Delta\right\}}\right\}\right\} \tag{2.9}$$

Constraints (2.8a)-(2.8c) measure TES state of charge via energy flow. (Introducing energy quality as a function of the molten salt temperature yields a non-linearity that, at the time of this writing, is a level of detail not worth the extra computational effort.)

2.4.2.4 Battery and Photovoltaic Field Operations

Lithium-ion and lead-acid batteries store energy. A lithium-ion battery outperforms a lead acid battery because, relative to a lead acid battery: (i) the lithium-ion battery commonly uses 80% of its available capacity, compared to 50% for a lead-acid battery; (ii)

throughout the life of the lithium-ion battery, it is expected to deliver twice the number of cycles; (iii) the lithium-ion battery has a faster and more efficient charging process; (iv) the charging efficiency of the lithium-ion battery is 100% compared to 85% for a lead-acid battery; (v) a lithium-ion battery is less susceptible to storage issues and leaks; (vi) a lithium-ion battery is less affected by ambient temperature; (vii) there are fewer maintenance requirements associated with a lithium-ion battery; and (viii) a lithium-ion battery weighs less and is smaller than a lead-acid battery per unit capacity [54, 55]. A lithium-ion battery is rechargeable and uses lithium ions to store or release electrical energy. When charging a lithium-ion battery, lithium ions move from the cathode to the anode. These ions move in the other direction, from the anode to the cathode, to release the stored energy and produce electrical energy. We use a lithium-ion battery in our analysis because of the benefits mentioned above.

The addition of a PV and battery system to CSP enhances dispatch flexibility. The lithium-ion battery being used in this hybrid system is connected to PV and reacts quickly to changes in net demand, as is shown in the green box on the left-hand side of the connection layout in Figure 2.2. The battery can either be charged directly from the PV system or through the rectifier connected to the AC bus; it discharges its energy through the inverter. We connect several 3.4 amp-hour lithium-ion cells to create the battery whose voltage is calculated for lithium-ion cells in series and should match that of the DC (direct current) system; buck-boost voltage converters adjust the battery's voltage output. The capacity of the battery is determined by placing the lithium-ion cells in parallel. The battery is connected to an inverter to convert the current from DC to AC. The inverter is sized so as not to constitute the bottleneck such that power output is limited. Depending on the configuration of the overall CSP and PV hybrid system, multiple converters may be needed.

Battery Operations

$$\dot{w}_t^+ + \dot{w}_t^{pv+} = v_t^{soc} i_t^+ \qquad \forall\, t \in \mathcal{T} \tag{2.10a}$$
$$\dot{w}_t^- = v_t^{soc} i_t^- \qquad \forall\, t \in \mathcal{T} \tag{2.10b}$$
$$b_t^{soc} = b_{t-1}^{soc} + \Delta \left(\frac{i_t^+ - i_t^-}{C^B} \right) \qquad \forall\, t \in \mathcal{T} : t \geq 2 \tag{2.10c}$$
$$\underline{S}^B \leq b_t^{soc} \leq \bar{S}^B \qquad \forall\, t \in \mathcal{T} \tag{2.10d}$$
$$v_t^{soc} = A^V b_{t-1}^{soc} + B^V \left(y_t^+ + y_t^- \right) + I^{avg} R^{int} \left(y_t^+ - y_t^- \right) \qquad \forall\, t \in \mathcal{T} : t \geq 2 \tag{2.10e}$$
$$\underline{P}^B y_t^- \leq \dot{w}_t^- \leq \bar{P}^B y_t^- \qquad \forall\, t \in \mathcal{T} \tag{2.10f}$$
$$\underline{P}^B y_t^+ \leq \dot{w}_t^+ + \dot{w}_t^{pv+} \leq \bar{P}^B y_t^+ \qquad \forall\, t \in \mathcal{T} \tag{2.10g}$$
$$i_t^- \leq I^{U-} b_{t-1}^{soc} \qquad \forall\, t \in \mathcal{T} : t \geq 2 \tag{2.10h}$$
$$i_t^+ \leq C^B \left(\frac{1 - b_{t-1}^{soc}}{\Delta} \right) \qquad \forall\, t \in \mathcal{T} : t \geq 2 \tag{2.10i}$$
$$I^{L-} y_t^- \leq i_t^- \leq I^{U-} y_t^- \qquad \forall\, t \in \mathcal{T} \tag{2.10j}$$
$$I^{L+} y_t^+ \leq i_t^+ \leq I^{U+} y_t^+ \qquad \forall\, t \in \mathcal{T} \tag{2.10k}$$
$$y_t^+ + y_t^- \leq 1 \qquad \forall\, t \in \mathcal{T} \tag{2.10l}$$
$$b^c \geq \frac{\Delta}{C^B} \sum_{t \in \mathcal{T}} [\gamma^t (i_t^+ - i_t^+ b_{t-1}^{soc})] \tag{2.10m}$$

The nonlinear relationships between power, current, and voltage are represented by Constraints (2.10a) and (2.10b) for charging and discharging, respectively. (See [53] for the associated linearization techniques.) Battery state-of-charge must be updated (Constraint (2.10c)), and this quantity is bounded both below and above (Constraint (2.10d)). Battery voltage is given by its current flow direction and previous state of charge (Constraint (2.10e)); the voltage is linear for a state of charge specified by Constraint (2.10d). Net power flow is bounded by Constraints (2.10f) and (2.10g). Constraints (2.10h) through (2.10k) restrict current flow. The battery cannot be charging and discharging simultaneously (Constraint (2.10l)) while Constraint (2.10m) measures battery cycle count similar to what is done in [42].

Photovoltaic Field Operations

$$\dot{w}_t^{pv} \leq W_t^{DC} y_t^{pv} \qquad \forall\, t \in \mathcal{T} \tag{2.11a}$$
$$\dot{w}_t^{pv} - \dot{w}_t^{pv+} \leq W^I y_t^{pv} \qquad \forall\, t \in \mathcal{T} \tag{2.11b}$$
$$\dot{w}_t^{pv+} \leq \dot{w}_t^{pv} \qquad \forall\, t \in \mathcal{T} \tag{2.11c}$$

PV curtailment is a process in which PV controls are purposefully set below the maximum power point of the PV modules. Constraint (2.11a) allows for curtailment by imposing only an upper limit on PV field generation. PV clipping is a process in which the rated power of the PV modules is larger than the inverter-rated power. When the difference between power produced by the PV field and power sent directly to the battery is greater than the inverter-rated power, the excess is lost or clipped (Constraint (2.11b)). Power sent to charge the battery directly from the PV field is limited by PV field generation (Constraint (2.11c)). Constraints (2.12b) and (2.12g) enforce domain requirements on the battery and PV field variables except for b^c whose non-negativity is ensured via Constraint (2.12d).

2.4.2.5 Variable Bounds

Variable bounds are enforced in (2.12a)-(2.12g).

$$u_t^{csu},\ u_t^{rsu},\ \dot{w}_t,\ \dot{w}_t^{p},\ \dot{w}_t^{s},\ x_t^{r},\ x_t^{rsu} \geq 0 \qquad \forall\ t \in \mathcal{T} \tag{2.12a}$$

$$b_t^{soc},\ i_t^{+},\ i_t^{-},\ v_t^{soc},\ \dot{w}_t^{pv},\ \dot{w}_t^{pv+},\ \dot{w}_t^{+},\ \dot{w}_t^{-} \geq 0 \qquad \forall\ t \in \mathcal{T} \tag{2.12b}$$

$$s_t, \dot{w}_t^{\delta}, x_t \geq 0 \qquad \forall\ t \in \mathcal{T} \tag{2.12c}$$

$$b^c \geq 0 \tag{2.12d}$$

$$y_t^{r},\ y_t^{rhsp},\ y_t^{rsb},\ y_t^{rsd},\ y_t^{rsu},\ y_t^{rsup} \in \{0,1\} \qquad \forall\ t \in \mathcal{T} \tag{2.12e}$$

$$y_t,\ y_t^{chsp},\ y_t^{csb},\ y_t^{csd}, y_t^{csu},\ y_t^{csup} \in \{0,1\} \qquad \forall\ t \in \mathcal{T} \tag{2.12f}$$

$$y_t^{+},\ y_t^{-},\ y_t^{pv} \in \{0,1\} \qquad \forall\ t \in \mathcal{T} \tag{2.12g}$$

2.5 Solution Techniques

The hybrid dispatch optimization model ($\mathcal{H}$) is implemented within the SAM framework developed by the National Renewable Energy Laboratory in a manner shown in Figure 2.3. A Python wrapper is used to specify system design inputs directly without use of the graphical interface and invoke SAM's simulation core for both photovoltaic and CSP power tower molten salt modules, enabling annual simulation of PV-CSP hybrids. The Python script contains decision logic that determines which processes is executed based on the program

inputs. This decision logic adds flexibility of system designs to be explored. For example, if the hybrid plant includes some amount of PV, the script executes SAM's detailed PV simulation module based on the user's inputs. Upon completion, PV parameters used in ($\mathcal{H}$) are stored in data files to be used during hybrid dispatch. If a battery exists in the system, the script calculates design parameters such as the number of cells and their configuration, operation limits, and performance curve fits, and stores them in a data file to be used during hybrid dispatch.

After the PV annual performance simulation has been run, the SAM simulation core generates estimates for the time-indexed parameters specified in Table 2.1; the dispatch model ($\mathcal{H}$) yields an optimal schedule over the immediate 48-hour planning horizon, which prescribes operational targets for the receiver and power cycle, yielding guidance for SAM's simulation core over the next 24 hours. After moving forward 24 hours, the simulation core repeats the process and generates another look-ahead dispatch problem to be solved until an annual simulation, comprised of 365 dispatch problem instances, is complete. Wagner et al. [11] provide a detailed description of the software architecture and rolling time horizon solution methodology for a CSP-only system. After the CSP simulation is complete, the annual time-series generation vector provided by SAM is consolidated to include CSP, PV, and battery operations.

Due to the number of dispatch problem instances required for an annual simulation, individual ($\mathcal{H}$) instances must solve quickly for a hybrid design to be evaluated in a timely manner. Solving the sub-hourly dispatch problem ($\mathcal{H}$) in its original form, as described in Section 2.4, to a MILP gap of 1×10^{-3} is computationally burdensome. To increase tractability, we implement three major solution techniques, the first two of which are exact and the third is not: (i) problem size reduction, (ii) tighter LP relaxation, and (iii) heuristic solution approach.

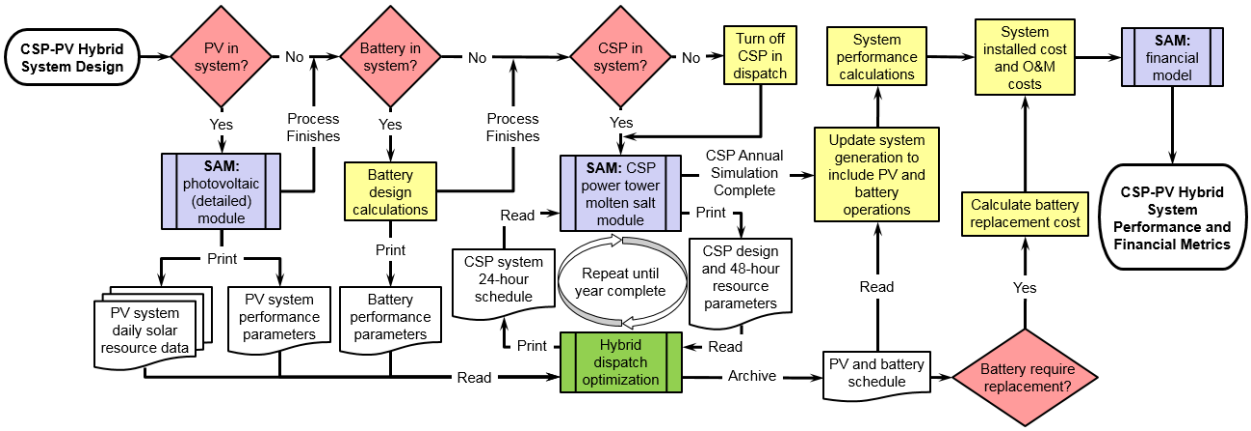

Figure 2.3: Flow diagram of the software architecture implemented around the hybrid dispatch optimization model ($\mathcal{H}$)

2.5.1 Problem Size Reduction

To reduce the overall problem instance size (i.e., number of variables and constraints), we reformulate ($\mathcal{H}$) such that it consists of windows with two different time fidelities over the course of the horizon: (i) sub-hourly fidelity for the first 24 hours that corresponds to that of the input weather file (i.e., 10-minute); and (ii) hourly time fidelity for the remainder of the horizon, which mimics the day-ahead energy market used to make future unit commitment decisions (see Figure 2.4). To implement this reformulation, we introduce a new set, $\mathcal{W}$, defined as a set of time windows within the time horizon, i.e., $\mathcal{W} = \{1, 2\}$. Each window, $w \in \mathcal{W}$, contains a time step duration, Δ_w, and a set of time periods, $\mathcal{T}_w$. The union of the time period sets comprises the complete time horizon, i.e., $\mathcal{T}_1 \cup \mathcal{T}_2 = \mathcal{T}$. This reformulation methodology improves tractability of the problem instances by reducing the theoretical problem size by 2,280 continuous variables, 1,800 binary variables, and 8,640 constraints, which corresponds to a 41.6% decrease in each case.

For the hourly time fidelity window, $w = 2$, we aggregate time-indexed parameters by taking the simple mean over the values for each time period within the hour; the lone exception is the parameter Δ_t^{rs}, which is recalculated using equation (2.9) and the updated aggregated value of Q_{t+1}^{in}. The majority of formulation ($\mathcal{H}$) is valid for both time windows. However, we

modify Constraints (2.4f), (2.5c), (2.7b), and (2.6d) to reflect operational changes between modeling the system at hourly versus sub-hourly fidelity. The left-hand side of Constraint (2.4f) is adjusted to index the previous time period:

$$y^{rsd}_{t-1} \geq (y^{r}_{t-1} - y^{r}_{t}) + (y^{rsb}_{t-1} - y^{rsb}_{t}) \quad \forall\ t \in \mathcal{T}_2 \tag{2.13}$$

which results in receiver shutdown operations occurring during the same time period as the last production or standby operation. In Constraint (2.5c), the time index on the variable u^{csu}_{t-1} is adjusted to the current time period:

$$y_t \leq \frac{u^{csu}_{t}}{E^c} + y_{t-1} + y^{csb}_{t-1} \quad \forall\ t \in \mathcal{T}_2 \tag{2.14}$$

which results in cycle start-up and operation occurring in the same time period. We add a constraint that ensures that the cycle input energy limit is not exceeded:

$$x_t + Q^c y^{csu}_t \leq Q^u \quad \forall\ t \in \mathcal{T}_2 \tag{2.15}$$

which results in limited cycle energy production for the time period during which the cycle is starting up. Constraint (2.7b) must be removed to allow for cycle startup and energy production to occur during the same time period. Constraint (2.6d) is removed because we assume that the power cycle can ramp from minimum to maximum power output within a hour. The original forms of Constraints (2.4f), (2.5c), (2.7b), and (2.6d) still hold for the sub-hourly window, i.e., $t \in \mathcal{T}_1$. The union of ($\mathcal{H}$) and Constraints (2.13), (2.14), and (2.15) form the reduced hybrid dispatch problem.

We also reduce the size of our problem by eliminating variables that could not assume values other than zero in any feasible solution during time periods with no solar resource (e.g., night time). For example, the decision to operate the CSP receiver, y^r_t, can be preprocessed out during periods in which solar resource, Q^{in}_t, is zero.

2.5.2 Tighter LP Relaxation

Our formulation in Section 2.4 is weak owing to Constraints (2.5c), (2.6f), (2.7c) - (2.7g), (2.8a), and (2.8c), specifically, with respect to the binary variables for cycle start-up and

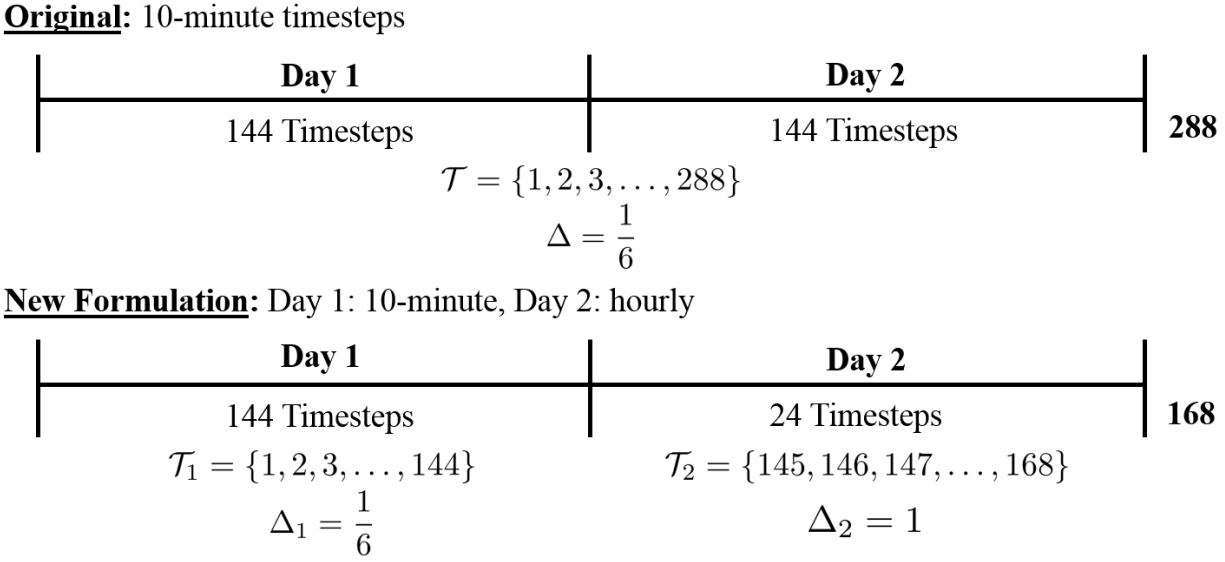

Figure 2.4: The original formulation has sub-hourly time periods throughout the problem's time horizon. The reformulated model possesses sub-hourly time periods during the first 24 hours and aggregates data to hourly fidelity for the second 24 hours.

standby. Cycle standby is an operational mode that allows the CSP power cycle to stay in a "hot" state by consuming TES but without generating electric power. From this operational state, the cycle can quickly come back on-line, generating power at a reduced start-up cost. Both cycle start-up and standby are indirectly related to the objective through the fixed-cost penalty.

To tighten the LP relaxation, thereby improving the guarantee of optimality, we introduce a binary variable, y_t^{off} that is defined as one if the power cycle is in an "off" state and zero otherwise, and reformulate the dispatch problem to include set partitioning Constraints (2.16) and (2.17):

$$y_t^{csu} + y_t + y_t^{csb} + y_t^{off} = 1 \quad \forall\, t \in \mathcal{T}_1 \tag{2.16}$$

$$y_t + y_t^{csb} + y_t^{off} = 1 \quad \forall\, t \in \mathcal{T}_2 \tag{2.17}$$

which results in a tighter LP relaxation because the cycle must be in one and only one of these operational state during any time period.

To further strengthen our formulation, we develop a cut that forces the cycle standby operation binary variable, y_t^{csb}, to zero when the TES heat to the cycle, x_t, is equal to its upper bound Q^u, i.e., the power cycle is operating at full load:

$$y_t^{csb} \leq 1 - \frac{x_t}{Q^u} \quad \forall\ t \in \mathcal{T} \tag{2.18}$$

The introduction of the binary variable, y_t^{off}, the set partitioning constraints, and cycle standby cut reduce solution times of certain problem instances, as shown in Section 2.6.

2.5.3 Heuristic Solution Approach

To further reduce our solution times, we implement a two-phase heuristic solution technique, which we call $\hat{\mathbf{H}}$, shown in Figure 2.5. In Phase 1, we set battery discharge power to zero, i.e., $\dot{w}_t^- = 0 \quad \forall \quad t \in \mathcal{T}$, effectively removing battery operation decisions, and solve the dispatch problem. The resulting solution represents operations of the CSP field, CSP power cycle, and PV field generation without accounting for battery interactions. This problem solves relatively quickly and can provide a lower bound on the objective function value of the monolith, ($\mathcal{H}$). In Phase 2, we hold the power cycle standby decisions constant (i.e., y_t^{csb}), unfix battery discharge power, and re-solve the dispatch problem using the integer solution from the first solve as a warm start.

In practice, executing $\hat{\mathbf{H}}$ allows for faster solve times because the two sub-problems are computationally less expensive than solving the whole problem at once. Despite being a heuristic, $\hat{\mathbf{H}}$ produces near-optimal solutions because the interaction between cycle standby and battery operations is weak.

2.6 Results

The dispatch model ($\mathcal{H}$) is written in the AMPL modeling language version 20210630 [56] and solved using CPLEX version 12.8 [57]. Hardware architecture to generate solutions and solve times consists of a SuperServer 1028GR-TR server with an Intel Xeon E5-2620 v4s at 2.1 GHz, running Ubuntu 16.04 with 128 GB of RAM, 1 250 GB SSD, and 3 500 GB

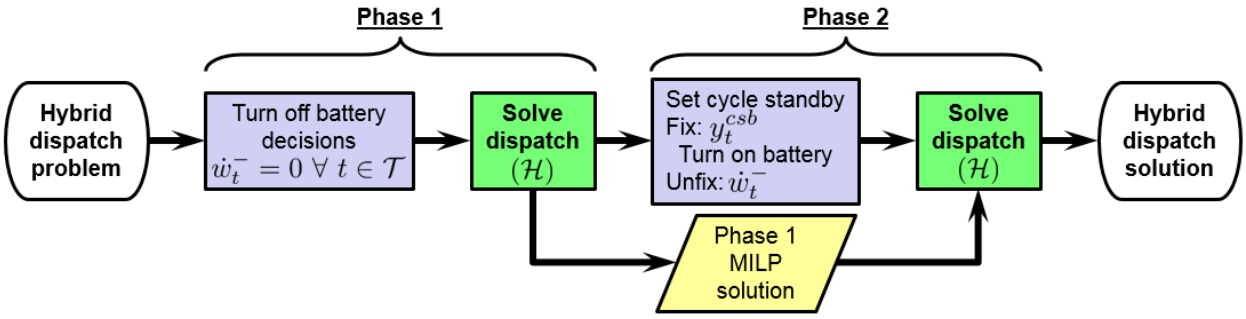

Figure 2.5: Flow diagram of the two-phase solution technique, using heuristic $\hat{\mathbf{H}}$. The solution to Phase 1 is given to Phase 2 as an initial feasible solution.

SSDs hard dives.

2.6.1 Case Study Inputs

Designing a hybrid system for a specific location or market is beyond the scope of this work; therefore, we compare the dispatch of a fixed CSP-TES-PV-battery hybrid plant design in two locations and two electricity markets.

2.6.1.1 Hybrid System Design

The hybrid system of study is grid-limited and requires the dispatch of individual sub-systems (i.e., power cycle and battery) to ensure that the transmission power limit of 310 MW_e is not exceeded. The CSP sub-system consists of two twin molten salt power tower CSP plants, each with a power cycle capable of 163 MW_e output with 12 hours, or 4,716 MWh_t, of thermal storage and a receiver capable of 565 MW_t production. The PV sub-system consists of a single-axis tracking PV field capable of 325 MW_{dc} production with a maximum inverter power output of 270 MW_{ac}. The battery sub-system has a capacity of 150 MWh_e with a maximum discharge rate of 1C, where we define the C-rate as the rate at which a battery is discharged relative to its maximum capacity; this is equal to the amount of current one is able to extract in one hour from a battery that is in a fully charged state. In our context, this equates to a maximum discharge power of 150 MW_e. Table 2.3 summarizes design parameters and defines operational limits. Given solar resource and receiver-rated thermal

power, SolarPILOT [58] generates the CSP heliostat field layout for the two locations.

Table 2.3: Case study plant design. ‡The plant consists of two CSP systems. †Used to derive the subset of parameters in Table 2.1 not listed in Table 2.3 or Table 2.4.

Parameter	**Symbol**	**Units**	**Value**
For a single CSP system‡:			
Cycle design thermal input	Q^u	MW_t	393
Cycle maximum gross output	W^u	MW_e	163
Cycle minimum gross output	†	MW_e	36.4
Cycle start-up energy consumption	E^c	MWh_t	197
Cycle minimum start-up time	†	hr	0.50
Cycle standby consumption	Q^b	MW_t	78.6
Receiver maximum/design thermal output	†	MW_t	565
Receiver minimum output	†	MW_t	141
Receiver start-up energy	E^r	MWh_t	141
Receiver minimum star-up time	†	hr	0.25
Thermal energy storage capacity	E^u	MWh_t	4716
PV and battery system:			
PV field capacity	†	MW_{dc}	325
PV inverter maximum output	†	MW_{ac}	270
Battery capacity	†	MWh_e	150
Battery maximum power output	$\bar{P}^B$	MW_e	150
Whole system:			
Net grid transmission maximum power limit for time t	W_t^{net}	MW_e	310

2.6.1.2 Operating Costs

The system dispatch is determined by maximizing revenue at minimum operating cost. Due the nature of maximizing revenue, sub-system operating costs are required to enable decision making between the different energy generation technologies. Table 2.4 summarizes the operating cost of each sub-system. Receiver start-up cost is estimated at \$10/MW_t of the receiver design thermal power. Receiver operating costs are estimated based on the heliostat field and receiver annual O&M costs and thermal energy generation, assuming daily start-ups. Power cycle operation, start-up, and change-in-production (ramping) costs are adapted from Kumar et al. [59]. Hot start-up costs of the receiver, C^{rhsp}, and power cycle, C^{chsp}, are assumed to be 10% of cold start-up costs. Battery life cycle costs penalize cycling during

periods when there is excess generation capacity. There is uncertainty associated with all of the operating cost values described above. However, it is the relative magnitude of these costs that is important in deciding which technologies should be used to generate electricity at any given time period and, for days on which there is abundant solar resource, these costs determine which technology should be curtailed. For example, due to the low operating cost of PV systems, it is better to curtail CSP receiver generation and/or power cycle generation than PV field generation during abundant solar resource days. These operating costs also indicate that it is more economically advantageous to charge the battery system using the PV field rather than the CSP power cycle.

Table 2.4: Estimated CSP-TES-PV-battery hybrid operating costs

Operating Costs and Penalties	**Symbol**	**Units**	**Value**
CSP system:			
Heliostat field and receiver	C^{rec}	$\$/\text{MWh}_\text{t}$	3
Receiver cold start-up	C^{rsu}	\$/start	5650
Power cycle	C^{pc}	$\$/\text{MWh}_\text{e}$	2
Power cycle cold start-up	C^{csu}	\$/start	6520
Power cycle change in production	$C^{\delta W}$	$\$/\Delta\text{MW}_\text{e}$	0.71
Power cycle standby	C^{csb}	$\$/\text{MWh}_\text{t}$	0.80
PV and battery system:			
Photovoltaic field	C^{pv}	$\$/\text{MWh}_\text{e}$	0.50
Battery charge/discharge	C^{bc}/C^{bd}	$\$/\text{MWh}_\text{e}$	1
Battery lifecycle	C^{bl}	\$/lifecycle	250

2.6.1.3 Battery Specifications

We take parameter values used to model the lithium-ion battery from Husted et al. [53], who models another type of hybrid system involving diesel generators, photovoltaics and a battery in a microgrid setting; see Table 2.5.

2.6.2 Numerical Experiment

The following analysis explores the performance and market outcomes for a fixed hybrid system design at two locations and in two markets. Although location (weather) and market

Table 2.5: Battery Cell Ratings

Battery Specifications	Value	Units
Cell Max Charge Voltage	4.1355	V
Cell End of Discharge Voltage	3.2768	V
Cell Nominal Voltage	3.70615	V
Cell Amp Hour Rating	3.4	Ah
Cell Internal Resistance	0.1394	Ω

are typically highly correlated, we evaluate all four market-location combinations to demonstrate the robustness of the solution techniques and to provide an understanding of how a single design might operate differently depending on its location and market conditions. The analysis is posed as a two-factor, two-level, numerical experiment.

2.6.2.1 Plant Location

The location of the hybrid plant affects its performance and profitability. Geographic location determines the solar resource availability for electricity generation. For our case study, we choose northern Chile (N. Chile) and southern Nevada (S. Nevada) as the two levels for the *location* factor, the former location owing to its high solar resource and our industry partner's interest in the development of hybrid plants within this region and the latter region owing to its solar resource and the availability of sub-hourly (i.e., one-minute time scale) solar data [60].

The University of Nevada – Las Vegas (UNLV) weather station does not measure relative humidity or atmospheric pressure, two inputs required to model power cycle performance. However, Nevada Power Clark Station [61], which is 5.2 miles, as measured by its straight-line distance from UNLV, reports relative humidity. Due to the low spatial variability, we can safely use the measurements of relative humidity from the Clark station with solar resource data from the UNLV station without introducing error into our calculations. For atmospheric pressure, we use an hourly typical meteorological year for Las Vegas and assume that atmospheric pressure remains constant at the sub-hourly level. The UNLV solar data

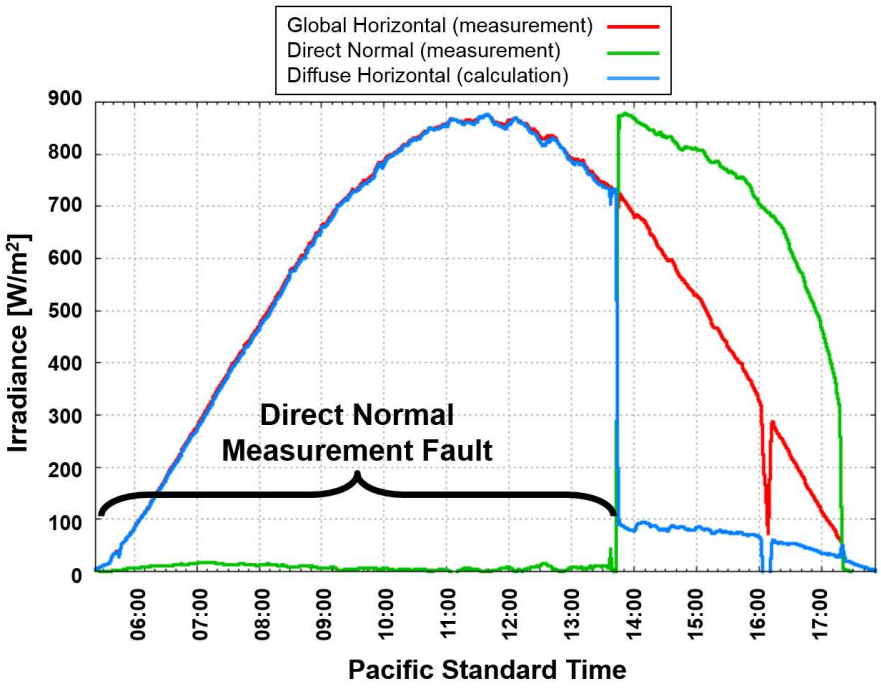

Figure 2.6: Example of UNLV data (taken from [60]) of which the pyroheliometer or tracking system had faulted.

reveals time periods in which the pyrheliometer instrument or the tracking system had faulted. Figure 2.6 shows an instance of the measurement fault in direct normal irradiance from the beginning of the solar day to approximately 13:40 PST, where the global horizontal irradiance measurements are close to clear-sky values with little-to-no measured direct normal irradiance. Therefore, we choose our data set to consist of twelve fault-free months, which spans June 2012 to May 2013. These three data sources constitute an annual sub-hourly (i.e., 10-minute) weather file for S. Nevada.

The duration curve in Figure 2.7 compares the direct normal irradiance for N. Chile and S. Nevada using a sorted histogram. The yearly totals for the three solar irradiance resources are given in Table 2.6. N. Chile has a higher solar resource than S. Nevada because the area has low atmospheric attenuation. S. Nevada has higher annual diffuse irradiance because there are more days with cloud cover than N. Chile. CSP systems can exploit direct normal irradiance, while PV systems generate electricity from both direct normal and diffuse horizontal irradiance.

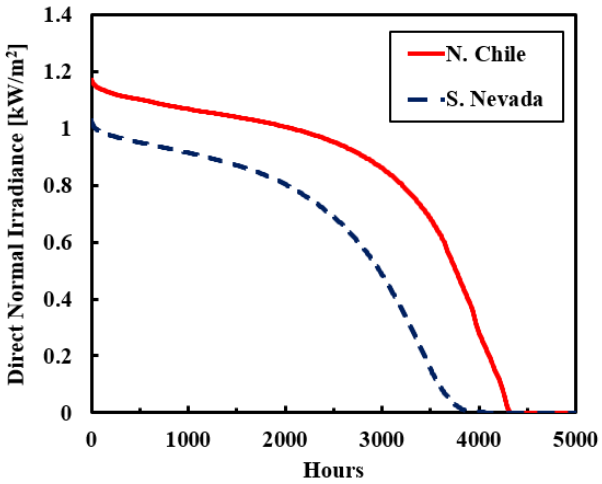

Figure 2.7: Sorted histogram of the direct normal irradiance for N. Chile and S. Nevada.

Table 2.6: Solar global horizontal, direct normal, and diffuse horizontal irradiance year totals for N. Chile and S. Nevada.

	Global Horizontal [kWh/m^2/year]	**Direct Normal** [kWh/m^2/year]	**Diffuse Horizontal** [kWh/m^2/year]
N. Chile	3782.1	2730.4	353.4
S. Nevada	2682.9	2083.2	490.4

2.6.2.2 Electricity Markets

The electricity market into which the plant bids affects the dispatch strategy due to the time-of-use price of electricity. For our factorial experiment, we choose the N. Chile spot market (NC spot) and the 2016 Pacific Gas & Electric (PG&E) market as the two levels for the *market* factor, the former owing to our industry partner's interest, and the latter owing to its simple design and the possibility that a plant in southern Nevada may be designed to dispatch against such a market.

Figure 2.8 compares the two markets using a sorted histogram of normalized electricity prices. Both markets follow a similar price trend. However, the PG&E market has more high-price and more highly priced hours relative to those in the NC spot market. Figure 2.9 depicts the time-of-use variation of the NC spot and PG&E markets. The NC spot market exhibits hourly, monthly, and week-versus-weekend variation in the electricity price, shown

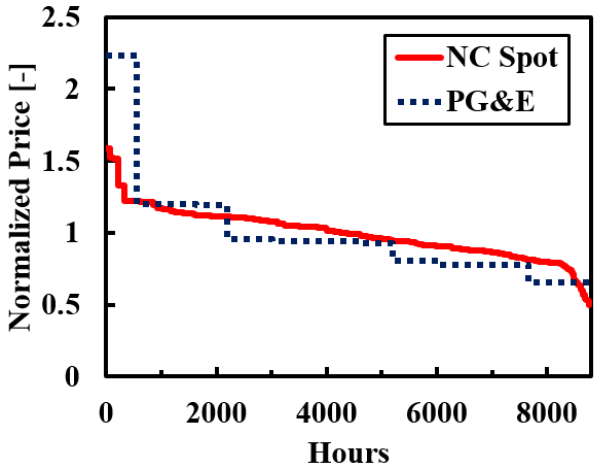

Figure 2.8: Sorted histogram of the normalized prices for N. Chile spot (NC spot) and Pacific Gas & Electric (PG&E) full capacity deliverability markets.

in Figure 2.9(a). Generally, high-price time periods occur at the end of the solar day during the winter and spring, e.g., July through December. During the fall (April through June), the NC spot market possesses relatively flat prices– either slightly above or below the annual average. The PG&E market has only hourly and seasonal variation, with the high-price time periods occurring between the hours of 4 and 9 p.m. The highest values occur during the months of July, August, and September.

Due to the seasonal variation in both markets and plant locations being in both the northern and southern hemispheres, we shift the market by six months when evaluating the location-market combinations of N. Chile in a PG&E market and S. Nevada in a NC spot market. This seasonal shift is done by appending the first 181 days (i.e., first six months) of the year to the end of the last 184 days (i.e., last six months) of the year. This method does not preserve the monthly transitions present in the original price structure. However, it does allow for comparison between the original markets because this shift does not change the number of time periods that exhibit a particular price.

2.6.3 Solve Times and Solution Quality

Each location-market combination in the numerical experiment requires 365 instances of the dispatch problem ($\mathcal{H}$) to be solved to produce annual system performance results. We

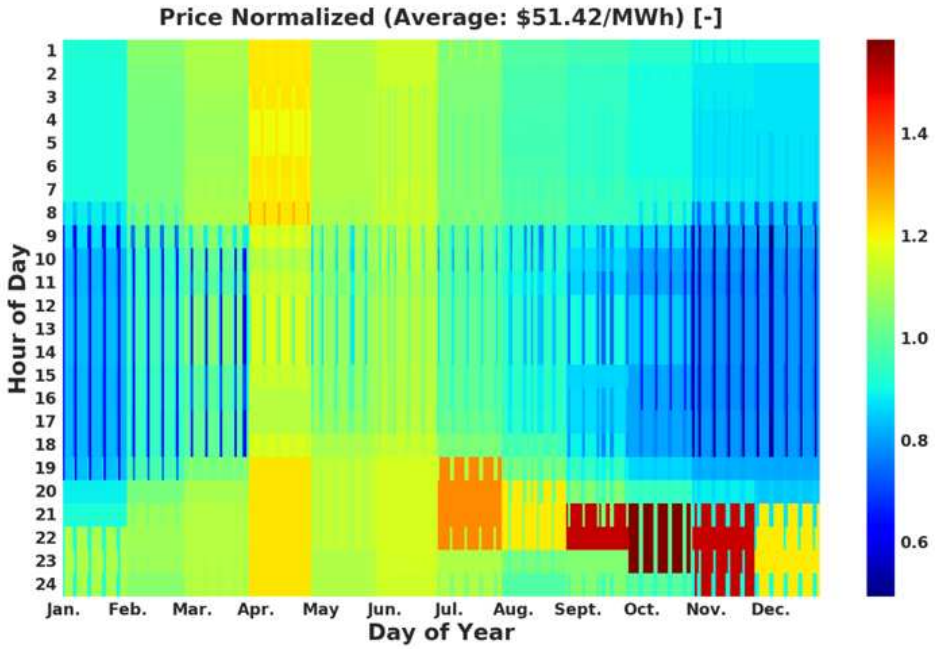

(a) NC spot market normalized to an average electricity price of $51.42 per MWh.

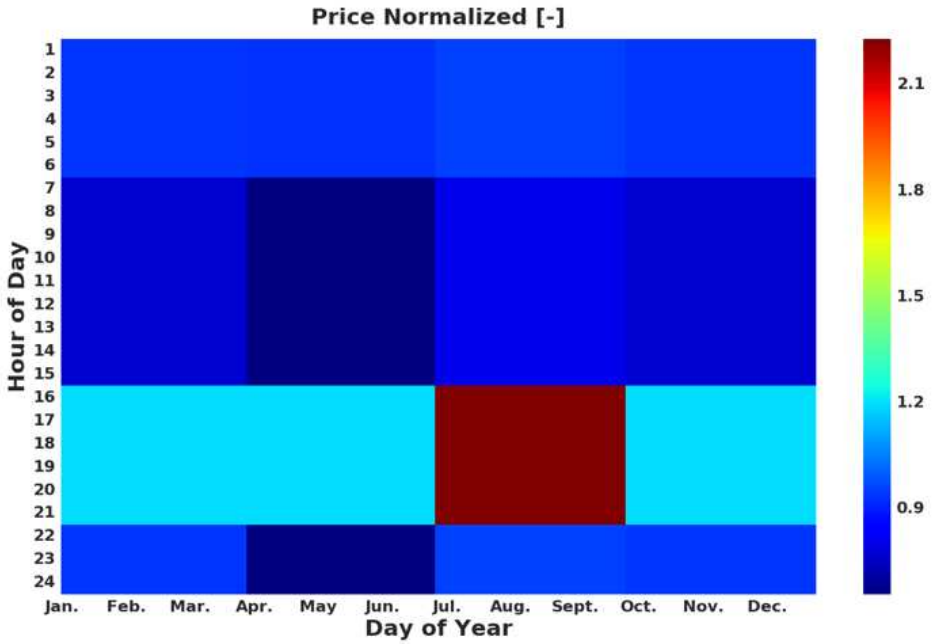

(b) PG&E market normalized by the power purchase agreement.

Figure 2.9: Time-of-use variation of electricity prices for the Northern Chile spot (NC spot) and Pacific Gas & Electric (PG&E) market.

limit each instance ($\mathcal{H}$) to 8 threads on the computing system to allow the four cases to be run in parallel, solving either to a relative optimality gap of 1×10^{-3} or to a specified time limit, whichever occurs first.

To get a sense of the computational difficulty, we solve each location-market combination using the hybrid dispatch model ($\mathcal{H}$) without applying any of the solution techniques described above and with a solve time limit of 120 seconds. Figure 2.10(a) shows the distributions of solution times for the 365 instances of ($\mathcal{H}$) for each location-market combination in the numerical experiment.

From Figure 2.10(a), the S. Nevada location results in about three times the number of ($\mathcal{H}$) solves that reach the time limit compared to the N. Chile location. With the exclusion of solves that reach the time limit, instances associated with the S. Nevada location solve faster, on average, than those associated with the N. Chile location. The annual solution times, i.e., solving all 365 instances of ($\mathcal{H}$), range from 4 to 8 hours, which is unacceptable for a single CSP-TES-PV-battery hybrid design evaluation. Furthermore, due to the large number of instances of ($\mathcal{H}$) that reach the time limit, the dispatch solution quality is poor. Specifically, for the instances that reach the time limit, the average MILP gap ranges from 2 to 4% depending on the location-market combination, resulting in sub-optimal dispatch and lost revenue.

To discern the relative improvements each of the solution techniques described in Section 2.5 affords, we solve ($\mathcal{H}$) with the problem-size reduction technique and note a 49% to 59% improvement in annual simulation solution time, relative to the original formulation; this corresponds to an average annual simulation time of 2.5 hours. The combination of problem-size reduction and the tighter LP relaxation results in annual simulation solution times between 36 and 43 minutes, corresponding to an average solution time improvement of about 70% relative to that associated with ($\mathcal{H}$) using only problem-size reduction. Finally, using $\hat{\mathbf{H}}$ combined with problem-size reduction and tighter formulation results in an average annual simulation time of about 34 minutes, yielding an 85% to 93% overall solution time

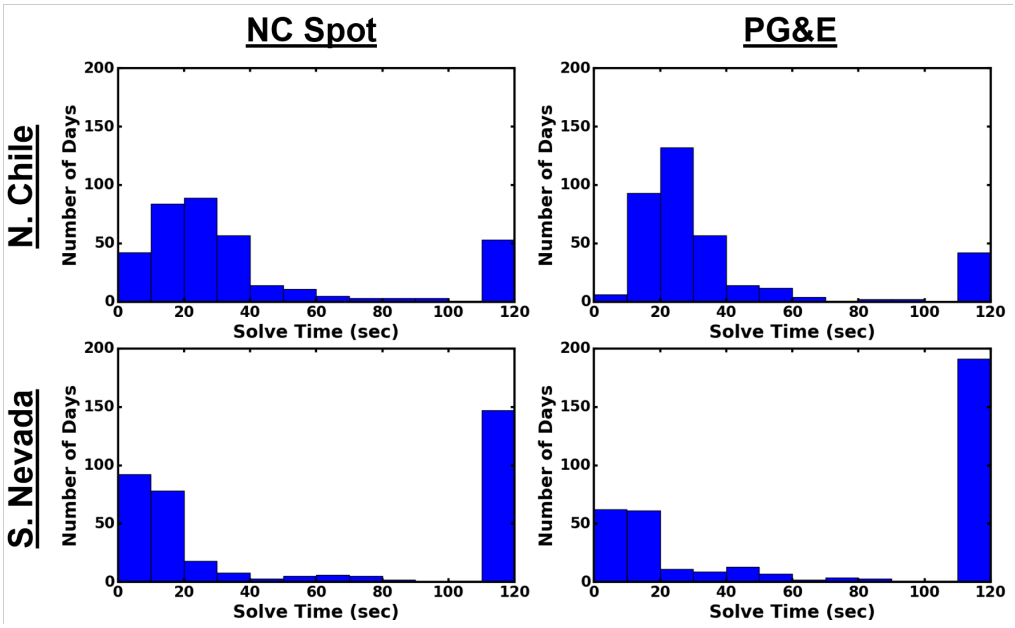

(a) Distribution of solution times from solving the 365 instances of ($\mathcal{H}$), without solution-expediting techniques, to the lesser of a relative optimality gap of 1×10^{-3} or a time limit of 120 seconds, for each location-market combination.

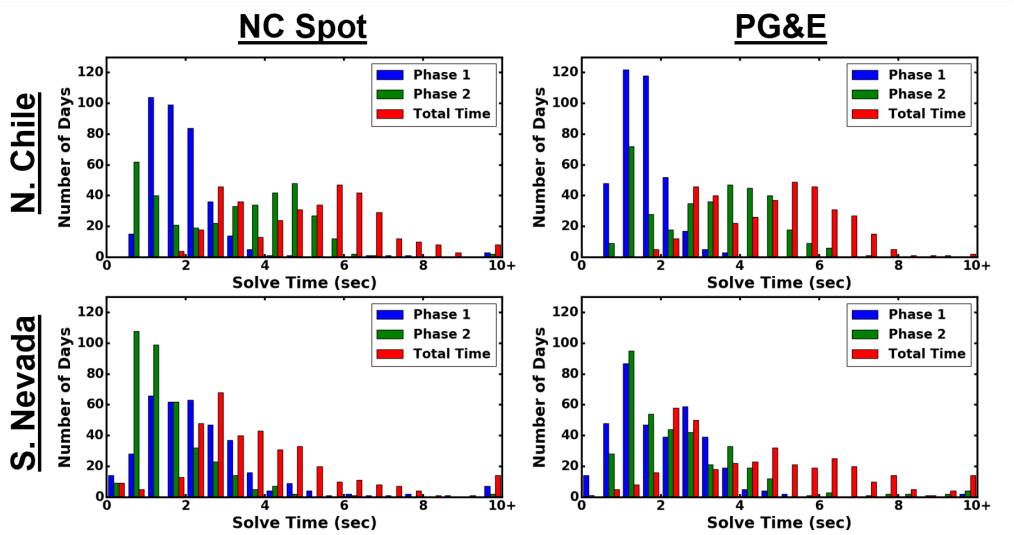

(b) Distribution of solution times from solving the 365 instances of $\hat{\mathbf{H}}$, with solution-expediting techniques, to the lesser of a relative optimality gap of 1×10^{-3} or a time limit of 60 seconds, for each location-market combination. Solve times greater than 10 seconds are reported in the last bin of the distribution. Solution times are categorized by $\hat{\mathbf{H}}$ Phase 1 (i.e., without battery operations), $\hat{\mathbf{H}}$ Phase 2 (i.e., cycle standby operations fixed and battery operations enabled), and total solve time for a given day.

Figure 2.10: Distribution of dispatch solution times from solving the 365 instances of ($\mathcal{H}$) and $\hat{\mathbf{H}}$ for each location-market combination of the numerical experiment.

reduction.

Figure 2.10(b) shows the distribution of daily dispatch solution times using the heuristic approach, $\hat{\mathbf{H}}$, and the other solution techniques described in Section 2.5. The distributions differentiate between the first and second phases of $\hat{\mathbf{H}}$ and the total solution time (i.e., the sum of the two solves). Each execution of $\hat{\mathbf{H}}$ is limited to 60 seconds. Solution times greater than 10 seconds are reported in the last bin of the distribution. Of the reported $\hat{\mathbf{H}}$ solution times, one problem instance, corresponding to the first-phase solve of $\hat{\mathbf{H}}$, reaches the time limit.

For the N. Chile location, on average, the first phase solves faster than the second phase (Figure 2.10(b)). However, this differentiation disappears for the S. Nevada location, owing to the grid constraint being tight in more of the N. Chile instances, resulting in more difficulty scheduling the battery operations. In general, the S. Nevada instances' total solve time is less than that of the N. Chile instances. However, the majority of total dispatch solution times, for all location-market combinations, is below 8 seconds.

2.6.3.1 Validation of the Heuristic Solution Approach

To validate $\hat{\mathbf{H}}$, we solve each dispatch problem with $\hat{\mathbf{H}}$ and ($\mathcal{H}$) directly, both with the other solution techniques applied, and compare corresponding objective function values. We use the heuristic solution from $\hat{\mathbf{H}}$ as an initial feasible solution to ($\mathcal{H}$) and impose no time limit on this problem. We observe the greatest difference between the objective function values of $\hat{\mathbf{H}}$ and ($\mathcal{H}$) to be \$8,935 for a two-day horizon, corresponding to a relative gap between $\hat{\mathbf{H}}$ and ($\mathcal{H}$) of about 0.83%. The difference between objectives averages less than \$120 in revenue for a two-day horizon over all 4 combinations of the 365 48-hour instances.

2.6.3.2 Annual Plant Performance

Annual simulation of CSP-TES-PV-battery hybrid plants allows us to understand the performance of a particular system design in a given location and under certain market conditions. Figure 2.11 plots six annual simulation responses for the numerical experiment.

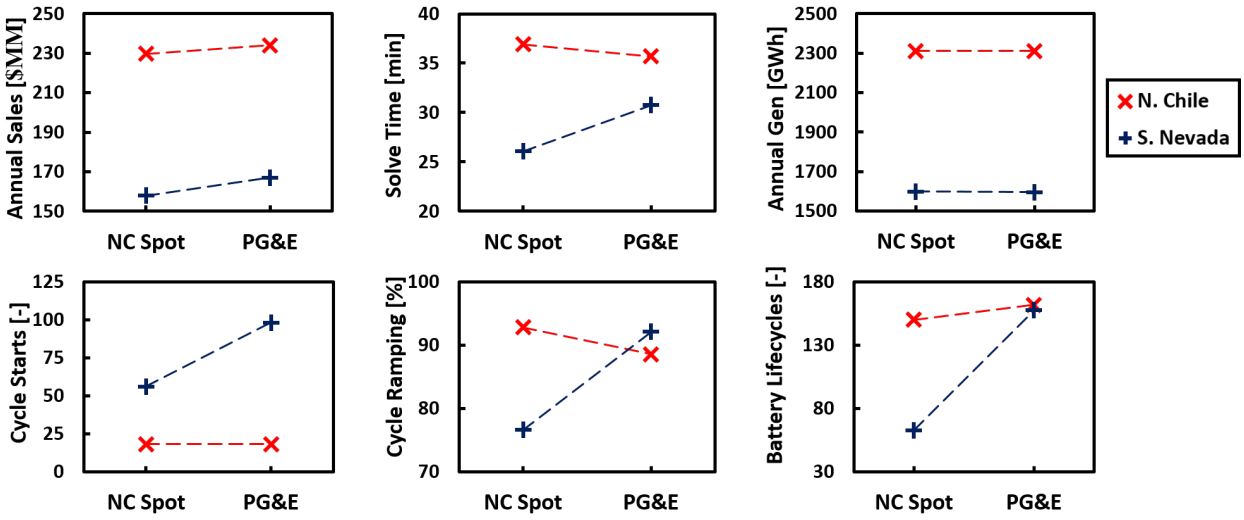

Figure 2.11: Annual solution responses from the numerical experiment: annual sales, solve time, annual generation, cycle starts, cycle ramping, and battery lifecycles.

We calculate **annual sales** as the sum, over all time periods within a year, of the product of energy generation, the normalized price multiplier, and an assumed PPA price of \$0.1/kWh. This response plot shows that the PG&E market results in greater sales than the NC spot market owing to the higher price multiplier during high-price time periods in the former market relative to those for to the latter market. However, the PG&E market has a greater effect on this plant design in S. Nevada than in N. Chile, owing to the lower solar resource in S. Nevada, illustrating the importance of dispatch optimization as solar resource decreases in a market structure similar to PG&E's.

Figure 2.11 depicts annual **solve time** and **generation** responses; the former shows that N. Chile annual dispatch strategies require more computational time, consistent with the results reported above. Annual generation shows that there is little-to-no interaction between generation and *market* factor because the price at which electricity is sold should not have a significant impact on how much electricity the plant can generate throughout the year. However, the annual generation plot shows the impact of the *location* factor in this study. Due to the greater solar resource in N. Chile, this plant design produces about 700 GWh more electricity in N. Chile than in S. Nevada.

The responses **cycle starts** and **cycle ramping** demonstrate how the power cycles would be operated. Due to the abundant solar resource, the hybrid plant power cycle in N. Chile would only need to start up about 20 times in a given year. However, the same plant in S. Nevada would need to start the power cycle 50 to 100 times annually, depending on the market, which could cause more wear and tear on the cycle, resulting in an increase in maintenance costs. Cycle ramping is the daily average percentage of the rated power the cycle ramps up and down, e.g., 100% represents the power cycle ramping from zero to rated power and back down to zero every day. Interestingly, the PG&E market requires more cycle ramping than the NC spot market for the S. Nevada location, but less for the N. Chile location. In the lower solar resource location of S. Nevada, cycle start-up and ramping become more important to ensure electricity generation occurs during high-revenue times of the PG&E market.

The last response plotted is **battery lifecycles**, which determines if the battery must be replaced during the 25- to 30-year life of this project. The life of a lithium-ion battery ranges from 500 to 4,000 cycles depending on the depth of discharge [62]. Discharging more of a battery's capacity at higher rates of power results in reduced expected lifecycle of the battery. Battery lifecycles are calculated based on the current throughput to-and-from the battery, i_t^- and i_t^+, using the following equation:

$$b^c = \sum_{t=1}^{\mathcal{T}} \frac{\Delta(i_t^- + i_t^+)}{2 \cdot C^B}$$

where C^B is the capacity of the battery. Of the four cases, the S. Nevada within the NC spot market possesses the lowest number of battery lifecycles owing to the relatively flat price structure in the NC spot market and less abundant solar resource in S. Nevada. Therefore, battery storage operations become less desirable in this location-market combination. In N. Chile, battery storage captures excess solar energy that would otherwise be curtailed and discharged during high-price and/or less-solar-abundant periods. However, the hybrid system could be redesigned to include little-to-no solar curtailment. These design trade-offs

are outside the scope of this paper.

2.6.3.3 Comparison to a CSP-only System

To demonstrate the value of a hybrid system, we compare performance metrics for both a CSP-PV and a CSP-PV-battery hybrid system to a stand-alone CSP system for the four location-market cases. These hybrid systems possess the design parameters given in the previous numerical experiments and are consistent with those produced by SAM and the corresponding dispatch optimization model ($\mathcal{H}$). Table 2.7 provides metrics, i.e., capacity factor (CF), levelized cost of energy (LCOE), and power purchase agreement (PPA), normalized by the corresponding metric for a CSP-only system, where CF is defined as the quotient of annual energy generation and the maximum annual grid transmission, LCOE corresponds to the quotient of lifetime costs and electrical energy production, and PPA represents the minimum price to which a power producer can agree in order to meet a project's desired internal rate of return [30]. We use SAM default system costs for financial calculations, and assume that installed battery cost is \$500/kWh$_e$ with a lifespan of 2,500 cycles and a replacement cost of \$250/kWh$_e$.

Table 2.7 shows that both the CSP-PV-battery system and the corresponding system without battery storage results in a significant increase in CF for all location-market combinations we test; conversely, the value of LCOE for both types of hybrid systems and all location-market combinations is about three-quarters of that for the CSP-only system, and the corresponding PPA values are about 80-90%. These comparisons indicate that hybrid systems possess increased dispatchability at more competitive prices than their CSP-only counterparts; furthermore, while the addition of a battery increases the capacity factor slightly, it does so at the expense of the economic metrics. Overall, the battery is relatively insignificant in improving these metrics owing to its cost relative to that of the thermal energy storage with which the CSP is coupled.

Table 2.7: Metrics for alternative power generation systems normalized by the corresponding metric for a CSP-only system. [capacity factor (CF), levelized cost of electricity (LCOE), and power purchase agreement (PPA)]

Location	Market	Metric	CSP-PV-Battery	CSP-PV
N. Chile	**NC Spot**	*CF*	165.8%	164.9%
		LCOE	78.7%	74.8%
		PPA	83.2%	79.1%
	PG&E	*CF*	165.5%	164.6%
		LCOE	78.7%	74.9%
		PPA	89.8%	85.3%
S. Nevada	**NC Spot**	*CF*	183.0%	182.9%
		LCOE	70.2%	68.0%
		PPA	75.7%	73.3%
	PG&E	*CF*	183.8%	183.9%
		LCOE	71.2%	67.3%
		PPA	86.0%	81.6%

2.7 Conclusions and Future Work

To analyze a CSP-TES-PV-battery hybrid system, we develop a dispatch optimization model ($\mathcal{H}$) to schedule, at sub-hourly time fidelity, the different technologies for energy generation within a detailed simulation framework (SAM's simulation core). The original formulation, ($\mathcal{H}$), proves to be too computationally expensive for timely hybrid design evaluation. Therefore, we implement solution techniques to reduce solution times, resulting in annual instances (consisting of 365 48-hour solves over progressive 24-hour horizons) being executed in about 34 minutes, an 86% to 93% improvement compared to the solve times without the solution-time improvements. With manageable solution times, we are able to exercise the CSP-TES-PV-battery hybrid simulation tool with dispatch optimization using a two-factor, two-level numerical experiment based on plant location and pricing market. We compare solution times and present annual plant performance metrics for each of these cases. Also, we compare alternative hybrid systems to the CSP-only systems based on capacity factor, levelized cost of energy, and power purchase agreement. This analysis shows that

hybrid systems dramatically outperform their CSP-only counterparts both from a capacity factor perspective and also economically.

An extension of this work uses our model ($\mathcal{H}$) to inform the design of a hybrid system. At the opposite end of the planning spectrum, future research efforts might shorten the time fidelity of the model to five minutes to make dispatch decisions in the real-time electricity market using weather uncertainty, improving the return-on-investment for solar hybrid generation facilities and making them more competitive with conventional energy generation plants.

CHAPTER 3

OFF-DESIGN PERFORMANCE OF MOLTEN SALT-DRIVEN RANKINE CYCLES AND ITS IMPACT ON THE OPTIMAL DISPATCH OF CONCENTRATING SOLAR POWER SYSTEMS

This paper is prepared for the journal *Energy Conversion and Management*

William T. Hamilton[7,8], Alexandra M. Newman[7,9], Michael J. Wagner[10], and Robert J. Braun[7,9,11]

3.1 Abstract

Due to the finite nature of daily solar energy collection and storage, concentrated solar power (CSP) power cycle operational decisions are critical to the economics of the system. For example, as thermal energy storage depletes during evening hours, the decision to operate at a low power output through the night or to shut down the plant and restart the next day yields trade-offs that are not well understood.

In order to properly understand the effects of part-load operation on optimal dispatch protocols, it is necessary to model the CSP power cycle at a fidelity that enables off-design performance characteristics to be properly captured. Towards that end, we develop a molten salt-driven Rankine power cycle model using Engineering Equation Solver software [63]. With equations and correlations from literature, our model predicts cycle off-design performance for various boundary conditions, i.e., molten salt inlet temperature, mass flow rate, and ambient temperature. We validate our results using cycle performance data provided by an industry partner and against another model within literature. To model the complete

[7]Department of Mechanical Engineering, Colorado School of Mines, Golden, CO 80401
[8]Ph.D. Student
[9]Professor of Mechanical Engineering
[10]Mechanical Engineer, Ph.D., National Renewable Energy Laboratory, Golden, CO 80401
[11]Corresponding Author

CSP system, i.e., solar field and receiver, we implement our Rankine cycle off-design performance results into the National Renewable Energy Laboratory's (NREL's) System Advisor Model (SAM) software. From previous work, SAM uses dispatch optimization to make operational decisions that maximize system profits. We present our Rankine cycle modeling approach, validate our model's results against industry data and a model from literature, and compare the resulting off-design performance to that of SAM's default power cycle model. Results indicate SAM's power cycle off-design performance either under or over predicts efficiencies depending on the control method chosen by the user. A case study demonstrates the impact of cycle off-design performance on annual performance for a stand-alone CSP system and a CSP-PV hybrid system. In addition, we demonstrate how cycle off-design performance influences optimal operator dispatch decisions and, thereby, overall system design and economics. Development of an off-design Rankine cycle model is not novel; however, investigating the impact of cycle off-design performance on system dispatch, economics, and design is a literature contribution.

3.2 Background

Concentrating solar power (CSP) with thermal energy storage (TES), utilizes the solar thermal spectrum to generate, store, and dispatch heat to create on-demand electricity. Specifically, CSP power tower technology consists of a field of heliostats that reflect solar photons to a central receiver where the radiation intensity can be greater than 1,000 suns. Within the receiver, a heat transfer medium is used to collect the focused thermal energy and either store it or use it to produce electricity in a thermodynamic cycle. Current utility-scale power tower systems utilize liquid molten salt (60% $NaNO_3$ 40% KNO_3), operating between 290°C and 565°C, to capture thermal energy from the sun within the receiver. After passing through the receiver, the heated molten salt can either be immediately used to generate electricity via Rankine power cycle, for example, or be stored in an insulated tank for use at a later time. When electricity generation is desired, high temperature molten salt flows through a series of heat exchangers where water is heated to generate superheated steam

that once expanded in a steam turbine, produces shaft work that drives an electric generator.

Figure 3.1 depicts a schematic of a prototypical power cycle in a CSP plant that employs a subcritical reheat regenerative Rankine cycle with seven feedwater heaters and a molten salt-to-steam heat exchanger train. Superheated steam leaving the salt-to-steam train expands through a high-pressure turbine (HPT), is reheated, and expands through the intermediate pressure turbine (IPT) and low pressure turbine (LPT), after which it is condensed into feedwater, and is pumped back to the salt-to-steam train. To improve efficiency, a small amount of steam is extracted at discrete locations during the turbine expansion to pre-heat the feedwater before the molten salt heat input. The individual components that constitute a Rankine cycle are sized to result in the highest efficiency when operating at design conditions, i.e., design-point efficiency.

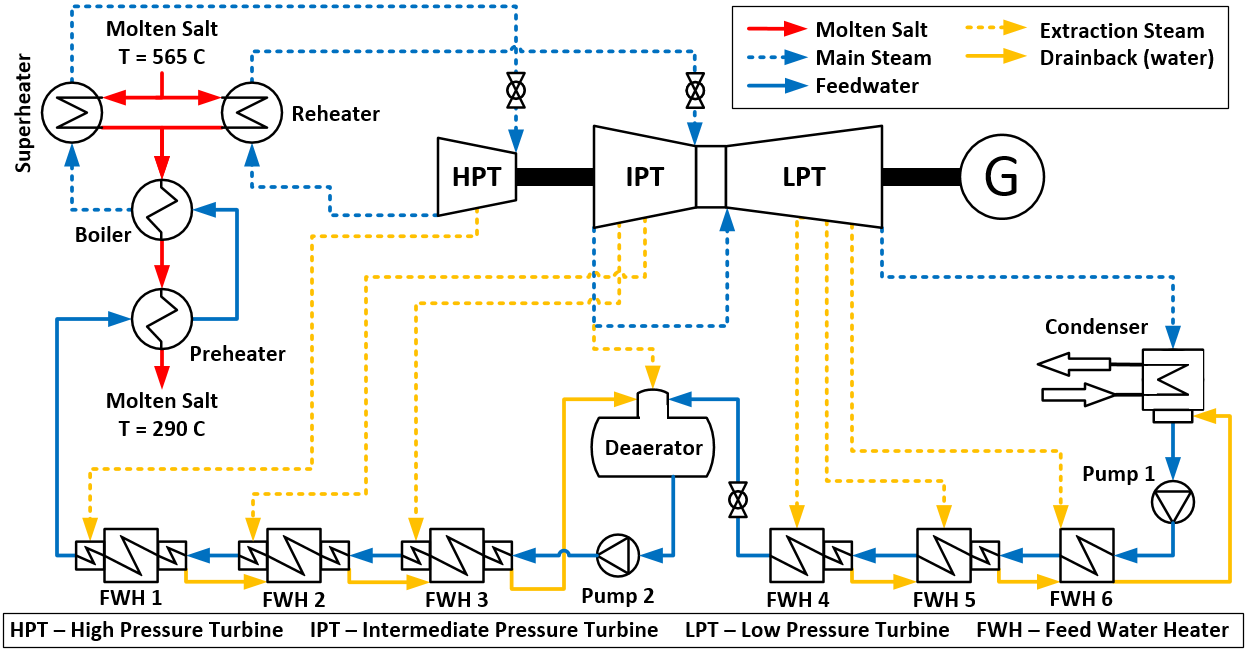

Figure 3.1: Molten salt-driven Rankine cycle with reheat, three turbine stages, and seven feedwater heaters, a sub-system in current commercial-scale CSP tower systems.

Balancing electricity supply to meet demand becomes an ever-increasing challenge as penetration levels of intermittent renewable energy, such as wind and solar, increase. To achieve high renewable energy grid-penetration requires either: (i) over-generation and, con-

sequently, curtailment, (ii) integration of highly flexible generators, or (iii) adoption of energy storage technologies [17]. The ability of a renewable technology to be dispatched flexibly, e.g., by combining CSP with TES, enables greater market penetration compared to variable generation sources without storage mechanisms. However, generation dispatchability and flexibility requires the Rankine cycle to operate in "off-design" conditions, frequently resulting in lower efficiency.

3.2.1 Rankine cycle part-load operation

In molten salt-driven Rankine cycles, electric power output is controllably reduced by decreasing salt flow rate, reducing cycle heat input, and, thereby, reducing steam generation within the salt-to-steam heat exchanger train. When steam mass flow rate is reduced, the turbine inlet pressure decreases under fixed speed conditions (resulting in a reduction of achievable enthalpy drop in the steam turbines). To achieve the lower turbine inlet pressure, the cycle's pumps can either produce feedwater at the design pressure with the introduction of throttling, or they can produce feedwater at the reduced pressure. These two methods are referred to as constant and sliding pressure operations, respectively.

The advantage of the constant pressure operation is that the boiler does not experience pressure changes during part-load operation, which can reduce transient stresses during load changes; however, work is lost due the throttling process in the turbine control valves. Under sliding pressure operation, boiler pressure varies depending on cycle load; consequently, turbine control valves remain fully open, regardless of part-load operation, which mitigates irreversibilities from throttling. As the cycle power is reduced from design to part-load operations, the pressure rise requirements for the feedwater pumps are reduced and, consequently, pump work is decreased. Due to the reduced pump work and valve throttling, sliding pressure operation typically results in higher cycle thermal efficiencies at part-load than the constant pressure operation. The main disadvantage of sliding pressure is a longer response time to load changes because the transients associated with boiler pressure are slower than the actuation of the control valves [64].

3.2.2 Related work

Rankine cycle off-design performance is well understood due to the maturity of the technology. The overall cycle performance is primarily a function of classification, i.e., subcritical, supercritical, reheat, or regenerative, and individual component performance. One of the largest uncertainties in predicting the part-load performance of steam turbines is properly evaluating the change in isentropic efficiency of the device. The standard methodology to model steam turbine off-design performance, in the absence of specific manufacturer test data, is the Spencer-Cotton-Cannon (SCC) method (1963) [65]. The SCC method is considered to be a conservative approach with actual turbine performance being approximately 2% higher than calculated values [64].

The SCC method, in combination with Stodola's ellipse method [66, 67], has been used to model steam turbine performance with limited knowledge about the turbine design specifics. The following work also uses this method: Woudstra et al. analyze the thermodynamic performance of a combined cycle utilizing Cycle-Temp, a power cycle modeling computer program which evaluates steam turbine performance [68]. Chacartegui et al. model and validate the performance of a 565 MW fossil fuel steam power plant to predict off-design performance of large steam turbines [69]. For CSP applications, Marugán-Cruz et al. conduct a parametric analysis of direct steam generation linear Fresnel CSP plant. The authors implement turbine sliding pressure control and off-design cycle performance [70]. McTigue et al. model a double-flash geothermal power plant hybridized with a CSP field, through the use of IPSEpro, and Stodola's ellipse to capture off-design behavior of the steam turbines [71]. Brodrick et al. use operational optimization to analyze an integrated solar combined cycle [72], and evaluate efficiency corrections for the steam turbine during part-load operations. Brodrick investigates the impact of system operations and feasibility by implementing nonlinear optimization to determine operating parameters for varying solar resource and electricity pricing. Based on literature acceptance, we implement the SCC and Stodola's ellipse methods to model off-design turbine performance.

Researchers have developed models to determine optimal scheduling of system operations with and without off-design performance. Castronuovo and Lopes propose a hourly-discretized optimization model to determine the optimum daily operational decisions for a wind farm with pumped hydro storage [73]. However, no off-design performance is considered within the optimization model. Bischi et al. develop a mixed-integer linear program to make short-term decisions for the operations of a combined cooling, heat and power energy system [74]. The authors convert nonlinear off-design performance curves to piece-wise linear approximations and compare solution quality for varying piece-wise intervals. However, this lacks a comparison between operational decisions using different performance curves. Zhou et al. investigate the impacts of component off-design performance on the optimal design of combined cooling, heating, and power systems [75]. The authors develop two optimization models that determine the design and operation of a combined cooling, heating, and power system: (i) assuming constant efficiency and (ii) considering equipment off-design performance. Their results indicate, for the given case study, that assuming constant efficiency provides a solution within 5% of the model considering equipment off-design performance. However, the system design is composed of discrete decisions on the number of a single type of equipment to acquire which limits the design space.

The contribution of our work comes from investigating and understanding Rankine cycle off-design performance impact on dispatch optimization decisions and the propagation of those decisions into the system's design, annual performance, and economics.

3.2.3 Objectives of our work

We develop and validate a Rankine cycle model with which to evaluate off-design performance, implement off-design performance into existing simulation software, and compare results against those from previous models. In Section 3.3, we describe the National Renewable Energy Laboratory's (NREL's) System Advisor Model (SAM) and the development of our Rankine cycle off-design performance model within Engineering Equation Solver. In addition, Section 3.3 includes validation of our Rankine cycle model against industry data and

another model presented in literature. Section 3.4 describes the integration of our validated performance Rankine cycle model into SAM, a short description of our dispatch optimization methodology, and outlines a case study, which examines the impact of cycle off-design performance on optimal dispatch and its influence on system design, performance, and economics. Section 3.5 presents a comparison between our Rankine cycle model's off-design performance and SAM's default cycle. In addition, Section 3.5 discusses the impact of cycle off-design performance has on optimal operations, annual metrics, and implications on design. Section 3.6 concludes this paper with a summary of our findings.

3.3 Rankine Cycle Off-design Performance Models

One standard approach for evaluating the performance of thermal-energy-to-electricity conversion of a power tower CSP system utilizes SAM's Rankine cycle model, which we term (R) [76], and employs user-defined, high-level parameters and predefined look-up tables to model off-design cycle performance efficiently (described in greater detail later). (R) achieves a significant improvement over previous methods by (i) allowing SAM users to quickly evaluate power tower CSP system designs utilizing a Rankine cycle for thermal-energy-to-electric conversion, (ii) providing users convenient options for modeling different turbine inlet pressure control methods and condenser types, and (iii) enabling complex system control that can utilize dispatch optimization to maximize system revenue over an immediate time horizon [11].

SAM's Rankine performance model (R) employs a minimal set of user-defined cycle parameters to predict off-design cycle performance for an annual simulation, which includes options for turbine inlet pressure control, i.e., fixed or sliding, and cycle condenser types, i.e., evaporative, air-cooled, and hybrid. (R) utilizes a multiple-variable regression method to predict the cycle's electrical output for a given molten salt inlet temperature, molten salt mass flow rate, and condenser pressure. Molten salt inlet temperature and mass flow rate impact available heat to the cycle, while condenser pressure affects the available energy in the low-pressure turbine's last stage.

(R) estimates Rankine cycle performance given a cycle configuration and ambient conditions, but may be improved in several respects. Specifically, the relationship between heat input and electrical power output, which can overestimate cycle efficiency at part-load conditions (shown in Section 3.5.1). In commonly simulated plant configurations, the power often operates at or near the design heat input. However, cycle partial-load conditions occur more frequently when SAM is employed in conjunction with the dispatch optimization model [20], which can incorporate hybridization of CSP systems with photovoltaics [18].

3.3.1 Rankine Cycle Model Development

We develop a Rankine cycle model capable of off-design performance calculations using Engineering Equation Solver (EES) [63], to which we refer as (E). Figure 3.1 depicts the modeled system, which contains steam reheat after expansion through the HPT and turbine extraction steam to six closed and one open feed water heaters. In order to model the entry cycle at a fidelity capable of capturing off-design performance, each component design characteristic must be gathered either through literature, industry knowledge, or a design-point heat balance. To develop (E), we use a heat balance of a Rankine cycle rated at 120MW$_e$ gross output, provided by our industry partners. The heat balance contains pressures, temperatures, and mass flow rates before and after each component within the cycle at 100% load condition and design ambient conditions.

3.3.1.1 Steam Turbines

Steam turbines have a significant effect on cycle performance because their efficiencies dictate the mechanical energy that can be converted from the steam's available energy (or exergy). The SCC method specifies baseline efficiencies for various turbine sections and correction functions to account for volumetric flow rate, governing stage design, pressure ratio, initial conditions, partial load, and an optional mean-of-loops (a heat rate curve as a weighted average of the cycle performance over control valve actuations) [65]. In addition, the SCC method provides procedures for calculating packing leakages and turbine-generator

losses associated with exhaust, mechanical, and generator.

For the development of (E), we model the HPT and the combined sections of the IPT and LPT using the SCC method described for a "3600-rpm noncondensing one-row governing stage" and a "3600-rpm condensing without governing stage," respectively. We estimate values for a majority of the independent variables, i.e., pressure ratios across stages, and steam flow rates at design, needed for the SCC method correction functions, using our industry partner's provided design-point heat balance. For the independent variables that cannot be estimated using the information provided by the industry heat balance, we assume values based on engineering approximations and literature [64]. We assume that the HPT governing stage has four control valves and a pitch diameter of 38 inches, a common configuration, along with an LPT last-stage annulus area of 55.6 square feet (afforded by a degree of freedom) because this area provided performance closest to our industry data when using the SCC-method tabulated values of exhaust losses.

For part-load conditions, the HPT efficiency is primarily a function of the ratio between inlet flow rate at part-load and the nominal design value. As this ratio decreases, the governing stage and overall HPT efficiencies decrease. On the other hand, the LPT efficiency is primarily a function of the annulus velocity of the last stage. We capture this effect using the SCC method through the calculation of exhaust losses, whose curves are a function of annulus velocity and are turbine-manufacturer-specific. However, the SCC method provides some representative relationships between annulus velocity and exhaust losses for various last-stage annulus areas.

During part-load conditions, extraction pressures, enthalpies, and mass flow rates vary as a function of throttle mass flow rate. To estimate extraction pressures and pressure after governing stage during part-load conditions, we implement Stodola's ellipse law [66], presented in Equation (3.1).

$$\frac{\dot{m}}{\dot{m}_{\mathrm{D}}}\frac{\sqrt{\rho_{i,\mathrm{D}}P_{i,\mathrm{D}}}}{\sqrt{\rho_i P_i}} = \frac{\sqrt{1-(P_o/P_i)^2}}{\sqrt{1-(P_{o,\mathrm{D}}/P_{i,\mathrm{D}})^2}}, \tag{3.1}$$

where $\dot{m}$ is the mass flow rate through the turbine stage, P is pressure, ρ is density, the subscript i refers to stage inlet, the subscript o refers to stage outlet, and the subscript D refers to the design condition.

Extraction enthalpies can be determined by the intersection of the turbine expansion line on an enthalpy-entropy (or Mollier) chart and the extraction pressure. For the HPT, expansion lines can be approximated as a straight line from the bowl condition to the turbine exit condition. Historically, IPT and LPT expansion lines were approximated using a Keuffel and Esser curve number 1864-31 [65]. We develop a second-order polynomial fit of entropy as a function enthalpy for the IPT and the LPT expansion line at design using the heat balance provided by our industry partners. For partial mass flow rates, expansion lines run parallel to the design lines, intersecting the calculated end point. This methodology is described in detail within the SCC method [65]. We estimate the turbine extraction mass flow by assuming a constant mass coefficient for all partial flow rates, shown in Equation (3.2).

$$\frac{\dot{m}_e}{\dot{m}_{e,\mathrm{D}}} = \frac{\sqrt{\rho_e P_e}}{\sqrt{\rho_{e,\mathrm{D}} P_{e,\mathrm{D}}}}, \tag{3.2}$$

where the subscript e refers to the conditions at turbine extraction.

3.3.1.2 Air-Cooled Condenser

Performance of the air- or water-cooled condenser dictates the relationship between condenser pressure, heat rejection, and ambient temperature. Condenser pressure affects the amount of available energy that the LPT can extract; therefore, condenser pressure as a function of heat rejection and ambient temperature is important to capture in off-design performance predictions. Air-cooled condenser performance is manufacturer-specific and can be challenging to generalize. Fortunately, our industry partner provided air-cooled condenser data, which includes condenser pressure as a function of heat rejection, and ambient temperature. Because of the proprietary nature of the data, we normalize it using minimum condenser pressure, design heat rejection, and design ambient temperature (converted to Kelvin), shown in Figure 3.2 and explicitly denoted by markers.

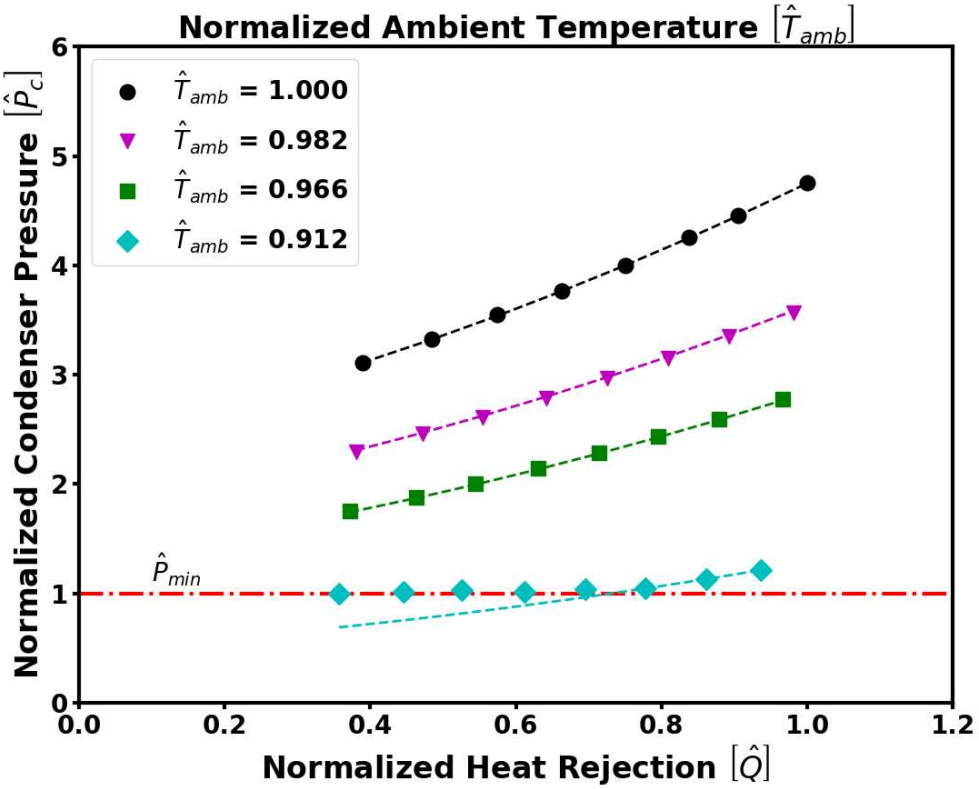

Figure 3.2: Normalized condenser pressure as a function of normalized heat rejection and normalized ambient temperature. Markers denote industry-provided data, while fitted function evaluated at the corresponding normalized ambient temperature and normalized heat rejection is represented by dashed lines of the same color.

From this data, we develop a second-order bi-variate polynomial in terms of normalized ambient temperature, $\hat{T}_{amb}$, and normalized heat rejection, $\hat{Q}$, to determine normalized condenser pressure, shown in Equation (3.3):

$$\tilde{P}_c\left(\hat{T}_{amb}, \hat{Q}\right) = \max\left\{\sum_{i=0}^{2}\sum_{j=0}^{2} a_{ij}\hat{T}_{amb}^{i}\hat{Q}^{j}, 1.0\right\}, \tag{3.3}$$

where $\tilde{P}_c$ is the normalized condenser pressure predicted by the bi-variate polynomial and a_{ij} is the coefficient for the (i, j) exponent pair. Table 3.1 contains the fitted regression model coefficients for the corresponding (i, j) exponent pairs.

When the bi-variate model predicts a normalized condenser pressure less then 1.0, e.g., when $\hat{T}_{amb} = 0.912$ and $\hat{Q} \leq 0.7$ in Figure 3.2, the predicted value is set to 1.0 by the

Table 3.1: Fitted regression model coefficients for the corresponding (i, j) exponent pairs.

a_{ij}		j		
		0	1	2
i	0	147.966	71.235	27.554
	1	-329.022	-159.268	-62.249
	2	183.460	89.502	35.571

maximum function. By setting the predicted value to 1.0, condenser pressure is set to the minimum pressure for the condenser. With respect to the industry-provided data, our bi-variate polynomial has a root mean squared error of 0.0126, a mean absolute error of 0.010, an R-squared value of 99.986%, and an adjusted R-squared value of 99.982%. Due to the quality of our bi-variate model, we implement said model into (E) to provide the relationship between ambient temperature, heat rejection, and condenser pressure.

For condenser parasitic fan power, we assume a constant approach temperature of 1.5°C and calculate the required air mass flow rate to achieve the desired heat rejection. Next, we assume constant fan isotropic and mechanical efficiencies of 85% and 97%, respectively. From these assumptions, fan power can be approximated using simple thermodynamic relationships.

3.3.1.3 Feedwater Heaters and Pumps

To model the six closed feedwater heaters (shown in Figure 3.1), we assume that the design drain cooler temperature difference remains constant during off-design operation and neglect any heat losses to the surroundings. With these assumptions, the outlet condition of the extraction drain is known and feedwater outlet temperature can be determined using an energy balance. Feedwater heater performance has a small impact on overall cycle efficiency; however, removing a feedwater heater from service can impact cycle efficiency greatly [64].

Pressure drop through feedwater heaters is handled by Equation (3.4) [77]:

$$\Delta P = k_p \dot{m}^2, \tag{3.4}$$

where ΔP is the difference between inlet and outlet pressures, k_p is a proportionality constant, and $\dot{m}$ is the mass flow rate through the heat exchanger. For off-design conditions, we assume that the heat exchanger pressure drop varies with the square of mass flow rate.

To model the feedwater and boiler re-circulation pumps, we assume a design isotropic efficiency of 80%. We adjust pump efficiency as a function of the ratio between part load and design mass flow rates using Equation (3.5) [77].

$$\frac{\eta_p}{\eta_{p,D}} = f + 2\,(1-f)\,\frac{\dot{m}}{\dot{m}_D} - (1-f)\left(\frac{\dot{m}}{\dot{m}_D}\right)^2, \tag{3.5}$$

where η_p is the pump isotropic efficiency, f is a shape factor parameter, $\dot{m}$ is the mass flow rate, and the subscript D refers to design conditions. For (E), we assume that the shape factor parameter f is equal to zero.

3.3.1.4 Molten Salt-to-Steam Heat Exchangers

From Figure 3.1, the molten salt-to-steam heat exchanger train is depicted in the upper left. Commercial-scale projects can have multiple trains in parallel to reduce the size of an individual heat exchanger. These heat exchangers are typically in the form of a counterflow shell-and-tube, utilizing different shell and tube configurations depending on the thermal and flow specifications. From the molten salt perspective, the salt enters the salt-to-steam train at about 565℃, a portion of the flow is directed to the reheater, while the rest enters the superheater. The flow ratio of this division is governed by the superheater's and reheater's thermal load and a equal target exit temperature to reduce mixing losses. After the superheater and reheater, the two molten salt flows merge and progress through the boiler and preheater, where the flow exits at a target temperature of 290℃.

To model the salt-to-steam heat exchanger train, we assume a constant molten salt outlet temperature of 290°C is maintained for all partial flow conditions. Heat loss to the surroundings is neglected for all heat exchangers in the salt-to-steam train. For the preheater, we assume saturated liquid as the feedwater outlet condition for all partial flow conditions. For the boiler, we assume saturated vapor at the feedwater outlet for all partial

flow conditions. Using energy balances for the preheater and boiler, we solve for the salt-to-steam train pinch temperature difference and steam mass flow rate given a molten salt flow rate.

For the superheater and reheater, we use the effectiveness-NTU method to predict working fluid outlet temperature [78]. We calculate an overall heat transfer coefficient using design inlet and outlet conditions. At design conditions, our target turbine inlet temperature is 540°C for both the HPT and the IPT sections. We determine 1345 kW/K and 804 kW/K as design-point heat transfer coefficients for the superheater and the reheater, respectively. We assume perfect control of molten salt flow fraction to the reheater in order to maintain equal molten salt superheater and reheater outlet temperatures.

For partial flow conditions, we adjust superheater and reheater overall heat transfer coefficients using Equation (3.6) [79].

$$\frac{\mathrm{UA}}{\mathrm{UA_D}} = \left(\frac{\dot{m}_h^{0.8}\dot{m}_c^{0.8}}{\dot{m}_{h,\mathrm{D}}^{0.8}\dot{m}_{c,\mathrm{D}}^{0.8}}\right)\left(\frac{\dot{m}_{h,\mathrm{D}}^{0.8}+\dot{m}_{c,\mathrm{D}}^{0.8}}{\dot{m}_h^{0.8}+\dot{m}_c^{0.8}}\right), \tag{3.6}$$

where UA is the overall heat transfer coefficient, $\dot{m}$ is mass flow rate, the subscripts h and c refer to the hot and cold side of the heat exchanger, respectively, and the subscript D refers to the nominal design value. We model pressure drop through the heat exchangers in the salt-to-steam train using Equation (3.4).

3.3.1.5 Sliding and Constant Pressure Operation

For both sliding and constant pressure operation, Equation (3.1) estimates "desired" steam pressure after the HPT governing stage, starting with the condenser pressure and working backwards through each turbine with respect to inlet pressure. For sliding pressure operation, boiler pressure is estimated using an assumed constant 4% pressure drop across the HPT stop and control valves and the pressure drop through the superheater. For constant pressure operation, the boiler remains at a pressure of 120 bar and the steam is throttled to the "desired" steam pressure at the HPT governing stage outlet. Henceforth, we denote off-design performance cycle models, i.e., (R) and (E) pertaining sliding and constant boiler

pressure operation, using superscripts s and c, respectively.

3.3.2 Validation and Error Analysis of model (E)

To validate (E), we compare relative heat rate (for sliding pressure operation) predicted by (E^s) against data provided by our industry partner for varying load fraction and normalized ambient temperature (see Figure 3.3). Relative heat rate is defined as the quotient of heat rate at an off-design condition and design heat rate; load faction is defined as the quotient of cycle output at an off-design condition and the design work output. In other words, a relative heat rate of 1.1 at a load fraction of 0.5 corresponds to the cycle requiring 10% more heat per unit of power compared to design point conditions, when producing 50% of design output. Relative heat rate can also be expressed in terms of the quotient of design-point and off-design efficiencies.

Figure 3.3 represents relative heat rate data (shown as symbols) provided by our industry partners; (E^s) predictions for relative heat rate are represented by lines of corresponding color. (E^s) adequately represents the data for the range of load faction and the various normalized ambient temperatures. (E^s) predicts the major trends contained within the data. As ambient temperature decreases, relative heat rate at full load conditions, i.e., $f_{pl} = 1$, decreases and the adverse effects at partial load fraction, represented by the derivative of the curve, decrease. However, (E^s) systematically underpredicts relative heat rate at partial load factions above 0.5 and overpredicts at low partial load fractions.

Figure 3.4 depicts the relative heat rate error, defined as (R^s) less (E^s), as a function of partial load faction for various normalized ambient temperatures. The largest error is -0.0212 and occurs at low normalized ambient temperature and low partial load fraction, i.e., $\hat{T}_{amb} = 0.912$ and $f_{pl} = 0.3$, which corresponds to a relative error of 2.08%. With respect to the provided industry data, (E^s) predicts relative heat rate with a root mean squared error of 8.59×10^{-3} and a mean absolute error of 7.30×10^{-3}. Due to small error between (E^s) and industry data, (E^s) appears to adequately represent off-design performance for a molten-salt driven Rankine cycle operating with sliding boiler pressure and using an air-cooled condenser

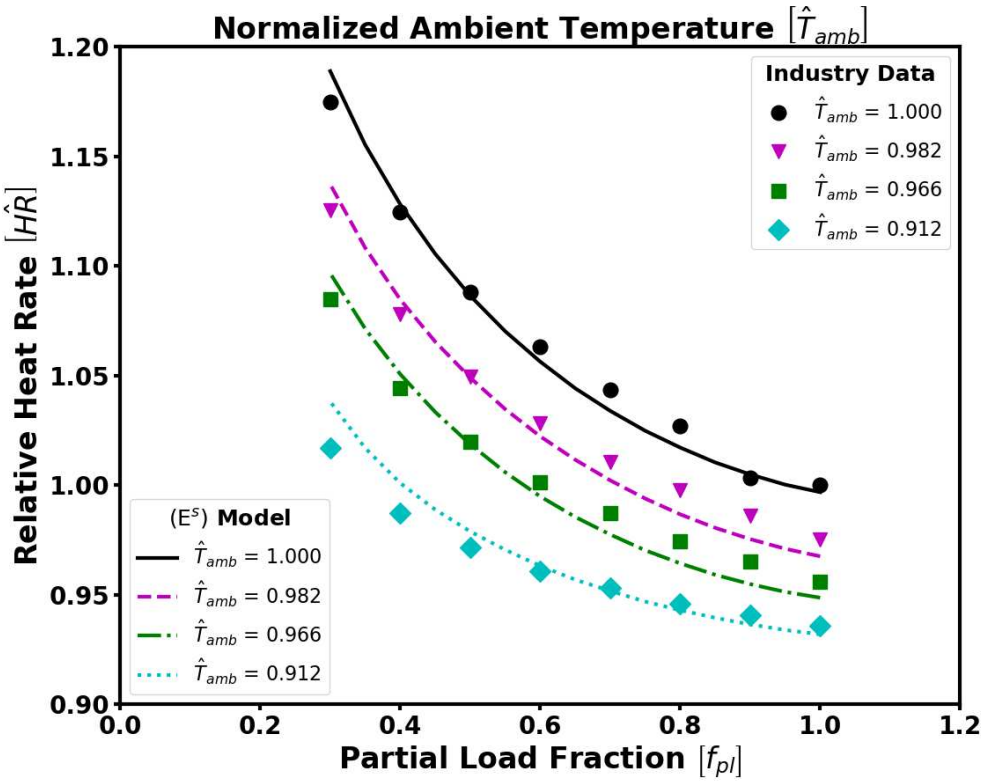

Figure 3.3: Relative heat rate (for sliding pressure operation) as a function of partial load faction and various normalized ambient temperatures. Industry data is represented by symbols and (E^s) model prediction is represented by lines of corresponding color.

for heat rejection.

We are unable to obtain cycle performance data for constant pressure operation from our industry partners. To validate (E^c)'s cycle performance predictions, we compare (E^c)'s relative heat rate curve to an open-source script that implements the SCC method in MATLAB® [80], shown in Figure 3.5. Utilizing the design heat balance, we provide Félix Pérez-Cicala's (2019) model with the appropriate assumptions previously outlined, e.g., turbine type as defined by the SCC method. To establish condenser pressure relationships, we provide Pérez-Cicala's model with (E^c)'s predictions of condenser saturation temperatures for design and minimum throttle flow conditions.

From Figure 3.5, (E^c)'s relative heat rate is in close agreement with Pérez-Cicala's model estimates. However, (E^c) deviates from Pérez-Cicala's model in a conservative manner at

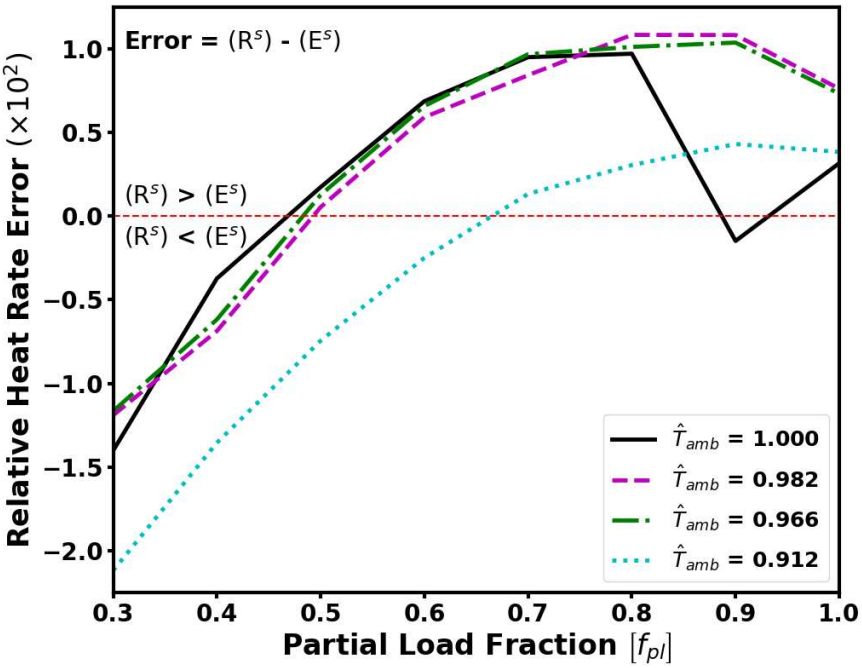

Figure 3.4: Relative heat rate error, defined as (R^s) less (E^s), as a function of partial load faction for various normalized ambient temperatures.

deceasing partial load factions. The two models remain within 1% of each other at lowest partial load fraction, i.e., 30% load. Based on this comparison, (E^c)'s estimate for relative heat rate closely matches Pérez-Cicala's model.

3.4 Integration of (E) into SAM and Case Study

To integrate (E)'s calculated cycle performance into SAM, we utilize the "User Defined Power Cycle" option. For user-defined cycles, SAM employs a design-of-experiments technique to capture the main and interaction effects of molten salt mass flow rate, molten salt temperature, and ambient temperature on cycle thermal input, cycle gross electrical output, electrical power consumption for cooling, and cooling water flow rate. Implementation of a user-defined cycle is described in detail within SAM's help documentation [81]. Table 3.2 presents low, design, and high parameter values used to generate (E)'s cycle performance maps for SAM. Additionally, we assume that (E)'s air-cooled condenser system consumes

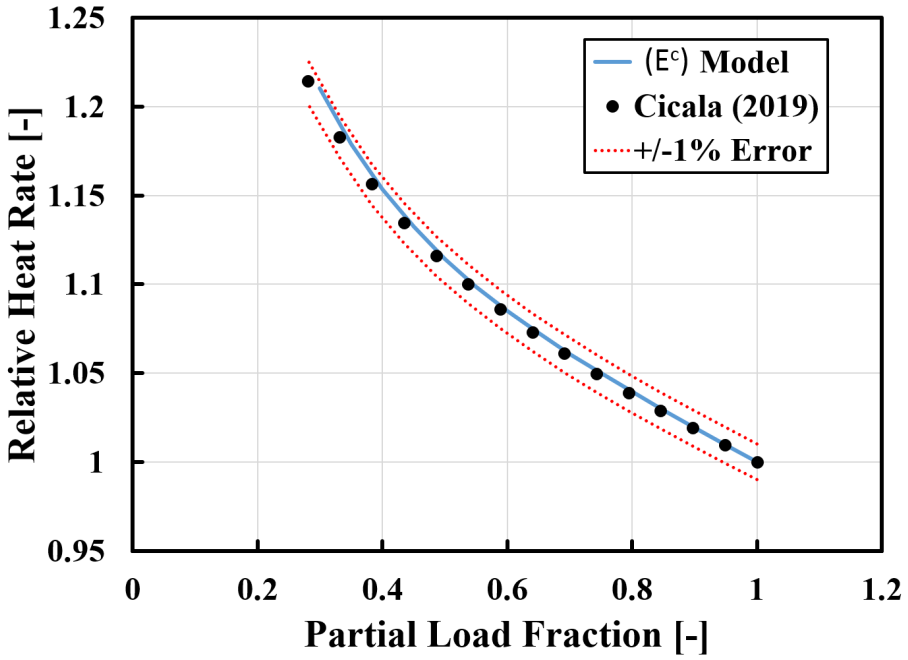

Figure 3.5: Comparison of (E^c) and Pérez-Cicala's model relative heat rates as a function of partial load faction for constant boiler pressure operation at design ambient temperature.

1.5% gross power at design conditions.

Table 3.2: Low, design, and high parameter values used to generate (E) cycle performance maps for SAM.

Parameter	Units	Low	Design	High
Molten salt temperature	°C	550	565	580
Normalized molten salt mass flow rate	-	0.30	1.00	1.05
Ambient Temperature	°C	15	43	55

3.4.1 Annual Simulations Utilizing Dispatch Optimization

To investigate the impact of off-design cycle performance on system economics, we utilize work that integrates SAM's simulation core with dispatch optimization. Our software framework, shown in Figure 3.6, enables us to utilize dispatch optimization to evaluate the performance and economics of CSP-only, CSP-PV (Photovoltaic) hybrids, and CSP-PV with battery storage designs. Our dispatch optimization model determines the operating schedule

of each sub-system in the design to maximize revenue over the time horizon. Our annual simulation and dispatch optimization is capable of evaluating system performance on hourly and sub-hourly time periods. For brevity, we refer the reader to our previous publications for a detailed description of the software framework and a complete formulation of the dispatch optimization model [18].

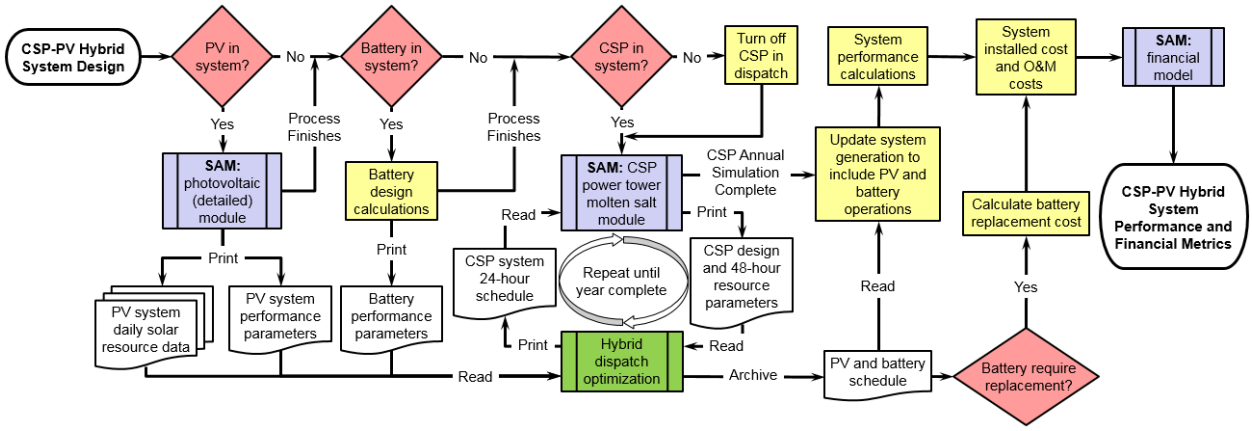

Figure 3.6: Flow diagram of the software architecture implemented around the hybrid dispatch optimization model.

3.4.2 Case Study

This case study examines the impact of cycle off-design performance on optimal dispatch and its influence on system design, performance, and economics. For our case study, we chose Rice, California, to which we refer hereafter as "Rice," as the plant's location and utilize typical meteorological year weather data for Rice at hourly time fidelity. The abandoned township of Rice has been explored as a potential location for a CSP system [20]. However, at the time of this writing, we are not aware of any active project development at Rice.

To be consistent with the geographic location of Rice, we choose the Southern California Edison 2015 pricing schedule as the electricity market against which to dispatch power. This electricity market has hourly prices differentiated by weekday, weekend, and season, with the highest-value time periods occurring between the hours of 2 and 8 p.m. on weekdays during the months of June through September.

For the system design, we assume a dry-cooled power cycle size of 163 MW_e gross output with a design ambient temperature of 43°C, a gross cycle efficiency of 41.2%, and the ability to operate between 30 and 105% of partial load fraction. To understand the impact of cycle performance on system design evaluation, we explore various designs using a uniform meshing of high-level system parameters, shown in Table 3.3. A uniform mesh of the system parameters in Table 3.3 results in 3,640 design cases, each of which were evaluated under the following assumptions: (i) the combined power output is grid-limited to 165 MW_e, (ii) the PV sub-system is single-axis tracking with zero tilt, and (iii) the system contains no electric battery storage. Given the solar resource at Rice and the solar multiple, SolarPILOT [58] generates the CSP heliostat field layout and receiver design parameters, such as tower height, receiver height and diameter.

Table 3.3: Low and high system design parameter values and the corresponding sampling interval used to generate a uniform mesh of system designs.

Design Parameter	**Units**	**Low**	**High**	**Interval**
Solar Multiple	-	0.50	3.50	0.25
Hours of Thermal Storage	Hours	4	16	2
PV Field Capacity	MW_{DC}	0	225	25
DC-to-AC ratio	MW_{DC}/MW_{AC}	1.0	1.3	0.1

In addition to off-design performance cycle models (R) and (E), we include a constant efficiency model to which we refer as (C). We assume that (C) operates at design-point efficiency for all combinations of partial loads and ambient temperature conditions. We compare (R)'s and (E)'s behavior to that of the baseline case with no cycle efficiency degradation, given by (C).

3.5 Results

The dispatch optimization model is written in the AMPL modeling language version 20210630 [56] and solved using CPLEX version 12.8 [57]. Hardware architecture to generate solutions consists of a SuperServer 1028GR-TR server with an Intel Xeon E5-2620 v4s at 2.1

GHz, running Ubuntu 16.04 with 128 GB of RAM, 1×250 GB SSD, and 3×500 GB SSDs hard dives.

3.5.1 Cycle Performance Comparison Between (R) and (E)

Figure 3.7 depicts a comparison of (R) and (E) relative heat rate curves as a function of partial load fraction, using sliding (Figure 3.7(a)) and constant (Figure 3.7(b)) boiler pressure operation for high-, design-, and low-ambient temperature conditions. Using SAM's look-up performance tables for sliding and constant pressure operation [82], we evaluate (R)'s relative heat rate relationships using design molten salt inlet temperature, values of normalized molten salt mass flow rates between 0.3 and 1.05, and constant condenser pressures of 0.2, 0.08, and 0.04 bar, corresponding to high-, design-, and low-ambient temperature conditions, respectively. We evaluate (E)'s relative heat rate relationships in a similar manner; however, constant ambient temperature is imposed instead of constant condenser pressure. We determine (E)'s cycle performance for normalized ambient temperatures of 1.04, 1.00, and 0.91, corresponding to high-, design-, and low- conditions, respectively.

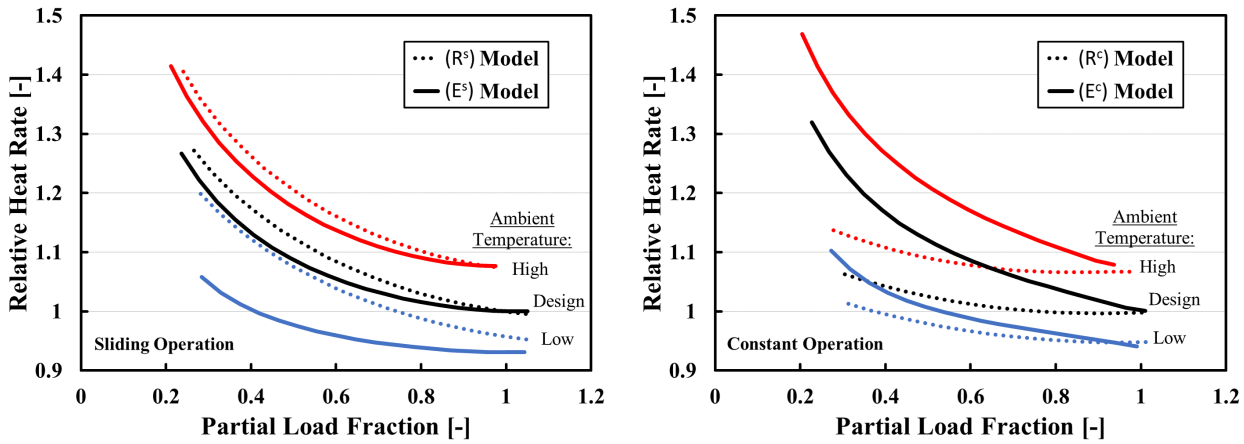

(a) Sliding boiler pressure operation.

(b) Constant boiler pressure operation.

Figure 3.7: Comparison of (R) and (E) relative heat rate curves as a function of partial load fraction, using (a) sliding, i.e., (R^s) and (E^s), and (b) constant, i.e., (R^c) and (E^c) boiler pressure operation for high-, design-, and low-ambient temperature conditions.

Figure 3.7(a) shows that (R^s) and (E^s) are in close agreement with each other in both magnitude and rate-of-change at high- and design-ambient temperature conditions. However, (R^s)'s and (E^s)'s estimated heat rates diverge for the low-ambient temperature condition which, at a partial load fraction of about 0.3, renders (R^s)'s relative heat rate 0.15 greater than (E^s). (R^s) provides a more conservative heat rate curve compared to (E^s). However, (E^s)'s heat rate at low-ambient temperature conditions yields a distinct advantage of higher efficiencies compared to (R^s).

Figure 3.7(b) shows that (R^c) and (E^c) are in agreement at full-load condition, i.e., partial load fraction equal to one. However, (R^c) and (E^c) diverge as partial load fraction is reduced. (R^c) estimates a better heat rate curve compared to (R^s). However, based on the reasons given in the descriptions of the two operating strategies in Section 3.2, sliding operation results in higher cycle efficiencies compared to constant operation. Therefore, (R^c) heat rate curve estimates are an optimistic and unrealistic representation of cycle performance at partial-load operations.

3.5.2 Impact on Annual Performance for CSP-only System

We first simulate annual performance for CSP-only system without hybridized photovoltaics using each of the five power cycle models previously discussed – (C), (R^s), (E^s), (R^c), and (E^c). The simulations consider all possible design configuration, and dispatch is optimized according to the characteristics of each cycle. Next, we choose the CSP-only design corresponding to the lowest power purchase agreement (PPA) price to determine the solar multiple and hours of TES, which are 2.5 and 10 hours, respectively.

Figure 3.8 depicts the annual percentage of time the power cycle spends in a thermal input range for a CSP-only system using the five off-design performance cycle models. The $[0, 30]$ range only contains values of 0 MW_t thermal input; therefore, the cycle is in an "off" state. From Figure 3.8, (R^s), (E^s), and (E^c) primarily operate at either a full-load or at an "off" state, which accounts for 40-45% and 25-30% of annual operation, respectively. (R^c) dispatches in a fashion similar to (C), i.e., spends more time in the low-power state $(90, 120]$

than in the "off" state. (C) and (R^c) spend only about 8% of the year in an "off" state, which is 3-4 times less than the other cycle models. The reverse is true for the low power state, in which (R^c) and (C) operate about three to six times more often in the low-power state compared to the other cycle models.

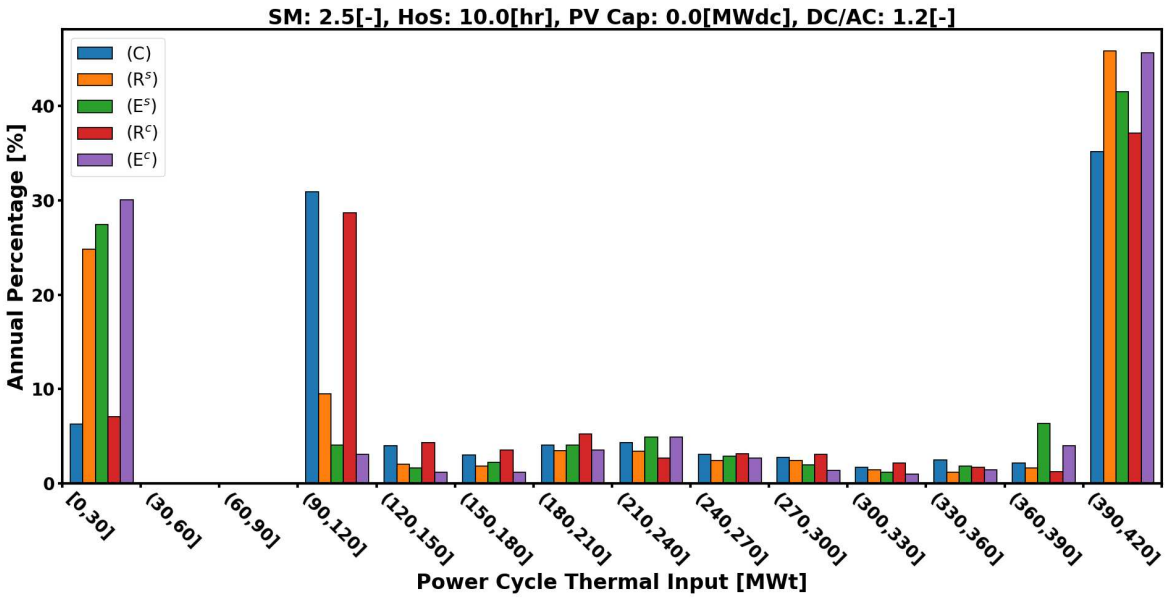

Figure 3.8: Annual percentage of time the power cycle spends in a thermal input range for a CSP-only system using the five off-design performance cycle models. The $[0, 30]$ range only contains values of 0 MW_t thermal input, corresponding to the cycle being in an "off" state.

Table 3.4 presents annual performance metrics for the five different off-design cycle models of the CSP-only system with a solar multiple of 2.5 and 10 hours of TES, and contains the following annual performance metrics: capacity factor, number of cycle starts, cycle ramp index, reliability (10%, 25%, and 50%), and simulation time. We also record "%Δ," which represents the percentage change between (E) and (R) utilizing the same boiler pressure operation, i.e., sliding or constant.

Capacity factor is the quotient of annual energy generation and the maximum possible energy generation, which is calculated using a grid transmission limit of 165 MW_e as the maximum system output. Due to a constant solar field design and solar resource, the five cases result in the same solar energy collection. Therefore, Table 3.4's capacity factor pro-

Table 3.4: Comparison between annual performance metrics using the various off-design cycle models for a CSP-only system comprise of a solar multiple of 2.5 and 10 hours of TES. Annual performance metrics shown are: capacity factor, number of cycle starts, cycle ramp index, reliability (10%, 25%, and 50%), and simulation time. We also record "%Δ," which represents the percentage change between (E) and (R) utilizing the same boiler pressure operation, i.e., sliding or constant.

Cycle Model	**Capacity Factor** [%]	**Cycle Starts** [-]	**Cycle Ramp** [%]	**Reliability**			**Simulation Time** [min.]
				10% [%]	**25%** [%]	**50%** [%]	
(C)	55.80	57	68.5	94.85	90.93	83.25	8.53
(R^s)	56.33	139	97.6	96.48	93.47	88.61	14.27
(E^s)	58.18	166	82.9	98.23	94.49	90.32	15.74
%Δ	+3.28	+19.42	-15.05	+1.81	+1.09	+1.94	+10.26
(R^c)	56.93	46	90.8	95.53	91.91	81.92	9.35
(E^c)	57.63	198	86.1	98.14	94.69	90.77	16.75
%Δ	+1.23	+330.43	-5.19	+2.74	+3.02	+10.80	+79.11

vides a direct comparison of solar-to-electric conversion. Table 3.4 shows that both (R) and (E) result in a higher capacity factor than (C) because (R) and (E) yield higher cycle efficiencies than does (C) at ambient temperatures below design conditions. For sliding pressure operation, (E^s) results in a higher capacity factor than (R^s) due to (E^s)'s performance at low-ambient temperature compared to that of (R^s), shown in Figure 3.7(a). For constant pressure operation, the difference between (R^c)'s and (E^c)'s capacity factor is smaller and is a result of (R^c)'s more frequent operation at low power output to avoid cycle start-ups, shown in Figure 3.8.

Cycle starts represents the number of start-up operations the power cycle undergoes throughout the year, regardless of whether the start up is "cold," "warm," or "hot" (where most of the cycle starts would be considered "hot" or "warm"). The *Cycle ramp index* corresponds to the average percentage of rated power ramp per day, e.g., 100% represents a cycle that goes from a no generation state, to full power, and back to no generation every day. For both sliding and constant operation, (E) results in more cycle starts and lower cycle ramping than (R). (R^c) results in the lowest number of cycle starts, while (E^c) results in the

highest, which is 330% more than (R^c). This difference is due to (R^c)'s under-accounting of performance degradation at lower power output (shown in Figure 3.7(b)), which results in behavior similar to that of (C), i.e., a low number of cycle starts.

Reliability at x% is defined as the system's capacity factor for the x% highest-valued time periods. For example, during the year's 10% highest-valued hours (876 hours), (C) generates 94.85% of the maximum possible energy, i.e., the product of the grid transmission limit of 165 MW_e and the number of high-valued time periods. Reliability at several different thresholds provides insight on how the system configuration is able to provide power during high-value time periods. Table 3.4 shows that (E) results in higher 10%, 25%, and 50% reliabilities compared to (R), because: (i) (E) cycle performance is slightly higher than (R) at full-load operation; and (ii) (R) operates at low load more often than (E) to avoid cycle starts, but at the cost of forgoing high-valued time periods, which causes the larger differences in reliabilities metrics between (R^c) and (E^c).

Simulation time is the wall clock time between when the simulation starts and ends, and includes the time to design the heliostat field and simulate the power cycle using dispatch optimization and updating the simulation schedule every day [11]. Table 3.4 shows the simulation times of (C) and (R^c) are about 70% faster than for the other cycle models due to the trade-off between cycle start-up and low-load operation being more obvious to the dispatch optimization solver.

3.5.3 Impact on Annual Performance for a CSP-PV Hybrid System

To investigate cycle dispatch behavior for a CSP-PV hybrid system, we select a hybrid design that corresponds to the lowest PPA price across all cycle models, i.e., a CSP system with a solar multiple of 1.25, 8 hours of TES, and a 225 MW_{DC} PV system with a 1.3 DC-to-AC ratio. However, the hybrid system configuration corresponding to "lowest PPA" design varies depending on the cycle model implemented. We discuss this inconsistency in §3.5.4.

The histogram in Figure 3.9 depicts the annual percentage of time the power cycle spends in a thermal input range for a CSP-PV hybrid system using the five off-design performance

cycle models, and shows that the system rexhibits a large decrease in full power operation because the solar multiple is half that of the CSP-only design (compare with Figure 3.8). Over the year, the power cycle is in an "off" state a majority of the time (approximately 40 to 63%). As a result, the power cycle operates at full load for 10 to 18% of the year, compared to the 35 to 46% seen in the CSP-only case. Like the CSP-only case, (C) and (R^c) favor low power output over cycle shutdown and start-up.

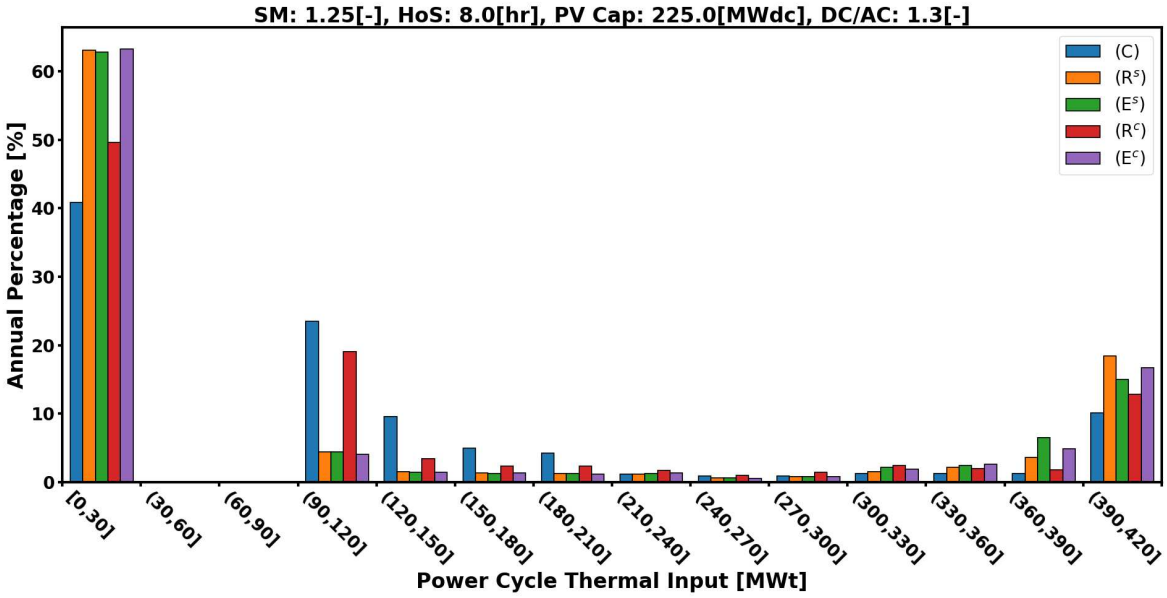

Figure 3.9: Annual percentage of time the power cycle spends in a thermal input range for a CSP-PV hybrid system using the five off-design performance cycle models. The $[0, 30]$ range only contains values of 0 MW_t thermal input, corresponding to the cycle being in an "off" state.

Table 3.5 presents annual performance metrics for the five different off-design cycle performance models of the CSP-PV hybrid system with lowest PPA price design. In addition to the annual performance metrics presented in Table 3.4 for the CSP-only system, Table 3.4 contains the percentage of CSP and PV curtailment. Table 3.5 shows that cycle models (C) and (R^c) perform similarly across all metrics; likewise, there are small differences between cycle models (R^s), (E^s), and (E^c). (C) and (R^c) result in lower capacity factors and fewer cycle starts than the other models. Hybridization of PV with CSP results in more than twice

the number of cycle starts compared to the CSP-only design. The (C) and (R^c) models exhibit more *PV curtailment*, about 3.5% of the annual PV generation, than CSP curtailment, about 0.7% of the annual CSP generation. Table 3.5 shows that (C) and (R^c) result in lower reliabilities and simulation times compared to the other models.

3.5.4 Implications on System Design

To investigate the effect that off-design cycle performance has on system design, we determine the system design corresponding to the lowest PPA price for each level of PV system DC capacity, shown in Table 3.6, which presents the solar multiple and hours of storage corresponding to the lowest PPA price design for two groups of off-design performance cycle models, categorized by agreement in the design characteristics of solar multiple and hours of storage. The first group consists of (C) and (R^c), while the second group consists of (R^s), (E^s), and (E^c). Table 3.6 shows that system design parameter DC-to-AC ratio has more variation between the cycle models.

Table 3.6 demonstrates that the two groups result in the same solar multiple and hours of storage for a PV system DC capacity of 0, 25, 50, 125, and 175 $\mathrm{MW_{DC}}$, leading us to conclude that off-design performance has less impact on the lowest PPA design's solar multiple and hours of storage combination when the capacity of the PV system is smaller. The discrepancy between the off-design cycle models' resulting lowest PPA design configurations leads to different "optimal" system designs.

We investigate, for the designs in Table 3.6 corresponding to lowest-PPA-priced systems, their resulting annual simulation metrics as a function of: (i) PV system DC capacity, and (ii) the particular cycle performance model. Figure 3.10 depicts normalized PPA, capacity factor, annual cycle starts, and top 25% reliability for the five power cycle models. PPA prices are calculated using SAM's default costs (Version 2018.11.11) and are normalized using the lowest PPA price for the CSP-only case, which corresponds to $\$107.58/\mathrm{MWh_e}$ using (E^s) cycle model.

Table 3.5: Comparison between annual performance metrics using the various off-design cycle models for a CSP-PV hybrid system comprised of a solar multiple of 1.25, 8 hours of TES, and 225 MW_{DC} PV system with a DC to AC ratio of 1.3. Annual performance metrics shown are: capacity factor, number of cycle starts, cycle ramp index, percentage of CSP curtailment, percentage of PV curtailment, reliability (10%, 25%, and 50%), and simulation time. We also report "%Δ," which represents the percentage change between (E) and (R) utilizing the same boiler pressure operation, i.e., sliding or constant.

Cycle Model	**Capacity Factor** [%]	**Cycle Starts** [-]	**Cycle Ramp** [%]	**CSP Curtailment** [%]	**PV Curtailment** [%]	**Reliability**			**Simulation Time** [min.]
						10% [%]	**25%** [%]	**50%** [%]	
(C)	61.07	289	84.86	0.69	3.73	97.25	91.07	90.07	13.19
(R^s)	62.46	337	98.25	1.30	1.52	97.79	94.24	92.17	16.86
(E^s)	62.90	337	98.62	1.98	1.47	98.42	94.56	92.14	17.35
%Δ [%]	+0.70	+0.00	+0.38	+52.93	-3.19	+0.64	+0.34	-0.03	+2.90
(R^c)	61.91	288	98.57	0.68	3.34	97.26	92.19	90.89	14.24
(E^c)	62.67	340	98.69	2.09	1.34	98.43	94.79	92.23	17.04
%Δ [%]	+1.23	+18.06	+0.13	+208.01	-60.01	+1.19	+2.83	+1.48	+19.71

Table 3.6: Solar multiples, hours of storage, and DC-to-AC ratios corresponding to the lowest PPA price for each DC capacity of PV system.

PV Capacity [$\mathbf{MW_{DC}}$]	**Solar Multiple**		**Hours of Storage**		**DC-to-AC Ratio**				
	Group 1: {(C), (R^c)}	Group 2: {(R^s), (E^s), (E^c)}	Group 1: {(C), (R^c)}	Group 2: {(R^s), (E^s), (E^c)}	(C)	(R^c)	(R^s)	(E^s)	(E^c)
0	2.50	2.50	10	10	**N/A**				
25					1.3	1.1	1.2	1.0	1.3
50					1.1	1.2	1.1	1.2	
75	2.25			12	1.1	1.2			1.0
100			12		1.2	1.0	1.1		1.2
125		2.25			1.2				
150	2.00				1.2		1.3	1.2	
175		2.00			1.3				
200		1.75			1.3		1.2		1.1
225	0.75	1.25	6	8	1.3	1.2	1.3		

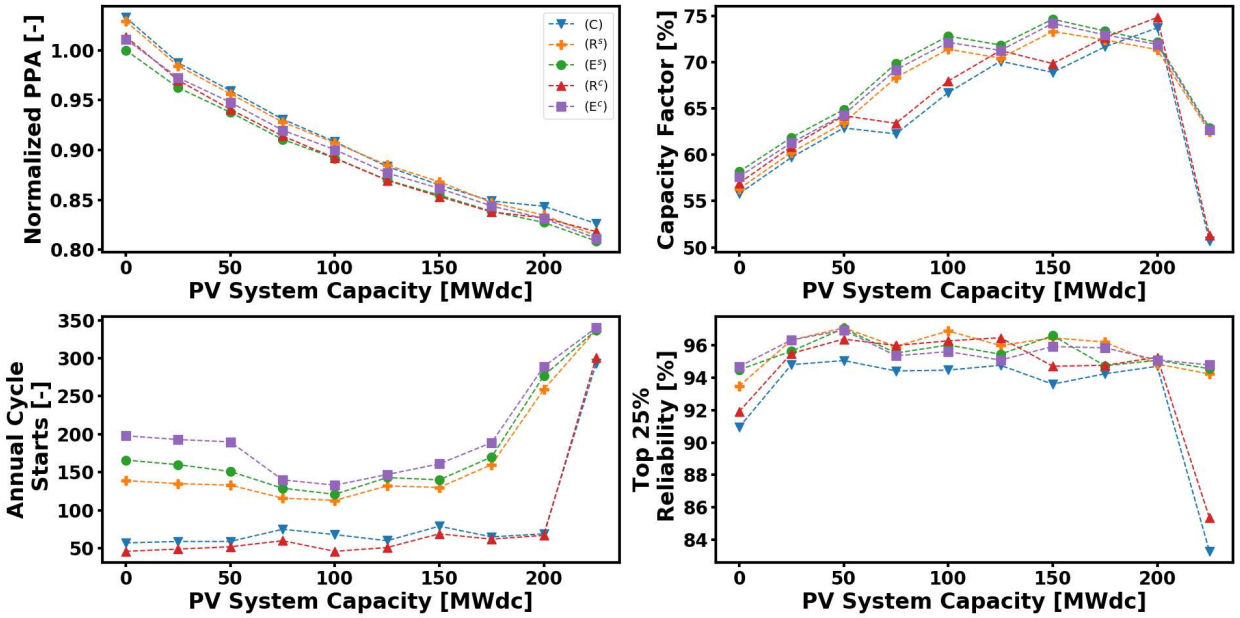

Figure 3.10: Normalized PPA, capacity factor, annual cycle starts, and top 25% reliability for the five power cycle models at varying DC capacity of the PV system. Design for each data point corresponds to lowest PPA price system.

Figure 3.10 shows that PPA prices decrease as PV system DC capacity increases, with about a 17% decrease from 0MW_{DC} to 225MW_{DC}. At any given PV system capacity, the variability in PPA price across the five off-design cycle models is small, with a maximum range of 3.3% occurring under a 0MW_{DC} PV system condition. System capacity factor has a high dependence on design variable values. At a PV system DC capacity of 225MW_{DC}, there is a drop in capacity factor due to the large reduction in solar multiple and hours of storage (Table 3.6). This result occurs because the PV system capacity is approaching the grid transmission capacity, resulting in the CSP system being shut down during PV generation to reduce curtailment. Correspondingly, for all the off-design cycle models, there is a steep increase in the number of starts as the PV system's DC capacity approaches 225MW_{DC} because the grid transmission capacity constraint requires the cycle to shut down during high PV generation time periods to mitigate system curtailment. Of the four metrics shown in Figure 3.10, annual cycle starts has the greatest variability between the different

power cycle models. (E^c)'s annual cycle starts decrease between 50 and 75MW_{DC} because of the increase in the number of hours of storage. Reliability for the 25% highest-valued time periods is relatively constant for the five power cycle models, except for (C) and (R^c) at high PV system DC capacity.

3.6 Conclusions

We present a methodology to model a Rankine cycle with the fidelity to estimate off-design performance. We implement said methodology into Engineering Equation Solver and validate the results against data provided by our industry partners and a model from literature that implements similar methodology. Then, we integrate the validated model results into SAM utilizing the "user-defined" cycle option which enables us to investigate the impact of off-design cycle performance on cycle operation, overall CSP plant performance, and minimum PPA price system design.

The results indicate that previous modeling of Rankine cycle off-design performance is either too optimistic (constant boiler pressure) or conservative (sliding boiler pressure). The former causes unrealistic operation of the power cycle which can lead to sub-optimal system designs. The latter results in lower solar-to-electric conversion which negatively impacts plant finances and PPA price.

Future work will update SAM's default Rankine cycle models using (E) estimates of off-design performance. The work outlined above assumes an instant transition between steady-state points from one time period to the next. Future work is warranted to investigate the power cycle transients to understand the inaccuracy of this assumption at increasing time fidelity.

CHAPTER 4

BLACK-BOX OPTIMIZATION FOR DESIGN OF CONCENTRATING SOLAR POWER AND PHOTOVOLTAICS HYBRID SYSTEMS WITH OPTIMAL DISPATCH DECISIONS

This paper is to appear in *SolarPACES 2019 AIP Conference Proceedings*

William T. Hamilton[12,13], Alexandra M. Newman[12,14,15], Robert J. Braun[12,15], and Michael J. Wagner[16]

4.1 Abstract

The hybridization of concentrating solar power (CSP) and photovoltaics (PV) can enable dispatchable renewable electricity generation at a lower price than current stand-alone CSP systems. However, designing a CSP-PV hybrid system can be challenging because of the many degrees of freedom in design that affect the internal and external system interactions and trade-offs. We develop a methodology to determine optimal designs for CSP-PV hybrids by implementing NLopt's derivative-free, or "black-box," algorithms around pre-existing CSP-PV hybrid simulation software that utilizes the National Renewable Energy Laboratory's System Advisor Model (SAM); we then employ a dispatch optimization model to determine operational decisions that maximize a plant's profits. We present optimal designs for CSP-PV hybrid systems dispatching against four time-of-delivery (ToD) pricing structures. NLopt's algorithms can improve the base case design's power purchase agreement (PPA) price by 15% to 21%, depending on the ToD pricing structure. In addition, we analyze the resulting optimal CSP-PV hybrid design's annual performance metrics, which

[12]Department of Mechanical Engineering, Colorado School of Mines, Golden, CO 80401
[13]Ph.D. Student
[14]Corresponding Author
[15]Professor of Mechanical Engineering
[16]Mechanical Engineer, Ph.D., National Renewable Energy Laboratory, Golden, CO 80401

tend to have capacity factors between 50% and 62%, but are able to generate electricity during the year's highest-valued periods about 90% of the time. Lastly, we investigate the trade-offs between capacity factor and PPA price using Pareto fronts and demonstrate that, for some ToD pricing structures, the system capacity factor can increase by 20% but at the expense of a 2% increase in PPA price.

4.2 Introduction

Due to their design flexibility and dispatchability, concentrating solar power (CSP) systems with thermal energy storage (TES) are becoming attractive solutions for renewable portfolios around the world. The design flexibility of CSP can fulfill many different market needs by providing either peaking, intermediate, or baseload power generation, depending on the system's solar multiple and hours of available TES. Utility companies and governments use time-of-delivery (ToD) price schedules to incentivize power generation during times of peak demand and/or low supply, which can vary depending on the utility's current generation portfolio and end-use customer demand. Due to the complexity of CSP system sizing and various constraints imposed on these systems, e.g., ToD pricing, design optimization using dispatch is required to ensure that CSP is competitive in electricity markets.

Locations with high direct normal irradiance (DNI) solar resource inherently have high penetration of photovoltaic (PV) systems on the grid. As a result, to stay competitive, CSP systems must dispatch power generation around PV generation. The PV system within a CSP-PV hybrid could be co-located with the CSP system, located on the same transmission line as the CSP system but miles apart, or be a conglomerate of small rooftop systems within the municipality to which the CSP system is supplying electricity.

In this paper, we develop and implement a methodology to determine optimal designs for CSP-PV hybrids using derivative-free, or "black-box," algorithms. We provide a description of our methodology to evaluate operational decisions. The contribution of this paper is to present the optimal designs for CSP-PV hybrids dispatching against four ToD pricing structures. Furthermore, we provide trade-off analysis using Pareto fronts to demonstrate

the relationship between system capacity factor and PPA price for the four ToD pricing structures under investigation.

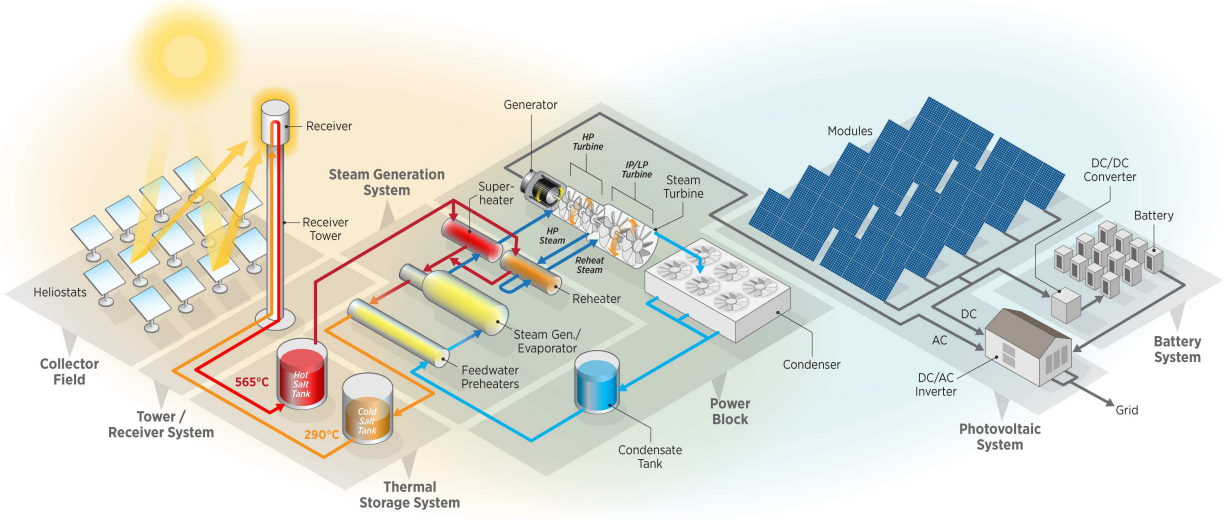

Figure 4.1: CSP-TES-PV-battery hybrid system configuration (Graphic © NREL/Al Hicks). On the left, the system consists of a molten salt power tower CSP plant, which consists of a heliostat field, molten salt receiver, thermal energy storage, and a Rankine power cycle. On the right, the system consists of a photovoltaic system with battery storage. The system depicted is not all-inclusive of components required for control or operation.

4.3 Approach

We simulate the performance of CSP-PV hybrid systems and evaluate their financial feasibility using the System Advisor Model (SAM) [30], which is an open-source simulation software package developed by the National Renewable Energy Laboratory (NREL) that enables users to analyze the financial feasibility and performance of renewable energy technologies. However, SAM's user interface only allows for the evaluation of a system design utilizing a single renewable energy technology and thereby precludes analysis of hybrid systems. In previous work, we developed a methodology to simulate the hybridization of the two commercial-scale solar technologies, power tower CSP with TES and a PV system with and without the inclusion of electrical energy storage (EES) [18], shown in Figure 4.2. Our methodology utilizes SAM's Python application programming interface (API) to build a wrapper to evaluate the performance of the hybrid system as a whole.

Co-located CSP and PV system design can be particularly challenging if the design requires the two sub-systems to behave as a single power generation system, which could be applicable for the case in which two systems cover a baseload, as a result of, e.g., an island grid with a consistent load requirement, or a utility agreement to schedule CSP generation around PV generation. However, these scenarios require an intelligent simulation control strategy of the dispatchable energy storage technologies. To this end, previous work focuses on the development of an optimization model to schedule or dispatch each sub-system within the overall system [18].

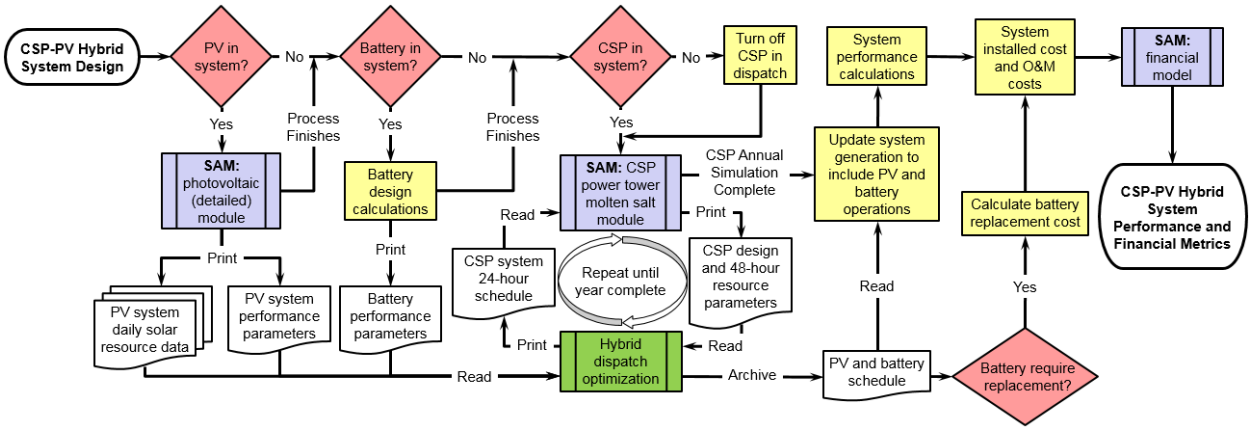

Figure 4.2: Flow diagram of the software architecture implemented around the hybrid dispatch optimization, modified from previous work.

4.3.1 Hybrid Dispatch Optimization

Dispatch optimization enables optimal scheduling of sub-system operations, i.e., receiver, power cycle, and EES. With an uncertain solar resource and limited energy storage, optimal operational decisions are complex and multifaceted. Our hybrid dispatch optimization model is a mixed-integer linear program (MILP), written in A Mathematical Programming Language (AMPL) [56], and solved using IBM CPLEX [57]. A MILP enables the use of binary logic related to on-off decisions; furthermore, a linear model is often more tractable than its nonlinear equivalent.

To determine a solution for an annual horizon, we solve our dispatch optimization model using a rolling time horizon with a 48-hour look-ahead, every 24-hours, depicted in the lower center of Figure 4.2. Relative to solving the monolith consisting of a year-long time horizon, this approach has the benefits of: (i) providing the dispatch optimization model with a limited view into the future to ensure that short-term decisions are uninfluenced by unrealistic future knowledge, such as solar resource or market pricing three to five days ahead, and (ii) increasing tractability and thereby faster solution times.

For brevity, we do not describe the dispatch optimization formulation in full detail; instead, we present the objective function, which maximizes system profits, i.e., revenue less operation costs. We calculate the following parameters: (i) revenue as the product of net system generation, a power purchase agreement (PPA) price multiplier (dictated by market structure), and an assumed base PPA price of \$100/MWh; and (ii) fixed and variable operation costs for different system operations, the former of which are associated with binary decisions (e.g., power cycle start-up), and the latter of which pertain to continuous variables (e.g., power cycle output). We provide a detailed description of costs, as well as the mathematical formulation of the objective function and all constraints, in previous work [18].

4.3.2 System Design Optimization

We explore the system design space using different combinations of solar and energy storage technologies, i.e., CSP with TES, PV, and EES, without the onerous development of a tailored heuristic to determine system operations for each design. We implement derivative-free, "black-box" optimization algorithms to intelligently explore and narrow the search.

4.3.2.1 Variables

High-level design variables dictate overall system performance and financial feasibility. Table 4.1 presents the design variables, their corresponding lower and upper bounds, and the base case values for the two sub-systems, i.e., CSP with TES, and PV.

Table 4.1: Sub-system design variables with upper bound, lower bound, and base case values.

Design Variable	Units	Lower Bound	Upper Bound	Base Case
Concentrating Solar Power with Thermal Energy Storage				
Receiver Diameter	[m]	10	30	17
Receiver Height	[m]	10	30	22
Tower Height	[m]	100	300	195
Power Cycle Capacity	[MW_e]	150	200	175
Solar Multiple	[-]	0.5	3.0	2.5
Hours of TES	[hours]	2	20	10
Photovoltaics				
Field DC Capacity	[MW_{dc}]	50	300	100
DC-to-AC ratio	[-]	1.0	1.6	1.2

4.3.2.2 Objective Function

The objective function minimizes the sum of PPA price and the penalized deviation of the design's resulting maximum solar flux from an imposed flux limitation, shown below.

$$\text{minimize} \quad \text{PPA}\left(\mathcal{S}\left(\mathcal{D}\right)\right) + P^{\text{FLUX}} \times \max\left\{\text{FLUX}^{\text{MAX}}\left(\mathcal{RF}\right) - \text{FLUX}^{\text{LIM}}, 0\right\} \tag{4.1}$$

where PPA price [US¢/kWh] is a function of the system simulation (denoted by $\mathcal{S}$), which is a function of our dispatch optimization model (denoted by $\mathcal{D}$), P^{FLUX} is the penalty to scale the deviation of maximum flux to an appropriate magnitude to match changes in PPA price, FLUX^{MAX} is the maximum solar flux experienced by the receiver and is a function of the receiver and heliostat field design (denoted by $\mathcal{RF}$), and FLUX^{LIM} is the maximum flux limit. By minimizing PPA price, we can investigate the effect of ToD pricing on optimal system design. We calculate PPA price by specifying a project's target internal rate of return of 11% at 20 years with a PPA price escalation rate of 1%/year (default values for PPA price calculation in SAM's PPA single owner, "utility," financial model) [30]. We use a value of 0.001 for P^{FLUX} to scale maximum flux deviations above and below the maximum flux limit. Our maximum flux limit, FLUX^{LIM}, is 1000 kW/m^2. Above this value, the receiver's design would require expensive materials, which our cost models do not represent. We

penalize deviations below FLUX^{LIM} to avoid low-flux receiver designs, which would result in an undersized heliostat field for the corresponding receiver.

4.3.2.3 Solution Technique

Our design optimization problem is challenging,"black-box," and requires a derivative-free algorithm because there is no explicit mathematical formula for PPA price as a function of system design variables. We implement NLopt, an open-source library for nonlinear optimization, that contains algorithms for either global or local searches utilizing derivative-free or gradient-based, approaches [83]. NLopt enables us to quickly implement and test multiple algorithms simultaneously through the Python API.

We employ a two-phase method utilizing both global and local search algorithms to reach an optimal system design, shown in Figure 4.3. In the first phase, we employ the following NLopt global-search, derivative-free algorithms to explore the design variable space and provide the "best" system design: DIRECT [84], DIRECT-L [85], CRS2-LM [86], ISRES [87], and ESCH [88, 89], where the "best" corresponds to the lowest objective function value. In the second phase, we employ NLopt's local-search, derivative-free algorithms, with the "best" design as an initial condition, to "polish" the optimal system design. We utilize the following local-search algorithms in the "polishing" phase: COBYLA [90], BOBYQA [91], NEWUOA [92], PRAXIS [93], NELDERMEAD [94], and SBPLX [95]. We reduce computational time through parallelization. After the second phase, we select the best solution found across all the local algorithms as the "optimal" system design. Because of the nature of "black-box" optimization, there is no guarantee that a solution found by this approach is a global optimum. However, in this paper, we refer to the best solution found by the two-phase approach as the "optimal system design." For the first phase, we set the stopping criterion to the minimum of an objective function absolute tolerance of 1×10^{-4} and a five-day computational solve time limit. For the second phase, we change the limit on computation time to two days.

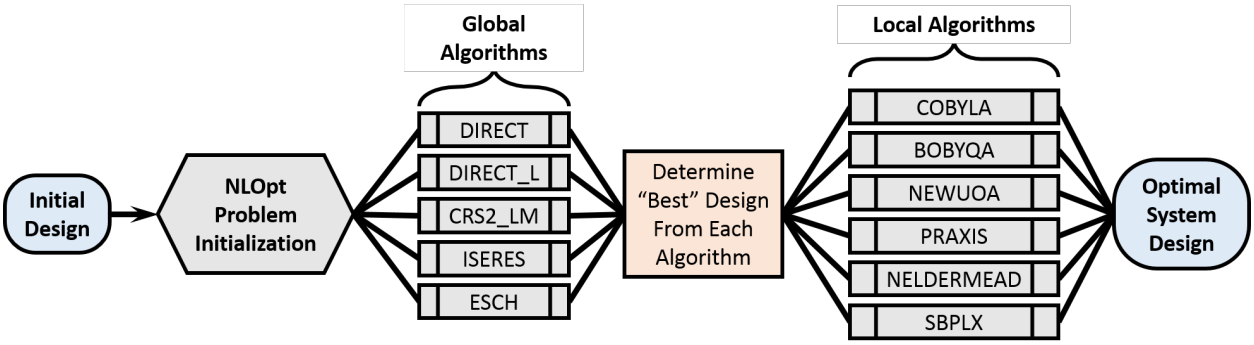

Figure 4.3: Schematic of the system design optimization methodology utilizing global and local search optimization algorithms within the open-source NLopt library.

4.3.3 Solar Hybrid Design Case Study

To investigate the effects that ToD schedules have on optimal system design, we conduct design optimization on a CSP-PV hybrid system operating within four different ToD pricing schedules at a fixed location (Rice, CA in the present analysis) using identical weather. Rice possesses high solar resource and abundant weather data with one-minute time fidelity for the years 1998 to 2017. For the system design, we assume that the PV sub-system configuration consists of single-axis-tracking PV modules, that the hybrid system lacks EES, and that the combined power output is constrained to an arbitrary interconnection capacity limit of 165 MWac.

The CSP-PV hybrid system operates within the following four ToD pricing schedules: Pacific Gas and Electric (PG&E) 2016 full capacity deliverability [30], pool-price tariff [96], two-tier tariff [96], and California Independent System Operator (CAISO) price node data for Rice, CA in 2017 [20], shown in Figure 4.4. The PG&E 2016 ToD schedule has three seasonal variations in pricing profile with the highest-valued periods occurring from July through September during a six-hour block between 3pm and 9pm. The pool-price ToD schedule is divided into two seasons, winter and the rest of the year, and includes a 3-hour morning and a 2-hour evening price peak. In addition, pool-price distinguishes between weekdays, Saturday, and Sunday pricing profiles. Figure 4.4b depicts the weekday profiles. Saturday's profile has a 5-hour morning and a 2-hour evening peak equal to the weekday

"mid-day" price, i.e., 10am to 6pm; outside of peak pricing, the PPA multiplier value is equal to lowest price in the weekday profile. Sunday's profile is a constant value equal to the weekday's lowest price. The two-tier ToD schedule has no seasonal variation in pricing. The daily pricing schedule throughout the year is identical to that shown in Figure 4.4c and is constructed of a base price (PPA multiplier equal to one) for the hours of 5am to 5pm and 9pm to 10pm, and a peak price (270% of the base price) occurring between 5pm to 9pm. Outside the base- and peak-price windows, the two-tier ToD schedule has a PPA multiplier equal to zero. Figure 4.4d depicts the CAISO-node hourly pricing data for every day in 2017 and the annual hourly average. The CAISO-node data has attributes of the three other ToD schedules, i.e., morning and evening peak prices and low prices in the middle of the day.

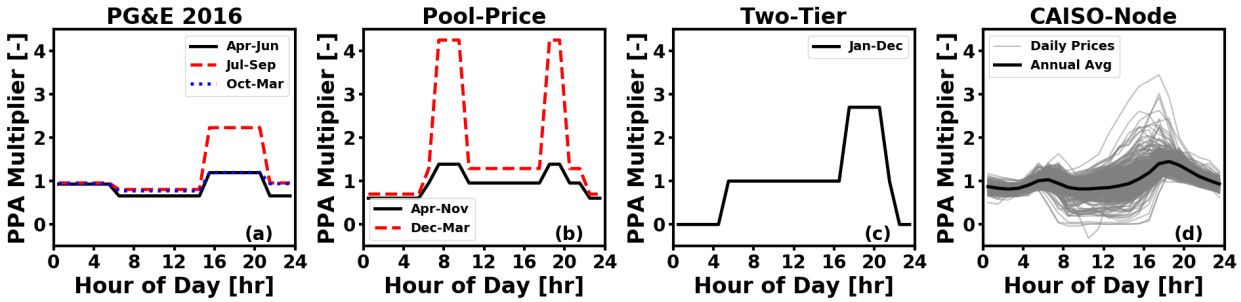

Figure 4.4: ToD pricing schedules for a) Pacific Gas and Electric (PG&E) 2016 full capacity deliverability, b) pool-price tariff, c) two-tier tariff, and d) CAISO-node price data for Rice, CA in 2017.

4.4 Results

For the four ToD pricing schedules, Table 4.2 presents the PPA prices, maximum flux, and objective function values for the base case and optimal design. The base case's maximum flux exceeds the imposed limit of 1000 kW/m^2, making it an infeasible receiver and heliostat field combination. The 141 kW/m^2 flux over the maximum limit results in a 0.141 penalty to the objective function value. Due to the two terms in the objective function, NLopt's algorithms reduce the system's PPA price and converge the maximum flux to the imposed limit, simultaneously. Our methodology results in an improvement in the objective function value relative to the base case design of between 15.8% and 22.8%, depending on the ToD

pricing schedule. Approximately 90% of this improvement is derived from decreasing the system's PPA price while the remainder results from reducing the penalized maximum flux deviation. Of the four ToD pricing schedules, two-tier and PG&E 2016 result in the lowest and highest optimal PPA prices at \$59.8/MWh and \$83.1/MWh, respectively.

Table 4.2: The base case and optimal designs resulting PPA price, maximum flux, and objective function value for the four ToD pricing schedules.

ToD Pricing Schedules		**PPA** [\$/MWh]	**Maximum Flux** [kW/m^2]	**Objective Value** [US¢/kWh]
PG&E 2016	Base Case	97.31	1141	9.872
	Optimal	83.13	1001	8.313
	% Change	-14.6%	-12.3%	-15.8%
Pool-Price	Base Case	84.51	1141	8.592
	Optimal	66.71	1000	6.671
	% Change	-21.1%	-12.4%	-22.4%
Two-Tier	Base Case	76.04	1141	7.745
	Optimal	59.75	999	5.976
	% Change	-21.4%	-12.4%	-22.8%
CAISO-Node	Base Case	97.33	1141	9.874
	Optimal	82.30	1006	8.236
	% Change	-15.4%	-11.8%	-16.6%

Table 4.3 presents the optimal system design variable values for the four ToD pricing schedules. The optimal receiver aspect ratio, defined as the quotient of height and diameter, is about one for all ToD pricing schedules except for the pool-price schedule. The receiver and tower design variable values, i.e., tower height, receiver diameter, and receiver height, scale with the system's solar multiple. For all the ToD pricing schedules, cycle capacity is approximately at its imposed lower bound of 150 MWe because the addition of the CSP sub-system increases the overall system's PPA price compared to a PV-only system, making it challenging to optimize CSP-PV hybrid designs using PPA price as the objective function without constraints on minimum power cycle sizing. The PG&E 2016 and CAISO-node schedules result in similar optimal designs and optimal solar multiples and hours of thermal energy storage of approximately 1.1 and 8.2, respectively. The pool-price and two-tier ToD

schedules produce smaller optimal CSP designs, with solar multiples below unity, and approximately 5 hours of thermal energy storage. For the PV sub-system, the optimal design results in a PV capacity of approximately 255 MWdc with a DC-to-AC ratio of 1.4. The PG&E 2016 pricing schedule yields a lower DC-to-AC ratio compared to the results of the other pricing schedules.

Table 4.3: Optimal system design variable values for the four ToD pricing schedules.

Design Variable	Units	PG&E 2016	Pool-Price	Two-Tier	CAISO-Node
Concentrating Solar Power with Thermal Energy Storage					
Receiver Diameter	[m]	15.5	10.2	12.5	14.7
Receiver Height	[m]	15.0	12.1	12.7	15.3
Tower Height	[m]	144	108	121	142
Power Cycle Capacity	[MW_e]	150.0	150.1	150.7	150.6
Solar Multiple	[-]	1.17	0.58	0.81	1.08
Hours of TES	[hours]	8.2	4.9	5.1	8.2
Photovoltaics					
Field DC Capacity	[MW_{dc}]	250	266	244	261
DC-to-AC ratio	[-]	1.16	1.49	1.45	1.39

Table 4.4 presents the optimal system design's annual simulation metrics for the four ToD pricing schedules. Installed cost is the sum of direct and indirect costs of the proposed design and excludes any financing costs. We calculate installed cost using the default cost functions and parameter values within SAM's Photovoltaic (detailed) and CSP power tower molten salt modules [81]. The optimal designs corresponding to the PG&E 2016 and CAISO-node pricing result in higher installed cost than pool-price and two-tier because their design requires a larger CSP sub-system which, in turn, enables a higher system capacity factor due to higher annual energy generation. Because we constrain total system generation to remain below an interconnection capacity limit, we calculate capacity factor as the quotient of total energy generation and the product of the capacity limit and number of hours in a year. We define a 10% reliability level as the system's capacity factor for the top 10% highest-valued periods of the year, i.e., the highest-valued 876 hours. The 10% reliability level provides

insight on how much energy generation is occurring during the highest-valued periods. All of the optimal designs have a 10% reliability level greater than 91%. We calculate the PV curtailment and clipping as the percentage of total PV DC electricity generation. The former is a result of the dispatch optimization model "taking" less DC power than available and the latter is a result of the PV DC generation exceeding the inverter's maximum DC input limit. By allowing for PV curtailment, we enable the NLopt optimization algorithms to evaluate the trade-off between increasing PV sub-system capacity, i.e., increasing PV annual generation, and curtailment during periods of high solar resource, i.e., spring and summer. The optimal design corresponding to the PG&E 2016 pricing produces no PV clipping because of the design's low DC-to-AC ratio. PV curtailment ranges from 1.2% to 4.6%, depending on the ToD pricing. Almost all of the PV curtailment is due to "shaving the peak" during the spring and summer months.

Table 4.4: Optimal system design's annual simulation metrics for the four ToD pricing schedules.

Design Variable	**Units**	**PG&E 2016**	**Pool-Price**	**Two-Tier**	**CAISO-Node**
Installed Cost	[$MM]	861.6	716.6	745.7	855.5
Capacity Factor	[%]	62.4	50.3	52.4	61.8
Total Generation	[GWh_e]	901.4	726.5	757.1	892.5
10% Reliability	[%]	95.3	92.0	97.1	91.0
PV Curtailment	[%]	4.60	3.26	1.23	4.57
PV Clipping	[%]	0.00	3.94	2.94	1.62

Figure 4.5 depicts the "best-known" Pareto fronts of PPA price versus (a) capacity factor and (b) 10% reliability for the four ToD pricing structures. A red-outlined symbol distinguishes the optimal design presented in Table 4.3. We generate these Pareto fronts by compiling a set of all explored designs and their performance during the two phases and across all algorithms. Then, we disregard any designs that exceed the imposed maximum flux limit. From this subset, we determine all the non-dominated points for the metrics of interest, shown in Figure 4.5.

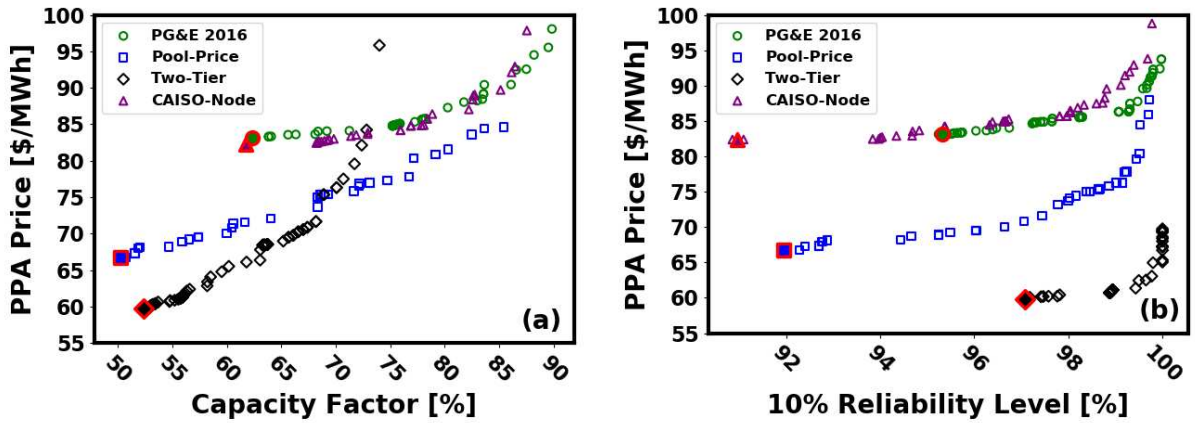

(a) PPA price versus capacity factor

(b) PPA price versus 10% reliability

Figure 4.5: The "best-known" Pareto fronts of PPA price versus (a) capacity factor and (b) 10% reliability for the four ToD pricing structures. A red-outlined symbol distinguishes the optimal design presented in Table 4.3.

From these Pareto fronts, we quantify the trade-offs between CSP-PV hybrid system's PPA price versus capacity factor and 10% reliability level for the four ToD pricing structures. From Figure 4.5a, the capacity factor Pareto fronts for PG&E 2016 and CAISO-node pricing have the smallest slope near the optimal designs, meaning that the system's capacity factor can increase with a small impact on PPA price. For example, a CSP-PV hybrid system in the PG&E 2016 pricing can achieve a capacity factor of 75% (20% increase) with an adverse effect on PPA price of \$1.66/MWh (2% decrease) compared to the optimal design. We observe a similar result for CAISO-node pricing. However, this asset is not present in the pool-price and two-tier structures, in which the slope of the capacity factor Pareto front near the optimal design is greater. The two-tier pricing results in the most dramatic trade-off between capacity factor and PPA price. Due to the zero-valued PPA multiplier from 10pm to 5am, the two-tier pricing results in a steep increase in PPA price for capacity factors above 68% because it requires power generation during time periods with a zero PPA multiplier, i.e., resulting in no revenue. Figure 4.5b shows that the 10% reliability level Pareto fronts have a slope close to zero near the optimal design, meaning that CSP-PV hybrids can achieve higher reliabilities, up to about 97%, with a small increase in PPA price. For example, a

system within the CAISO-node pricing can increase its 10% reliability level from 91% to 95% with a $1.88/MWh increase in PPA price.

4.5 Conclusions

This paper develops and implements a methodology to determine optimal designs for CSP-PV hybrids using derivative-free algorithms within the NLopt library. We evaluate CSP-PV hybrid designs using NREL's SAM utilizing dispatch optimization for operational decisions. This paper investigates optimal CSP-PV hybrid designs dispatching against four ToD pricing structures. The results indicate that NLopt's derivative-free algorithms can improve the base case PPA price by 15% to 21%, depending on the ToD pricing structure. We present the optimal CSP-PV hybrid designs, which tend to have small CSP sub-systems with large PV sub-systems. In addition, we present the optimal CSP-PV hybrid design's annual performance metrics, which tend to have low capacity factors – from 50% to 62%, but high 10% reliability levels of greater than 90%. Lastly, we investigate the trade-offs between capacity factor and PPA price using Pareto fronts and demonstrate that, for some ToD pricing structures, system capacity factor can increase by 20% with less than a 2% increase in PPA price.

CHAPTER 5

SUMMARY, CONCLUSIONS, AND FUTURE WORK

In Chapter 2, we extend our dispatch model for a stand-alone CSP system to include sub-hourly fidelity, grid constraints with neighboring PV generation, and electric battery storage dispatch decisions. With these extensions, we develop solution techniques to improve problem tractability and reduce solve times by as much as 93%. Additionally, we assess that CSP-PV hybrid systems can almost double capacity factors while resulting in a 30% improvement related to various economic metrics. In Chapter 3, we develop a molten salt-driven Rankine cycle model capable of predicting off-design performance for varying salt inlet temperature, salt mass flow rate, and ambient air temperature. After validating our cycle model, we compare its off-design performance to that of SAM and find that SAM's constant boiler operation model over-predicts performance at salt mass flow rates less than design conditions. By contrast, our cycle model under sliding pressure operations predicts efficiencies higher than those of SAM, especially at low ambient temperatures. Additionally, we investigate the implications of off-design cycle performance on optimal dispatch, annual system metrics, and design configurations with neighboring PV of various sizes. As a result, we find that off-design cycle performance can impact system dispatch and, consequently, optimal design, especially when a CSP-PV hybrid system operates under a grid constraint. In Chapter 4, we develop a methodology for evaluating optimal CSP-PV hybrid system design utilizing derivative-free, "black-box," optimization algorithms. We explore the impact that electricity markets have on the optimal CSP-PV hybrid design configurations. We determine that minimizing PPA price results in CSP systems with low solar multiples and hours of TES which, combined with a PV system, produce capacity factors from 50% to 62%, but high 10% reliability levels of greater than 90%. In summary, locations with high solar resource inherently have high penetration of photovoltaic generation. As a result, to stay competitive,

CSP systems must dispatch electricity around PV generation.

Future efforts should focus on model improvement through increased model fidelity, decreased computational overhead, and added capabilities. Our initial CSP dispatch model possessed hourly time fidelity, which our subsequent efforts reduce this to 10-minute time fidelity and add PV-battery operations. However, solar resource transients occur at the scale of a few minutes, e.g., a cloud passing over the solar field. While modeling the annual performance of a CSP system at one-minute fidelity may be impossible with current computing resources, or at least burdensome for iterating through designs, we can investigate and understand how these performance degradations due to transients scale to predicted production on the 5- or 10-minute time scales. With smaller time intervals, our system dispatch optimization model can be applied to inform plant operators in "real time." Coupled with weather forecasting, such a model has the potential to reduce system operating costs. By reducing computational overhead through techniques not explored in this dissertation, these software tools can be effectively utilized by project developers, policy makers, and researchers. For example, we could use clustering techniques to characterize an annual simulation (stand-alone CSP or CSP-PV hybird system) to a subset of representative days, or dispatch problems, that can be solved in parallel and their resulting solutions stitched together to predict annual metrics. This approach could greatly reduce computational overhead and enable system performance predictions to include ranges of weather uncertainty. As new system configurations are proposed, model capabilities will be added to investigate operational trade-offs of these new systems. One system configuration that has been gaining attention at the time of this writing allows for resistive heating of the TES using inexpensive electricity, generated as the result of renewable energy curtailment. Research into these systems is being proposed with and without a CSP collection field. Heating TES directly could be added to our dispatch optimization and simulation models to understand the associated economic trade-offs.

As the world transitions to a more sustainable energy generation portfolio, the CSP industry needs to market itself as part of the solution. Our work focuses on helping this industry make informed system design and dispatch decisions. CSP systems with or without a neighboring PV facility is challenging to design because the economics depend on system operations within a particular electricity market under varying weather conditions. The greatest advantage of CSP over PV technologies is the integration of inexpensive TES, thereby, making CSP a dispatchable renewable energy resource. However, at the time of this writing, the CSP industry faces many challenges. While TES provides a buffer between solar energy production and electricity generation, collection of thermal energy on days with many weather transients, i.e., clouds and/or high winds, is an operational challenge that results in lower-than-expected system production. Depending on the frequency of these variable-weather days, the CSP plant can struggle to meet its production targets and/or contractual agreements. However, CSP costs are expected to decrease in the coming years and, with more realistic production targets through better annual system simulation modeling, CSP can be another renewable energy success story.

REFERENCES CITED

[1] International Energy Outlook 2017. Technical report, U.S. Energy Information Administration, 9 2017.

[2] Climate Change 2014: Mitigation of Climate Change. Technical report.

[3] International Energy Agency. IEA - Renewable Energy, February 2017. URL `https://www.iea.org/policiesandmeasures/renewableenergy/`.

[4] Paul Denholm, Robert Margolis, Trieu Mai, Greg Brinkman, Easan Drury, Maureen Hand, and Matthew Mowers. Bright future: Solar power as a major contributor to the US grid. *IEEE Power and Energy Magazine*, 11(2):22–32, 2013.

[5] Paul Denholm and Maureen Hand. Grid flexibility and storage required to achieve very high penetration of variable renewable electricity. *Energy Policy*, 39(3):1817–1830, March 2011. ISSN 0301-4215.

[6] Bruce Dunn, Haresh Kamath, and Jean-Marie Tarascon. Electrical Energy Storage for the Grid: A Battery of Choices. *Science*, 334(6058):928–935, November 2011. ISSN 0036-8075, 1095-9203.

[7] Mark Z. Jacobson and Mark A. Delucchi. Providing all global energy with wind, water, and solar power, Part I: Technologies, energy resources, quantities and areas of infrastructure, and materials. *Energy Policy*, 39(3):1154–1169, March 2011. ISSN 0301-4215. doi: 10.1016/j.enpol.2010.11.040. URL `http://www.sciencedirect.com/science/article/pii/S0301421510008645`.

[8] Behnam Zakeri and Sanna Syri. Electrical energy storage systems: A comparative life cycle cost analysis. *Renewable and Sustainable Energy Reviews*, 42:569–596, February 2015. ISSN 1364-0321.

[9] Ran Fu, David J. Feldman, Robert M. Margolis, Michael A. Woodhouse, and Kristen B. Ardani. U.S. Solar Photovoltaic System Cost Benchmark: Q1 2017. Technical Report NREL/TP–6A20-68925, 1390776, September 2017.

[10] Paul A Basore and Wesley J Cole. Comparing supply and demand models for future photovoltaic power generation in the USA. *Progress in Photovoltaics: Research and Applications*, 26(6):414–418, 2018.

[11] Michael J Wagner, Alexandra M Newman, William T Hamilton, and Robert J Braun. Optimized dispatch in a first-principles concentrating solar power production model. *Applied Energy*, 203:959–971, 2017.

[12] Mark Mehos, Craig Turchi, Judith Vidal, Michael Wagner, Zhiwen Ma, Clifford Ho, William Kolb, Charles Andraka, and Alan Kruizenga. Cofncentrating Solar Power Gen3 Demonstration Roadmap. Technical Report January, National Renewable Energy Laboratory, Golden, CO, 2017.

[13] Craig S. Turchi, Zhiwen Ma, Ty W. Neises, and Michael J. Wagner. Thermodynamic Study of Advanced Supercritical Carbon Dioxide Power Cycles for Concentrating Solar Power Systems. *Journal of Solar Energy Engineering*, 135(4):041007, November 2013. ISSN 0199-6231.

[14] Marc T. Dunham and Brian D. Iverson. High-efficiency thermodynamic power cycles for concentrated solar power systems. *Renewable and Sustainable Energy Reviews*, 30: 758–770, February 2014. ISSN 1364-0321.

[15] New Energy Update: CSP. Morocco expects price drop for hybrid CSP plant, widens funding sources, May 2018. URL `http://newenergyupdate.com/csp-today/morocco-expects-price-drop-hybrid-csp-plant-widens-funding-sources`.

[16] Glenn Meyers. CSP & PV Hybrid Plants Gain Sway In Chile, April 2015. URL `https://cleantechnica.com/2015/04/02/csp-pv-hybrid-plants-gain-sway-chile/`.

[17] Paul Denholm and Mark Mehos. Enabling greater penetration of solar power via the use of CSP with thermal energy storage. NREL/TP, Golden, CO, 2011.

[18] William T. Hamilton, Mark A. Husted, Alexandra M. Newman, Robert J. Braun, and Michael J. Wagner. Dispatch optimization of concentrating solar power with utility-scale photovoltaics. *Optimization and Engineering*, September 2019. ISSN 1573-2924. doi: 10.1007/s11081-019-09449-y. URL `https://doi.org/10.1007/s11081-019-09449-y`.

[19] Mark Mehos, Craig Turchi, Judith Vidal, Michael Wagner, Zhiwen Ma, Clifford Ho, William Kolb, Charles Andraka, and Alan Kruizenga. Concentrating Solar Power Gen3 Demonstration Roadmap. Technical Report NREL/TP–5500-67464, 1338899, January 2017.

[20] Michael J. Wagner, William T. Hamilton, Alexandra Newman, Jolyon Dent, Charles Diep, and Robert Braun. Optimizing dispatch for a concentrated solar power tower. *Solar Energy*, 174:1198–1211, November 2018. ISSN 0038-092X.

[21] N. Miller, D. Manz, J. Roedel, P. Marken, and E. Kronbeck. Utility scale Battery Energy Storage Systems. In *IEEE PES General Meeting*, pages 1–7, July 2010.

[22] Andreas Poullikkas. A comparative overview of large-scale battery systems for electricity storage. *Renewable and Sustainable Energy Reviews*, 27:778–788, November 2013. ISSN 1364-0321.

[23] Catherine Heymans, Sean B Walker, Steven B Young, and Michael Fowler. Economic analysis of second use electric vehicle batteries for residential energy storage and load-levelling. *Energy Policy*, 71:22–30, 2014.

[24] Eric Tervo, Kenechi Agbim, Freddy DeAngelis, Jeffrey Hernandez, Hye Kyung Kim, and Adewale Odukomaiya. An economic analysis of residential photovoltaic systems with lithium ion battery storage in the united states. *Renewable and Sustainable Energy Reviews*, 94:1057–1066, 2018.

[25] Johannes Weniger, Tjarko Tjaden, and Volker Quaschning. Sizing of residential PV battery systems. *Energy Procedia*, 46:78–87, 2014.

[26] Bogdan S Borowy and Ziyad M Salameh. Methodology for optimally sizing the combination of a battery bank and PV array in a wind/PV hybrid system. *IEEE Transactions on Energy Conversion*, 11(2):367–375, 1996.

[27] Mohsen Gitizadeh and Hamid Fakharzadegan. Battery capacity determination with respect to optimized energy dispatch schedule in grid-connected photovoltaic (PV) systems. *Energy*, 65:665–674, 2014.

[28] Francois Giraud and Ziyad M Salameh. Analysis of the effects of a passing cloud on a grid-interactive photovoltaic system with battery storage using neural networks. *IEEE Transactions on Energy Conversion*, 14(4):1572–1577, 1999.

[29] Jie Shi, Wei-Jen Lee, Yongqian Liu, Yongping Yang, and Peng Wang. Forecasting power output of photovoltaic systems based on weather classification and support vector machines. *IEEE Transactions on Industry Applications*, 48(3):1064–1069, 2012.

[30] Nathan J. Blair, Nicholas A. DiOrio, Janine M. Freeman, Paul Gilman, Steven Janzou, Ty W. Neises, and Michael J. Wagner. System Advisor Model (SAM) General Description (Version 2017.9.5). Technical Report NREL/TP–6A20-70414, 1440404, May 2018. URL `http://www.osti.gov/servlets/purl/1440404/`.

[31] A Nottrott, J Kleissl, and B Washom. Storage dispatch optimization for grid-connected combined photovoltaic-battery storage systems. In *Power and Energy Society General Meeting, 2012 IEEE*, pages 1–7. IEEE, 2012.

[32] A Nottrott, Jan Kleissl, and Byron Washom. Energy dispatch schedule optimization and cost benefit analysis for grid-connected, photovoltaic-battery storage systems. *Renewable Energy*, 55:230–240, 2013.

[33] Abubakar Sani Hassan, Liana Cipcigan, and Nick Jenkins. Optimal battery storage operation for pv systems with tariff incentives. *Applied Energy*, 203:422–441, 2017.

[34] Yann Riffonneau, Seddik Bacha, Franck Barruel, Stephane Ploix, et al. Optimal power flow management for grid connected pv systems with batteries. *IEEE Transactions on Sustainable Energy*, 2(3):309–320, 2011.

[35] Bo Lu and Mohammad Shahidehpour. Short-term scheduling of battery in a grid-connected PV/battery system. *IEEE Transactions on Power Systems*, 20(2):1053–1061, 2005.

[36] Manuel Jesús Vasallo and José Manuel Bravo. A novel two-model based approach for optimal scheduling in CSP plants. *Solar Energy*, 126:73–92, 2016.

[37] Alexander W Dowling, Tian Zheng, and Victor M Zavala. A decomposition algorithm for simultaneous scheduling and control of CSP systems. *AIChE Journal*, 64(7):2408–2417, 2018.

[38] Francesco Casella, Emiliano Casati, and Piero Colonna. Optimal operation of solar tower plants with thermal storage for system design. *IFAC Proceedings Volumes*, 47(3): 4972–4978, 2014.

[39] J Usaola. Operation of concentrating solar power plants with storage in spot electricity markets. *IET Renewable Power Generation*, 6(1):59–66, 2012.

[40] Mario Petrollese, Daniele Cocco, Giorgio Cau, and Euro Cogliani. Comparison of three different approaches for the optimization of the CSP plant scheduling. *Solar Energy*, 150:463–476, 2017.

[41] Mochamad Ashari and CV Nayar. An optimum dispatch strategy using set points for a photovoltaic (PV)–diesel–battery hybrid power system. *Solar Energy*, 66(1):1–9, 1999.

[42] Michael S Scioletti, Alexandra M Newman, Johanna K Goodman, Alexander J Zolan, and Sven Leyffer. Optimal design and dispatch of a system of diesel generators, photovoltaics and batteries for remote locations. *Optimization and Engineering*, 18(3): 755–792, 2017.

[43] Gavin Goodall, Michael Scioletti, Alex Zolan, Bharatkumar Suthar, Alexandra Newman, and Paul Kohl. Optimal design and dispatch of a hybrid microgrid system capturing battery fade. *Optimization and Engineering*, 20(1):179–213, 2019.

[44] MNGLA Muselli, G Notton, and A Louche. Design of hybrid-photovoltaic power generator, with optimization of energy management. *Solar Energy*, 65(3):143–157, 1999.

[45] MKC Marwali, MA Haili, SM Shahidehpour, and KH Abdul-Rahman. Short term generation scheduling in photovoltaic-utility grid with battery storage. *IEEE Transactions on Power Systems*, 13(3):1057–1062, 1998.

[46] A. Green, C. Diep, R. Dunn, and J. Dent. High Capacity Factor CSP-PV Hybrid Systems. *Energy Procedia*, 69:2049–2059, May 2015. ISSN 1876-6102.

[47] Allan R Starke, José M Cardemil, Rodrigo A Escobar, and Sergio Colle. Assessing the performance of hybrid CSP + PV plants in northern Chile. *Solar Energy*, 138:88–97, 2016.

[48] Mario Petrollese and Daniele Cocco. Optimal design of a hybrid CSP-PV plant for achieving the full dispatchability of solar energy power plants. *Solar Energy*, 137:477–489, 2016.

[49] Daniele Cocco, Luca Migliari, and Mario Petrollese. A hybrid CSP–CPV system for improving the dispatchability of solar power plants. *Energy Conversion and Management*, 114:312–323, 2016.

[50] Christoph Adrian Pan and Frank Dinter. Combination of PV and central receiver CSP plants for base load power generation in South Africa. *Solar Energy*, 146(Supplement C):379–388, April 2017. ISSN 0038-092X.

[51] C Parrado, Aymeric Girard, F Simon, and E Fuentealba. 2050 LCOE (Levelized Cost of Energy) projection for a hybrid PV (photovoltaic)-CSP (concentrated solar power) plant in the Atacama Desert, Chile. *Energy*, 94:422–430, 2016.

[52] Carlos Valenzuela, Carlos Mata-Torres, José M Cardemil, and Rodrigo A Escobar. CSP + PV hybrid solar plants for power and water cogeneration in northern Chile. *Solar Energy*, 157:713–726, 2017.

[53] Mark A. Husted, Bharatkumar Suthar, Gavin H. Goodall, Alexandra M. Newman, and Paul A. Kohl. Coordinating microgrid procurement decisions with a dispatch strategy featuring a concentration gradient. *Applied Energy*, 2017. ISSN 0306-2619.

[54] Joe O'Connor. Battery showdown: Lead-acid vs. lithium-ion. Technical report, 2017. URL `https://medium.com/solar-microgrid/battery-showdown-lead-acid-vs-lithium-ion-1d37a1998287`.

[55] Michael Mobbs. Lead acid vs. lithium-ion battery comparison. Technical report, 2016. URL `https://static1.squarespace.com/static/55d039b5e4b061baebe46d36/t/56284a92e4b0629aedbb0874/1445481106401/Fact+sheet_Lead+acid+vs+lithium+ion.pdf`.

[56] AMPL. *AMPL Version 10.6.16*. AMPL Optimization LLC, 2009.

[57] IBM. IBM ILOG CPLEX Optimization Studio: CPLEX User's Manual, 2016.

[58] Michael J. Wagner and Tim Wendelin. SolarPILOT: A power tower solar field layout and characterization tool. *Solar Energy*, 171:185–196, September 2018. ISSN 0038-092X.

[59] N. Kumar, P. Besuner, S. Lefton, D. Agan, and D. Hilleman. Power Plant Cycling Costs. Technical Report NREL/SR-5500-55433, 1046269, July 2012.

[60] A. Andreas and T. Stoffel. University of Nevada (UNLV): Las Vegas, Nevada (Data). Technical Report NREL Report No. DA-5500-56509, 2006.

[61] A. Andreas and T. Stoffel. Nevada Power: Clark Station: Las Vegas, Nevada (Data). Technical Report NREL Report No. DA-5500-56508, 2006. URL `http://dx.doi.org/10.5439/1052547`.

[62] John Wang, Ping Liu, Jocelyn Hicks-Garner, Elena Sherman, Souren Soukiazian, Mark Verbrugge, Harshad Tataria, James Musser, and Peter Finamore. Cycle-life model for graphite-lifepo4 cells. *Journal of Power Sources*, 196(8):3942–3948, 2011.

[63] S.A. Klein. *Engineering Equation Solver (EES) Academic Professional V10.452-3D*. F-Chart Software, July 2018. URL `http://fchart.com/ees/eeshelp/eeshelp.htm`.

[64] K. C. Cotton. *Evaluating and Improving Steam Turbine Performance*. Cotton Fact Inc., Rexford, NY, USA, 1993.

[65] R. C. Spencer, K. C. Cotton, and C. N. Cannon. A Method for Predicting the Peformance of Steam Turbine-Generators.... 16,500 kw and Larger. *Journal of Engineering for Power*, 85:249–298, October 1963.

[66] David H. Cooke. Modeling of Off-Design Multistage Turbine Pressures by Stodola's Ellipse. Technical report, Richmond, Virginia, November 1983.

[67] David H. Cooke. On Prediction of Off-Design Multistage Turbine Pressures by Stodola's Ellipse. *Journal of Engineering for Gas Turbines and Power*, 107(7):596–606, 1985.

[68] Nico Woudstra, Theo Woudstra, Armando Pirone, and Teus van der Stelt. Thermodynamic evaluation of combined cycle plants. *Energy Conversion and Management*, 51 (5):1099–1110, May 2010. ISSN 0196-8904. doi: 10.1016/j.enconman.2009.12.016. URL `http://www.sciencedirect.com/science/article/pii/S0196890409005226`.

[69] R. Chacartegui, D. Sánchez, J. A. Becerra, A. Muñoz, and T. Sánchez. Performance Analysis of a 565 MW Steam Power Plant. In *Volume 7: Turbomachinery, Parts A, B, and C*, pages 2427–2436, Vancouver, British Columbia, Canada, 2011. ASME. ISBN 978-0-7918-5467-9. doi: 10.1115/GT2011-46272. URL http://proceedings.asmedigitalcollection.asme.org/proceeding.aspx?articleid=1634217.

[70] Carolina Marugán-Cruz, D. Serrano, J. Gómez-Hernández, and S. Sánchez-Delgado. Solar multiple optimization of a DSG linear Fresnel power plant. *Energy Conversion and Management*, 184:571–580, March 2019. ISSN 0196-8904. doi: 10.1016/j.enconman.2019.01.054. URL http://www.sciencedirect.com/science/article/pii/S0196890419301001.

[71] Joshua D. McTigue, Jose Castro, Greg Mungas, Nick Kramer, John King, Craig Turchi, and Guangdong Zhu. Hybridizing a geothermal power plant with concentrating solar power and thermal storage to increase power generation and dispatchability. *Applied Energy*, 228:1837–1852, October 2018. ISSN 0306-2619. doi: 10.1016/j.apenergy.2018.07.064. URL http://www.sciencedirect.com/science/article/pii/S0306261918310924.

[72] Philip G. Brodrick, Adam R. Brandt, and Louis J. Durlofsky. Operational optimization of an integrated solar combined cycle under practical time-dependent constraints. *Energy*, 141:1569–1584, December 2017. ISSN 0360-5442. doi: 10.1016/j.energy.2017.11.059. URL http://www.sciencedirect.com/science/article/pii/S0360544217319084.

[73] E. D. Castronuovo and J. A. P. Lopes. On the optimization of the daily operation of a wind-hydro power plant. *IEEE Transactions on Power Systems*, 19(3):1599–1606, August 2004. ISSN 0885-8950. doi: 10.1109/TPWRS.2004.831707.

[74] Aldo Bischi, Leonardo Taccari, Emanuele Martelli, Edoardo Amaldi, Giampaolo Manzolini, Paolo Silva, Stefano Campanari, and Ennio Macchi. A detailed MILP optimization model for combined cooling, heat and power system operation planning. *Energy*, 74:12–26, September 2014. ISSN 0360-5442. doi: 10.1016/j.energy.2014.02.042. URL http://www.sciencedirect.com/science/article/pii/S0360544214001765.

[75] Zhe Zhou, Pei Liu, Zheng Li, Efstratios N. Pistikopoulos, and Michael C. Georgiadis. Impacts of equipment off-design characteristics on the optimal design and operation of combined cooling, heating and power systems. *Computers & Chemical Engineering*, 48:40–47, January 2013. ISSN 0098-1354. doi: 10.1016/j.compchemeng.2012.08.007. URL http://www.sciencedirect.com/science/article/pii/S0098135412002670.

[76] Michael J Wagner. *Simulation and Predictive Performance Modeling of Utility-Scale Central Receiver System Power Plants*. Master of Science, University of Wisconsin - Madison, 2008.

[77] F. Lippke. Simulation of the part-load behavior of a 30 MWe SEGS plant. Technical Report SAND-95-1293, Sandia National Labs., Albuquerque, NM (United States), June 1995. URL https://www.osti.gov/biblio/95571.

[78] Theodore L. Bergman, Adrienne S. Lavine, Frank P. Incropera, and David P. Dewitt. *Fundamentals of Heat and Mass Transfer*. John Wiley & Sons, Inc., 111 River Street, Hoboken, NJ, 7 edition, 2011. ISBN 978-0470-50197-9.

[79] Angela M. Patnode. *Simulation and Performance Evaluation of Parabolic Trough Solar Power Plants*. Master of Science, University of Wisconsin - Madison, Wisconsin, 2006.

[80] Félix Pérez-Cicala. Modelling of Rankine cycles using Spencer, Cotton and Cannon. https://www.github.com/FelixPerezCicala/modRankineSCC, 2019.

[81] National Renewable Energy Laboratory. System Advisor Model (SAM) Version 2018.11.11, May 2019. URL https://sam.nrel.gov/images/web_page_files/sam-help-2018-11-11-r4.pdf.

[82] National Renewable Energy Laboratory. SAM Simulation Core (SSC). https://github.com/NREL/ssc/blob/develop/tcs/csp_solver_pc_Rankine_indirect_224.cpp, 2019.

[83] Steven G. Johnson. The NLopt nonlinear-optimization package, 2019. URL http://github.com/stevengj/nlopt.

[84] D. R. Jones, C. D. Perttunen, and B. E. Stuckman. Lipschitzian optimization without the Lipschitz constant. *Journal of Optimization Theory and Applications*, 79(1):157–181, October 1993. ISSN 0022-3239, 1573-2878. doi: 10.1007/BF00941892. URL http://link.springer.com/10.1007/BF00941892.

[85] J.M. Gablonsky and C.T. Kelley. A Locally-Biased form of the DIRECT Algorithm. *Journal of Global Optimization*, 21(1):27–37, September 2001. ISSN 1573-2916. doi: 10.1023/A:1017930332101. URL https://doi.org/10.1023/A:1017930332101.

[86] P. Kaelo and M. M. Ali. Some Variants of the Controlled Random Search Algorithm for Global Optimization. *Journal of Optimization Theory and Applications*, 130(2):253–264, August 2006. ISSN 1573-2878. doi: 10.1007/s10957-006-9101-0. URL https://doi.org/10.1007/s10957-006-9101-0.

[87] T. P. Runarsson and Xin Yao. Search Biases in Constrained Evolutionary Optimization. *IEEE Trans. on Systems, Man, and Cybernetics Part C: Applications and Reveiws*, 35 (2):233–243, May 2005. ISSN 1094-6977. doi: 10.1109/TSMCC.2004.841906. URL http://dx.doi.org/10.1109/TSMCC.2004.841906.

[88] Carlos Henrique da Silva Santos, Marcos Sergio Goncalves, and Hugo Enrique Hernandez-Figueroa. Designing novel photonic devices by bio-inspired computing. *IEEE Photonics Technology Letters*, 22(15):1177–1179, 2010.

[89] CHS Santos. Parallel and bio-inspired computing applied to analyze microwave and photonic metamaterial structures, 2010.

[90] M. J. D. Powell. A Direct Search Optimization Method That Models the Objective and Constraint Functions by Linear Interpolation. In Susana Gomez and Jean-Pierre Hennart, editors, *Advances in Optimization and Numerical Analysis*, Mathematics and Its Applications, pages 51–67. Springer Netherlands, Dordrecht, 1994. ISBN 978-94-015-8330-5. doi: 10.1007/978-94-015-8330-5_4. URL https://doi.org/10.1007/978-94-015-8330-5_4.

[91] M J D Powell. The BOBYQA algorithm for bound constrained optimization without derivatives. page 39, 2009.

[92] M. J. D. Powell. The NEWUOA software for unconstrained optimization without derivatives. In Panos Pardalos, G. Di Pillo, and M. Roma, editors, *Large-Scale Nonlinear Optimization*, volume 83, pages 255–297. Springer US, Boston, MA, 2006. ISBN 978-0-387-30063-4 978-0-387-30065-8. doi: 10.1007/0-387-30065-1_16. URL http://link.springer.com/10.1007/0-387-30065-1_16.

[93] Richard P Brent. *Algorithms for minimization without derivatives*. Courier Corporation, 2013.

[94] John A. Nelder and Ronald L. Mead. A Simplex Method for Function Minimization. *Comput. J.*, 7:308–313, 1965. doi: 10.1093/comjnl/7.4.308.

[95] T. Rowan. *Functional Stability Analysis of Numerical Algorithms*. PhD thesis, University of Texas at Austin, 1990.

[96] Rafael Guédez, Monika Topel, Inés Conde, Francisco Ferragut, Irene Callaba, James Spelling, Zhor Hassar, Carlos David Perez-Segarra, and Björn Laumert. A Methodology for Determining Optimum Solar Tower Plant Configurations and Operating Strategies to Maximize Profits Based on Hourly Electricity Market Prices and Tariffs. *Journal of Solar Energy Engineering*, 138(2), April 2016. ISSN 0199-6231. doi: 10.1115/1.4032244. URL https://asmedigitalcollection.asme.org/solarenergyengineering/article/138/2/021006/379586/A-Methodology-for-Determining-Optimum-Solar-Tower.